Enhancing the efficiency of thin-film solar cells using rear-electrode plasmonic gratings

Matthew Benjamin Wincott

Department of Materials

University of Oxford

This thesis is submitted for the degree of

Doctor of Philosophy

Oriel College

Trinity 2016

To my dear wife Jessica and my loving family.

Acknowledgements

Over the course of this project I have received support from many people. I first turn to my principal supervisor Jason Smith, who has given me such a fantastic role model as a scientist of the utmost integrity. My sincere thanks for your guidance and critical judgement, but also your approachability and friendliness. To my co-supervisors Hazel Assender and Andrew Watt, I offer my thanks for your invaluable help in steering my research and for your constant realism. All of the staff at the Department of Materials have been fantastic; I struggle to name them all. Specific thanks must go to Paul Warren for your perpetual IT genius. Thank you to all of my colleagues and friends in the Photonic Nanomaterials Group for your unfailing support and constructive tea breaks. Heartfelt thanks also to my family for all your encouragement and support. Finally, I'd like to thank my wife Jessica for your unceasing love, patience, advice and support throughout and for making my life so rich.

Abstract

Enhancing the efficiency of thin-film solar cells using rear-electrode plasmonic gratings

Matthew Benjamin Wincott

Doctor of Philosphy (Department of Materials) - Oriel College - Trinity 2016

This work describes an investigation into optical methods to improve the optical absorption properties of thin-film organic solar cells. The focus lies on the incorporation of nano-scaled gratings into the rear metallic electrode of the cell. Finite Difference Time Domain simulations are used to explore the absorption of light within the solar cell structure, building on similar work by Abass *et al.* [1] and Sefunc *et al.* [2]. Planar devices can be optimised by altering the layer thicknesses to achieve optimal absorption within the photoactive region. When gratings are incorporated, they are found to have significant effects on the absorption within the active layer, due to the excitation of surface plasmons, total internal reflection, and shifts in interference within the multilayer stack. The enhancements are analysed in greater detail by comparing with dispersion plots generated both theoretically and using further simulations, and provide a useful reference for future device design. Devices incorporating triangular, rectangular, and sinusoidal gratings, using both silver and aluminium electrodes, are investigated and demonstrate enhancements compared to optimised planar devices of up to 10% and 4.5% respectively using a triangular grating. Aluminium is therefore shown to be a useful material in the design of plasmonic solar cells incorporating gratings. Rectangular and sinusoidal gratings are also shown to provide enhancements of up to 6.5% and 8% respectively for silver gratings. Devices incorporating 2D gratings are shown to have similar enhancements and are insensitive to incident polarisation. Devices incorporating gratings display broad intolerance to grating parameters and good insensitivity to the angle of incidence up to around 15°. Factors that influence absorption in practical devices incorporating gratings such as illumination conditions and choice of substrate are discussed. Alternative active layer materials are discussed in terms of their likely impact on featured devices, including the effect of the introduction of additional

layers. Practical steps towards the fabrication of experimental devices are described, including a demonstration of the use of a Focussed Ion Beam technique to generate ridges with periodicity down to 300 nm. Transfer to a soft intermediate polymer PDMS is also demonstrated through a simple method with very high fidelity.

Contents

List of Figures

List of Tables

CHAPTER 1

Introduction and Research Review

1.1 Project goals

In the design of solar cells, the ultimate aim is to extract energy from sunlight as efficiently as possible. There are a variety of avenues of research aiming to achieve this, often focussed on the materials employed and device structure. In this project, I will explore optical methods to improve the devices. In essence, I will attempt to manipulate the passage of light through the device in order to absorb more photons within the photoactive region. I will focus on organic solar cells, which are appealing due to their low cost and the potential to scale their production using systems such as roll-to-roll processing. Whilst much progress has been made in the highly competitive

field of solar cell design, I aim to bring additional clarity to the area by providing a comparison of structures that can be employed with a clear focus on experimental realisation. I aim to provide a realistic appraisal of the mechanisms of enhancement and the potential that optical methods have to improve the efficiency of organic solar cell devices.

1.2 Thesis outline

I begin this thesis by setting my work in the context of current photovoltaic research in Chapter 1. I provide an overview of solar cell technologies, before focussing on organic solar cells which are the subject of my work. The structure, fabrication, and device operation of organic solar cells are of great relevance to my work and I therefore briefly summarise the details of these. In addition, I provide a background to the underlying science which underpins my research. I have then included a short review of the relevant literature which seeks to address the same goals as my project, albeit often from a different but comparable angle.

In this project, I aim to dissect the important physics underlying the enhancement of thin film organic solar cell devices. I therefore provide a basic summary of the underlying theoretical concepts in Chapter 2 including a mathematical description, where relevant. I also take this opportunity to describe the background theory to the simulation techniques I make heavy use of during my research. In Chapters 3 to 6, I detail the research that I have conducted over the course of my project. In Chapter 3, I investigate the optimisation of planar devices, and how the absorption is altered with the addition of a grating incorporated into the rear contact of organic solar cell devices. This leads to a discussion of the mechanisms by which the changes in the absorption are brought about. Chapter 4 details further investigation into the design of grating structures. I also detail the progress made in optimising the geometry of the structured electrodes to improve their optical performance under normal incidence. In Chapter 5, I describe additional considerations for devices employed under real world conditions. In Chapter 6, I describe the steps taking towards the experimental realisation of the theoretical structure I have optimised. The thesis concludes with Chapter 7, which draws together the principal findings of

my research.

1.3 Solar Cells

1.3.1 Introduction

The challenge of anthropogenic climate change has driven multiple avenues of research into technologies to reduce our dependence on fossil fuels. The Sun is the ultimate source of nearly all our energy and irradiates the Earth's surface at a rate of approximately $1000\,\mathrm{Wm}^{-2}$. If we can harness a small fraction of this energy, we have the means to meet our energy needs for the foreseeable future. Photovoltaics are devices which convert the energy from the Sun directly into electrical energy. This direct conversion is appealing in its simplicity. Complete devices that achieve this conversion are known as solar cells.

Solar cell technologies are broadly categorised into generations, with more recent technologies occupying the later generations. There is some debate over the exact classifications, particularly with regards to the later generations, but I put forward a common description here. First generation solar cells included thick mono-crystalline silicon cells. These provide relatively high efficiencies, but are also relatively expensive due to the high costs of the mono-crystalline silicon fabrication process. Extremely pure crystals are required, as defects strongly impair the efficiencies of these devices. Thick cells are employed in order to achieve maximal absorption by increasing the path length of light passing through the device.

Second generation cells aim to address the cost issue by employing thin film technologies. The trade-off is the decrease in absorption due to the reduced path length. Examples of materials used include amorphous silicon, Copper Indium Gallium Selenide (CIGS), and Cadmium Telluride (CdTe). These cells, whilst lower in cost due

to the reduced material costs of employing thin films, also currently have relatively low efficiencies compared to first generation cells.

Third generation cells incorporate many different technologies with the aim of further reducing costs compared to second generation cells, whilst also increasing efficiencies. Examples include quantum dot solar cells, inorganic cells based on III/V materials such as GaAs, tandem cells, Dye Sensitised Solar Cells (DSSCs), and organic/polymer solar cells.

Fourth generation cells employ inorganic structures within organic devices to improve both optical and electronic properties of these devices [3]. Into this category fall organic solar cells incorporating nano-structured metals, which are used to enhance efficiencies through plasmonics. It is this final class that forms the focus of this investigation.

1.3.2 Organic solar cells

This work focusses on organic solar cells, which offer an attractive means to produce solar energy as they are cheap and the manufacturing process can be scaled for high device throughput [4, 5]. These devices comprise a number of thin layers, as shown in Figure 1.1, where the layers are ordered according to the current standard geometry. Light is incident on the device through a transparent front conductor, typically Indium Tin Oxide (ITO). The light then passes through an optional electron blocking layer such as poly[3,4-ethylenedioxythiophene]:poly[styrenesulphonate] (PEDOT:PSS) before reaching the active layer, where the majority of useful photoexcited charge is generated. There is then an optional hole blocking layer, followed by a rear metallic contact. The devices are frequently built on a glass substrate, although there is the potential to develop them on flexible substrates. The blocking layers improve the

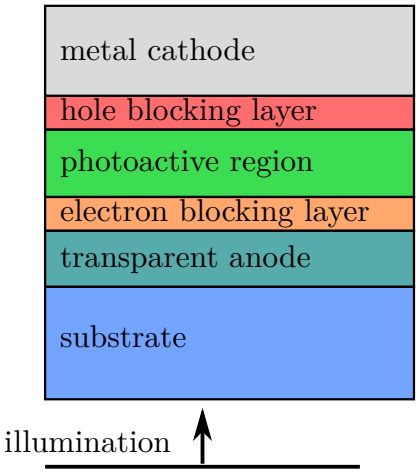

Figure 1.1 Generic organic solar cell structure in the standard geometry.

current extraction properties of the device by promoting charge carrier transport or providing an improved contact with the external electrodes by matching the work function.

In standard geometry devices, the metal back contact serves as a cathode and the front contact as the anode. The front contact must therefore be as transparent as possible in order to admit as much light as possible into the device. Devices are also studied in an inverted geometry, in which the roles of the front and back contacts are reversed, such that the front contact is the cathode, and the rear contact is the anode [6]. This often necessitates a change in the order and materials of the blocking layers surrounding the photoactive layer.

The photoactive materials used within the device are commonly a conjugated polymer as the electron donor, and a fullerene-based material as the electron acceptor. In this thesis, the materials studied are the polymer Poly(3-hexylthiophene-2,5-diyl) (P3HT) and the fullerene-based material Phenyl-C61-butyric acid methyl ester (PCBM). These are well studied materials which serve as an instructive benchmark upon which to make improvements via optical methods. The best P3HT:PCBM-based cells currently have photocurrent efficiencies around 5% [7–9], though other polymer

blends achieve efficiencies exceeding 10% [10].

1.3.3 Fabrication

First generation silicon solar cells are fabricated from thin, doped, mono-crystalline wafers which have been highly polished. The opposing dopant is diffused into the wafer from one side leading to a p-n junction. This is an expensive and low throughput methodology. In contrast, organic solar cells are formed by depositing a number of thin layers onto a substrate. This can be achieved at significantly reduced cost and improved scalability.

A common method for the fabrication of organic solar cells includes solution processing. In this case, the layers are dissolved in solvents and deposited sequentially onto a substrate. The substrate is typically coated in a transparent conductor such as ITO which has been applied using physical vapour deposition. The PEDOT:PSS is dissolved in water, and the photoactive materials are dissolved in an organic solvent such as chlorobenzene or dichlorobenzene.

A typical method for depositing the layers is spin-coating, in which the substrate is mounted on a rotating chuck and the solutions are dropped onto the substrate. The centrifugal force on the solution spreads it across the substrate, whilst also drying the solvent. The uniformity and thickness of the resulting layer is a function of acceleration, final spin speed, and time. Finally, the rear contact is deposited on the back of the cell. In the case of a metal contact this is typically performed using thermal evaporation under low vacuum. At least one annealing stage is usually employed to improve the performance of the final devices.

Other fabrication methods include thermal evaporation of the layers of the device [4].

This requires materials that are thermally stable, which precludes large molecular mass materials. The evaporation is usually performed under vacuum to prevent contaminants being incorporated into the devices and to ensure that the layers are deposited uniformly.

In order to achieve a high manufacturing throughput, roll-to-roll processes can be employed in order to achieve a rapid throughput. In this case, the substrate is passed through rollers and the layers are deposited by a number of different methods, including gravure, flexographic, screen, and inkjet printing [11]. There are also vacuum assisted methods of roll-to-roll processing. The potential to fabricate a high volume of devices in a short time scale is a strong motivation for research into organic solar cell technologies, as it reduces costs and increases global capacity.

These fabrication methods have a strong influence on the types of additional optical structures that can be incorporated into devices. The sequential deposition of layers allows the incorporation of optical structures deep within the devices, for example. In addition, it would be beneficial to utilise structures that are compatible with high throughput fabrication methods such as roll-to-roll processing.

1.3.4 Device operation

When a typical organic device is illuminated, a photon is absorbed in one of the active materials, creating a bound electron-hole pair known as a Frenkel exciton [12, 13]. These excitons rapidly recombine and have a diffusion length of between 1 nm to 10 nm [14]. If the exciton diffuses to an appropriate interface before recombination, it can dissociate into an electron and hole. This occurs due to the lower energy in both the highest occupied molecular orbital (HOMO) and lowest unoccupied molecular orbital (LUMO) of the electron donor material compared to the acceptor.

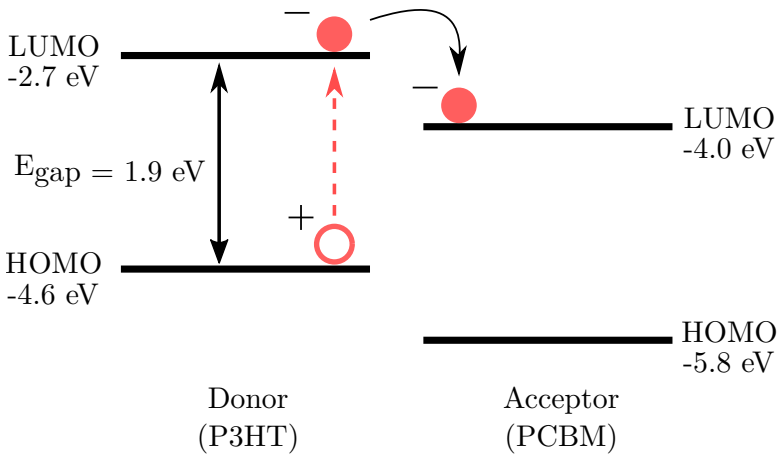

Figure 1.2 Schematic of the HOMO-LUMO in a P3HT:PCBM organic solar cell, demonstrating the excitation of an electron to the LUMO. The energy gap of the donor is labelled E_{gap}. Data for energy levels are obtained from the literature [20].

The energy levels comprising the HOMO and LUMO arise from the hybridisation states of the π-conjugated organic molecules of the photoactive materials. The HOMO and LUMO can be compared to the valence and conduction bands, respectively, in inorganic solar cell devices. Charge transfer can occur from the exciton such that the electron is transferred to the LUMO of the acceptor and the hole is left in the HOMO of the donor. This occurs if the difference in energy between the HOMO and LUMO is smaller than the binding energy of the exciton, as the separated state is therefore energetically favourable [15]. This process of electron transfer is illustrated in Figure 1.2. Some of the first authors to demonstrate this were Sariciftci *et al.* [16].

After this transfer process, the electron and hole are still attracted to one another via Coulomb forces and are known as a geminate pair. The electron and hole in this charge transfer (CT) state must then dissociate further to form a charge separated state (CS) as they migrate to their respective electrodes, where they flow into the external circuit. The exact process by which this occurs is somewhat disputed, with older theories based on Onsager's theory [17], adapted by Braun [18], competing with theories based on hot CT states [19], amongst others.

The potential difference across the cell is governed by the difference between the electron and hole chemical potentials (quasi-Fermi levels) which is related strongly to the energy difference between the HOMO and LUMO of the photoactive polymer [21, 22].

Organic cells display very poor charge mobilities [23], compared to silicon cells, of around $10^{-7}\,\mathrm{m^2V^{-1}s^{-1}}$ to $10^{-8}\,\mathrm{m^2V^{-1}s^{-1}}$ [24] and therefore act as insulators for many purposes. The photo-excited excitons rapidly recombine and it is therefore important that absorption takes place close to the donor-acceptor interface, within the diffusion length of the exciton [14]. This has led to the predominance of the bulk heterojunction geometry for polymer-based cells. In this case, rather than a simple planar heterojunction between the electron donor and acceptor, the two materials form a large interfacial area through phase separation. This provides a small path length to the interface and increases the likelihood that photogenerated excitons can diffuse to the interface before recombination.

The poor charge mobility also means that the distance between the interface and electrodes must be small, such that after charge separation has occurred at the heterojunction, the electron and hole can be extracted before significant recombination occurs. For this reason, the photoactive layer is very thin, typically on the length-scale of one hundred nanometres [13].

The thin photoactive layer additionally results in a short optical path length which limits the efficiency of these devices [23, 25]. There is clearly, therefore, a balance to be struck in using cells with a thin active layer to improve charge extraction and keep costs down, whilst maintaining adequate path length for absorption. One prominent method for achieving this balance is to use alternative materials for the active layer that absorb strongly and have good charge extraction properties. This has led to the development of alternative polymers with low bandgaps, such

as Poly[[4,8-bis[(2-ethylhexyl)oxy]benzo[1,2-b:4,5-b']dithiophene-2,6-diyl][3-fluoro-2-[(2-ethylhexyl)carbonyl]thieno[3,4-b]thiophenediyl]] (PTB7)[26], which leads to efficiencies up to 8.4% [27], or 9.2% in the inverted geometry [6]. An alternative approach is to design optical structures in order to effect an increase in this optical path length, or alternatively to increase the near-field strength within the active region. One method to achieve such increases is through the use of plasmonics.

1.4 Plasmonics

1.4.1 Introduction

Plasmonics describes the interaction of light with quantised coherent free-metal electron oscillations, known as plasmons. The term 'plasmonics' was proposed by Maier *et al.* in 2001 as the sub-field of modern optics investigating these phenomena [28]. Desribing the process in more detail, a metal can be considered as a collection of fixed positive ions surrounded by a free electron gas or plasma, commonly referred to as a 'sea of electrons'. This electron cloud can oscillate with respect to the background ions under the influence of an external electromagnetic wave resulting in collective plasma oscillations. The quantisation of these oscillations is referred to as a bulk volume plasmon.

1.4.2 Surface plasmons

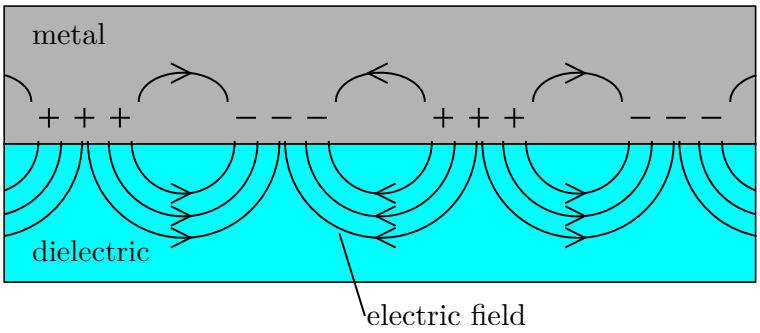

Figure 1.3 Schematic demonstrating the free electron displacement and resulting electric field of a surface plasmon polariton.

At an interface between two materials in which the real parts of the dielectric function

changes across the interface, such as a dielectric/metal, the electron plasma supports an additional form of electron oscillation, in which the electrons oscillate in a direction parallel to the interface. Energy is transmitted along the interface in a surface wave, and these waves were first considered in detail by Ritchie in 1957 [29]. Under a classical approach, Ritchie considered a semi-infinite medium with a planar interface to the vacuum. He predicted surface plasmons at a frequency $\omega_p/\sqrt{2}$ where ω_p is the bulk plasma frequency, as discussed in Section 2.2. He also predicted that these should be observable by energy loss spectra of fast electrons bombarding a metal film and this was confirmed by Powell & Swan (1959) [30, 31]. This description can be generalised to include interfaces between a non-absorbing half space (real, non-zero dielectric constant ϵ_2) and a metallic half space (complex dielectric constant $\epsilon_1(\omega)$), thus modelling a dielectric/metal interface [32]. The term 'surface plasmon' was coined by Stern & Ferrell in 1960 [33]. In addition, there is an electromagnetic field as a result of the charge oscillation, and the coupled charge oscillation and field is known as a surface plasmon polariton (SPP). The effect is illustrated in Figure 1.3.

The fields associated with the SPP are strongly confined at the interface, and have a higher intensity than the incident field. The field decays in an evanescent manner into the metal, where there is large absorption, and the penetration into the metal is described by an effective skin depth. There is a far slower decay into the dielectric, as illustrated in Figure 1.4. In addition, the propagation length of the SPP is relatively long. These latter properties, along with the high field intensity, make SPPs highly useful for practical applications.

Surface plasmon polaritons can be excited by firing electrons into a suitable metal, as occurs during energy loss spectroscopy from fast electrons. The inelastic scattering of the electrons when they enter the material leads to energy transfer and the excitation of the SPPs. By measuring the angular distribution and energy distribution of the

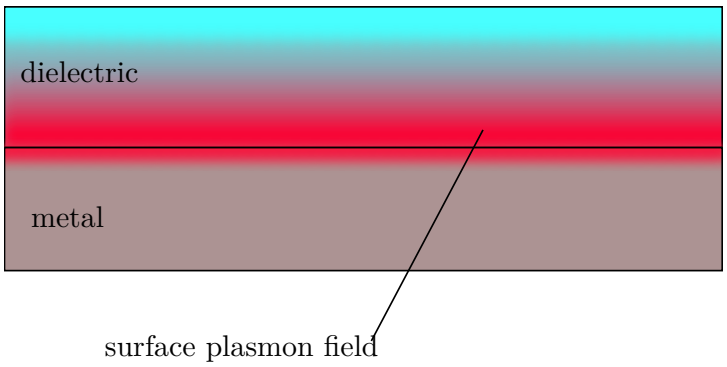

Figure 1.4 Schematic demonstrating the confined fields of a surface plasmon at an interface between a metal and a dielectric.

scattered electrons passing through a thin film of the material, the SPPs can be observed.

SPPs can also be excited by incident photons, and the resultant oscillation has a shorter wavelength than the excitation wavelength. SPPs cannot be directly excited by photons in free space, however, due to a momentum mismatch between the two. There are a number of methods to supply additional in-plane momentum in order to allow the coupling into the SPP mode. These methods include prism coupling via the Kretschmann [34] and Otto [35] configurations, and grating coupling [36]. These coupling systems are illustrated in Figure 1.5. The coupling to surface plasmons via a grating offered an explanation to the Wood's anomaly first observed in 1902 [37].

1.4.3 Gratings

Building on the theory of surface plasmons at planar interfaces, there is a large body of work investigating the properties of gratings and how they can be used to couple light into surface plasmon modes. As discussed, the incorporation of a grating allows

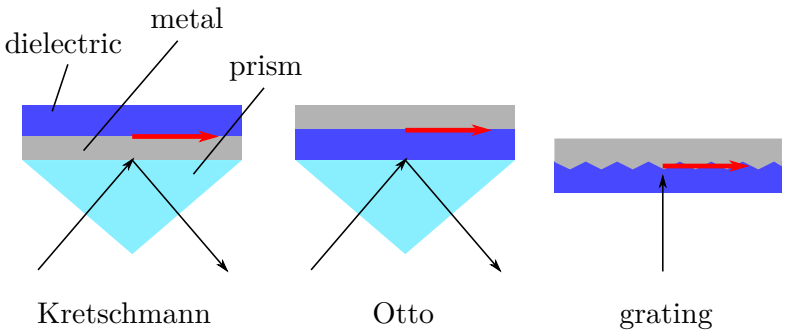

Figure 1.5 Schematic of the excitation of surface plasmon polaritons.

coupling between non-radiative surface plasmon modes and light.

For gratings with small amplitudes, perturbation theory [38] can be used to describe the interaction of light with the grating [39]. In general, Greene's functions [38] or other formalisms such as that proposed by Chandezon *et al.* [40] can be employed. These theoretical models can be correlated both with prior theoretical results and also experiments. Experimental measurements are typically taken by measuring the transmission or reflection from a sample as the angle of incidence is altered [41]. Alternatively, the transmission [42] or reflection [43] from a plasmonic sample can be directly imaged in k-space.

For small amplitudes, the surface plasmon dispersion does not deviate significantly from the planar interface equation. The periodicity of the grating, however, gives rise to a band structure analogous to those that exist due to the periodicity of a crystal lattice in condensed matter physics. A small band gap can open up at the Brillouin zone boundary at even modest grating heights [32]. As the depth of the grating increases, the surface plasmon dispersion deviates from the planar interface equation. For deep gratings, localised modes within the groove itself lead to an increased band gap at the zone boundary, even for gratings with sub-wavelength periodicity, and can be excited at normal incidence [44]. Energy gaps can also open up as a result of

standing waves from left and right propagating surface plasmon modes as a result of additional grating components [45, 46].

In this thesis, relatively low aspect ratio gratings will be employed, for which the surface plasmon dispersion will not make significant deviations from the planar case. Gratings with large amplitudes would not be feasible due to the thin active layer present in fabricated devices. It is, however, instructive to bear in mind that higher aspect ratio regimes exist and could be employed in alternative device geometries.

1.4.4 Localised surface plasmons

If the surface plasmon interaction, described above, is confined within a small particle whose size is comparable to the wavelength of the incident light, it is described as a localised plasmon (LSP). When the size of the sphere is much smaller than the wavelength of the incident light, a quasi-static approximation is applied. In this case, the surface plasmon does not propagate along the interface due to the small finite size, and the electrons oscillate coherently inside the whole particle. This is demonstrated in Figure 1.6. The incident field induces a dipole in the sphere as polarisation charges build up on the surface. This occurs resonantly at the dipole plasmon frequency [47]. LSPs lead to an enhanced near-field electromagnetic field surrounding the particles which has been employed to enhance efficiencies in several photovoltaic technologies.

The first detailed quantitative description of LSPs was made by Mie in 1908 [48]. The theory developed in this paper, now referred to as Mie theory, describes the absorption and scattering of light by a metal sphere. Mie's method is to solve the vector wave equation in spherical polar coordinates, centred on the sphere. The vector spherical harmonics are calculated and any solution to the vector wave equation

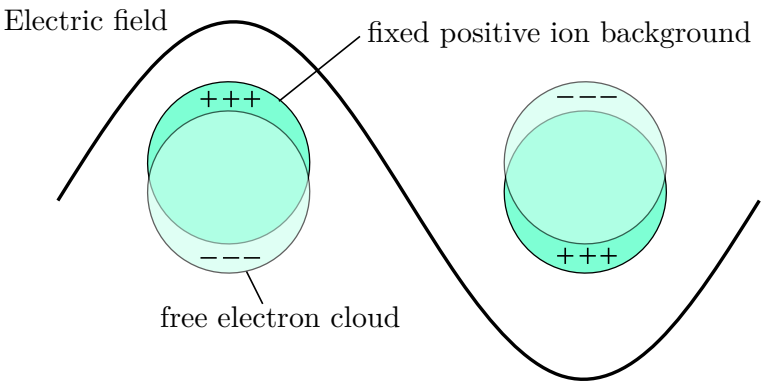

Figure 1.6 Schematic diagram of a metallic nanoparticle under the action of an electric field leading to a localised surface plasmon.

can be written as an infinite series expansion of these harmonics. An incident plane wave of the form $E_x = E_0 e^{ik_x}$ and the internal field are then expanded in vector spherical harmonics. Boundary conditions are finally employed to obtain the solution as an infinite series of spherical vector harmonics. The first term in the expansion, the dipolar term, is typically dominant. The effect of this dipolar response is a strongly enhanced near field at the resonant frequency and enhanced absorption and scattering cross-sections. For larger particles it is necessary to include higher order modes, principally the quadrupolar mode.

The dipolar and quadrupolar scattering profiles display distinct differences. The dipole mode scatters equally in the forward and backward directions. In contrast, the quadrupolar mode scatters preferentially in the forward direction. This has implications when deciding on the size and position of any nanoparticles used for plasmonic scattering enhancement for a given application. There are many additional factors influencing the exact frequency response of localised surface plasmons, including particle size, shape and dielectric environment [47, 49].

1.5 Plasmonics and solar cells

1.5.1 Introduction

Metallic nano-structures can be used to increase optical absorption by exciting surface plasmon modes within the photoactive region. These are excited by the incident solar radiation and lead to enhanced near-field intensity and an increased optical path length via scattering effects. This may allow increased absorption and by extension photocurrent generation within the cell, without increasing cell thickness. In this way, one of the principal negative impacts of using a thin cell is mitigated. Such an approach has been demonstrated in several device architectures including silicon and organic solar cells using both nanoparticles, and nano-structured electrodes.

In this section, I will discuss some important papers which propose the use of nanostructures in the context of solar cells. The section is broken into two subsections; in the first of these, Section 1.5.2, there is a discussion of the use of nanoparticles, which provided some of the initial impetus to the field. Investigations into the use of nanoparticles also serve as an important comparison to alternative methods using structured electrodes. Much of the pioneering work investigating the use of nanoparticles was performed using silicon-based materials, so the section begins with a discussion of these papers. It then moves on to discuss investigations into the use of nanoparticles with organic devices, both in experiments and as simulations. The use of structured electrodes is described in Section 1.5.3. These papers are broadly divided into those that detail experimental results, and those that employ simulations.

1.5.2 Nanoparticles

Inorganic devices

Stuart and Hall were some of the first to demonstrate enhanced waveguiding using plasmonic scattering in semiconductors. They used metal island films to enhance absorption in silicon-on-insulator (SOI) photodiodes in their papers of 1996 [50] and 1998 [51]. The island films are formed by depositing a uniform layer of silver on the front silicon surface and then annealing it. The silver coalesces into islands with a distribution of diameters. This process is illustrated in Figure 1.7. In the first paper they measured significant broadband enhancement in photocurrent centred around 800 nm. This was improved upon in the latter paper in which they achieved an enhancement of nearly 20-fold at the same wavelength using a silver island plasmonic layer with mean particle diameter 108 nm. The authors attribute the enhancement to increased scattering efficiency of larger scattering particles and coupling between the resonant modes of the metal film and waveguide modes of the SOI structure.

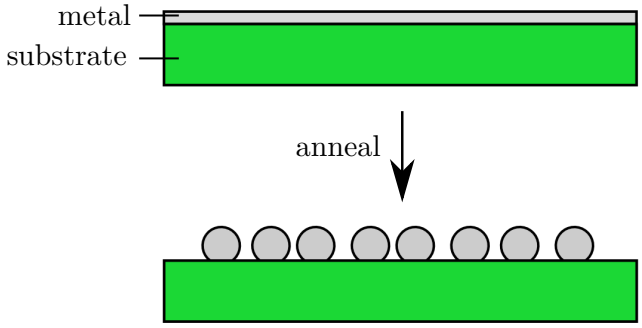

Figure 1.7 Schematic of the annealing process to form nanoparticles from a thin film of metal evaporated on a substrate.

Further work on silicon photodiodes has been performed by Lim *et al.* in 2007 [52]. They plotted the relative photocurrent enhancement of photodiodes with and without gold nanoparticles and observed enhancement at the longer wavelengths broadly

centred around 680 nm and a decrease at shorter wavelengths below 650 nm. The decrease was attributed to interference effects between the scattered and transmitted waves. They suggest that phase mismatch between the waves causes destructive interference and therefore a reduction in field amplitude. More recently, Temple *et al.* have suggested that this decrease may in fact be due to the poor radiative efficiency of the gold nanoparticles at these wavelengths as they display absorption in this region [53].

Pillai et al. were some of the first to apply plasmonic techniques explicitly to solar cells [54]. They compared enhancements for thin-film SOI and thick wafer-based solar cells. Each was coated with silver nanoparticles by depositing a thin uniform layer of silver and then annealing to form silver islands, in a similar method to that of Stuart and Hall previously [51]. Pillai *et al.* used theoretical modelling in which they treated the nanoparticles as interacting dipoles to model the absorption enhancement as well as performing experimental measurements. They noticed significant photocurrent enhancements throughout the visible and near-infrared regions with particular enhancements at 1050 nm, approaching the band gap of silicon, using the SOI cells. They found smaller enhancements for the thick wafer-based silicon cell. The enhancement results should ideally be viewed in conjunction with an absolute photocurrent vs wavelength plot in order to assess whether the enhancements occur within regions of the spectrum at which significant improvements in power conversion efficiency can be made. In this case, the enhancements fall close to the band gap where absorption is typically weak. It could be argued that this is beneficial as the cell will absorb photons which would otherwise have passed straight through. Alternatively, it could be argued that there is so little absorption at this wavelength that an enhancement in this region is futile.

Similar enhancements have been demonstrated using thin-film devices, beginning

with amorphous-silicon (a-Si) solar cells. Matheu *et al.* have demonstrated increases in power conversion efficiency (PCE) up to 2.8% using 100 nm gold nanoparticles [55]. Interestingly, they obtained an even greater enhancement of 8.8% using silica nanoparticles. The silica particles do not display a plasmonic response, but still scatter light into the lateral plane. Their response can be described using Mie theory in the same way as metallic particles. Matheu et al. also suggest that silica nanoparticles might find a use in organic solar cells. Further work within the same group has focused on hydrogenated amorphous silicon (a-Si:H) solar cells [56]. They report increases in PCE of 8.3% using gold nanoparticles at a concentration of $3.7 \times 10^8\,\mathrm{cm}^2$ but suggest that greater enhancements could be obtained using higher particle densities.

Organic devices: experimental

Whilst results from silicon technologies can prove instructive, when plasmonic techniques are applied to organic solar cells there are subtly different requirements. A major difference lies in the different absorption profiles of the two materials. Silicon absorbs up to its bandgap at 1.11 eV corresponding to light with wavelength around 1120 nm. A P3HT:PCBM blend, in contrast, absorbs strongly but only in the region of 300 nm to 900 nm, and has a steep shoulder around 700 nm. This affects the necessary wavelength tuning of the response from any plasmonic features. In addition, the thin active layer in these devices strongly dictates the dimensions of the features that can be employed. It also precludes the use of simple wave-guiding modes, as these would not be supported in such a thin structure.

The different fabrication methods between silicon and organic devices also preclude and permit different mechanisms to incorporate plasmonics structures into devices. The annealing technique employed by Stuart & Hall [50] and others to form metallic

nanoparticles is not applicable to the rear contact of organic devices as the temperatures required to anneal the metals would destroy the photoactive materials. Organic devices open up new possibilities, however, as the layer by layer growth of these devices permits the incorporation of colloidal nanoparticles within the structure in a manner that isn't possible with a crystalline inorganic device.

An early paper in which plasmonic techniques were applied to organic solar cells was published in 1995 by Stenzel *et al.* [57]. They employed metallic nanospheres to enhance the efficiency of copper phthalocyanine (CuPc) organic solar cells. The particles were incorporated between the ITO and active layer. They demonstrated photocurrent enhancement across the solar spectrum, with particular enhancements at shorter wavelengths. They report the best results using copper nanoparticles, for which they find an enhancement of 170% in photocurrent density. They employ an interesting technique whereby Fabry-Perot interference is filtered out of the spectra. This interference will arise due to interference between reflections at the various layers in the photovoltaic stack. Removing such resonances from the spectra helps to assess the true origin of any plasmonic enhancement. The authors attribute the broad enhancement to the large distribution of shapes within the nanoparticles which lead to a broad range of resonance frequencies. They also note that the metallic particles could not be placed at the electrode where the absorption of photons most likely leads to an extracted charge, as the particles would disrupt the ohmic contact. Westphalen et al. have demonstrated similar enhancements using zinc phthalocyanine (ZnPc) solar cells [58]. Nanoparticles were formed on the ITO substrate by tempering an evaporated thin silver island film, prior to deposition of the ZnPC active layer.

More recently, Morfa *et al.* (2008) have utilised similar techniques and applied them to P3HT:PCBM cells [59]. In this paper, the group prepare their samples by annealing a thin silver island on the ITO substrate, which is robust to the temperatures

involved. The resulting silver nanoparticles are located at the front of the device where incident light enters the cell and are embedded in the PEDOT:PSS layer when this is subsequently deposited. The photon-current conversion efficiency was measured as a function of wavelength and current-voltage measurements were also performed. The authors noted an overall increase in PCE from 1.31% to 2.23% under AM 1.5 illumination, a factor of approximately 1.7, using an initial 1 nm depth of silver, which is then annealed to form islands. This is an atypically high enhancement, and the reference devices were of somewhat low efficiency. They observe a dip in the enhancement spectrum around 450 nm which corresponds to the resonant frequency of the silver particles at which they absorb strongly. The detriment caused by this absorption is an important consideration when employing nanoparticles within these devices. It has ramifications for the optimum location of the particles, as locating them at the front of the device will lead to unwanted absorption prior to reaching the active layer. For all but the thickest silver film the principal enhancements occur at wavelengths longer than about 500 nm. In addition, the authors note a slight decrease in the open circuit voltage of the cells with increasing silver thickness which may be due to decreasing work function of the Indium Tin Oxide (ITO) electrode due to the presence of the silver.

Morfa *et al.* attribute the improvements in efficiency they observed to the dramatically enhanced near-field electromagnetic enhancement around the metallic nanoparticles. This response drops off quickly with distance and so they suggest that the PEDOT:PSS layer must be kept thin so the fields do not decay excessively before reaching the photoactive layer. Kim *et al.* have reported similar increases in photocurrent efficiency from 3.05% to 3.69% using a similar device geometry and silver nanoparticles, which were formed instead using an electrodeposition technique [60]. In their experiments, the average particle size was approximately 13 nm. The particles were again formed on the ITO so were located at the front of the active

layer, which would have led to similar problems with absorption as noted above.

More recently, in 2013, Chen *et al.* presented experimental results in which they incorporated gold nanoparticles of various sizes into the PEDOT:PSS layer at the front of P3HT:PCBM based devices [61]. They achieve efficiency enhancements of up to 23% using 35 nm nanoparticles. They attribute their enhancements both to the excitation of LSPRs but also increased roughness in the PEDOT:PSS which leads to an increased interfacial area with the active layer. They note that there is a high degree of lateral confinement of the LSPR near-field in the PEDOT:PSS, such that particles that encroach on the active layer offer the largest plasmonic effect.

Organic devices: simulations

In addition to experimental results, simulations form a major avenue of research into optical designs for solar cells. Finite Difference Time Domain (FDTD) simulations were performed by Duche *et al.* [62] in 2009. In their paper they looked at a simple array of spheres within an MEH-PPV:PCBM photoactive region, but neglected electrical contacts and other layers that would be found in a real solar cell. They compute and compare the absorption of the devices with and without nanoparticles and also plot the spatial distribution of electromagnetic field power density. They note an increased power density between the nanoparticles within certain frequency ranges. Although not explicitly stated, this can be related back to near-field enhancement as suggested previously.

Additional simulations were performed by Shen *et al.* who used a Finite Element Modelling (FEM) technique to elucidate further the mechanism of enhancement in P3HT:PCBM solar cells [63]. The group modelled metallic nanoparticles embedded directly in the photoactive layer. The simulations were performed in 2D, so the

simulation models a periodic array of cylindrical nanowires. The authors investigated a number of parameters including layer thickness, particle spacing, particle diameter and particle coating. They ascribe the absorption enhancement to near-field enhancement of the electromagnetic field surrounding the nanoparticles, confirming the suggestions of previous papers. To reach this conclusion, the authors divided the simulation volume into three sub-regions and identified the region in which absorption enhancement occurs. Significant absorption was only noted in the middle sub-region, where the nanoparticles are located. This rough division leads them to suggest the enhancement arises from the near-field surrounding the nanoparticles.

Other interesting results arising from the Shen paper are that there is an optimum nanoparticle spacing. As the nanoparticles are moved farther apart, the average mode area increases, however the electric field enhancement gets smaller. The interplay between these competing factors leads to an optimum particle spacing. Particle diameter also has an effect on enhancements, as expected from previous results. The authors also note that nanoparticles that are not coated with silica can lead to quenching of the photogenerated excitons. Coating the particles, however, decreases the absorption enhancement so they suggest that the particles should be coated as thinly as possible. It is notable that the authors have used PEDOT:PSS as their front contact, which differs from the conventional ITO. They reasoned that indium, which is used in ITO, is a scarce material and that it is therefore preferable to use an alternative contact. In addition, they have employed 2D simulations which leads them to simulate cylinders rather than spheres. This might have a large influence on the frequency response of the plasmonic resonances. Finally, they do not mention whether they expect any disruption to the bulk heterojunction structure of the P3HT:PCBM blend due to the presence of nanoparticles within this layer.

In 2011, Kochergin *et al.* demonstrated a systematic approach to the use of nanopar-

ticles in organic photovoltaics, including P3HT:PCBM based cells [64]. They investigated the dependence on nanoparticle material and also nanoparticle fill factor using simulations under an effective medium approximation (EMA). They conclude that aluminium shows the greatest promise due to its higher plasma frequency leading its enhancement peak to overlap strongly with the absorption band of P3HT:PCBM and other photoactive polymer blends. There are, however, discrepancies when compared with experimental data within the paper. They attribute these to inaccuracies in the optical constants used for the polymer blend which were taken from literature values [63] and inaccuracies in the aluminium optical constants. There are also inherent deficiencies within the EMA method, particularly at long wavelengths where it neglects multipolar interactions.

Summary of nanoparticle papers

In summary, the use of nanoparticles in both silicon and organic solar cell devices has been demonstrated both experimentally and in simulations. The early work was performed using silicon devices, but enhancements have also been demonstrated in organic devices. There are a number of locations in which nanoparticles could be incorporated into these devices, as illustrated in Figure 1.8. Most experimental results place the particles at the front of the device, principally due to fabrication considerations. When the PEDOT:PSS or active layer is subsequently deposited, the particles are then embedded in this layer. This leads to unwanted absorption within the particles prior to reaching the active layer and has a detrimental effect on the absorption spectrum. The principal mechanisms of enhancement arising from the particles are attributed to increased near field intensity leading to increased absorption. To capitalise on this, the particles should be located as close to the active region as possible, and preferably within it. The particles will also have

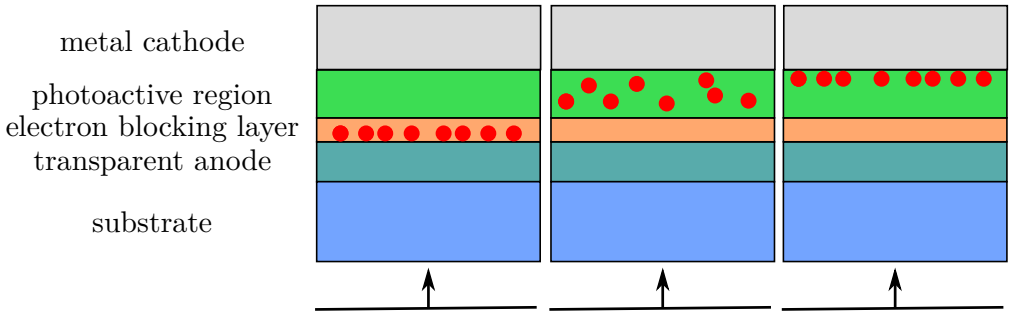

Figure 1.8 Potential location of nanoparticles to enhance thin film organic solar cells.

an influence on the electrical properties of the device, including charge extraction. Simulations permit the incorporation of the particles directly into the active region, but this is hampered experimentally by exciton quenching at the particle surface. This could be addressed by coating the particles in a dielectric, but this would reduce their efficacy as the enhancements derive from a near-field effect. Finally, recent experimental results from 2013 demonstrate actual enhancements of up to 23% using silver nanoparticles in P3HT:PCBM devices. This acts as a point of reference for other mechanisms of enhancement that I will go on to describe.

1.5.3 Structured electrodes

So far, I have focused on the use of nanoparticles as plasmonic features used to increase device efficiency by enhanced near-field, amongst other effects. This forms a useful and well developed point of reference by which to measure enhancements by other methods. As noted above, however, there are limitations imposed by the fabrication process which lead the particles in a suboptimal region of the cell, where unwanted absorption can occur. An alternative but related methodology to enhance

efficiencies is to exploit structuring of the rear electrode. This addresses some of the aforementioned concerns, but presents alternative challenges. The features are designed predominantly but not exclusively to provide coupling into surface plasmon modes by providing momentum in the directions parallel to the interface. The motivation for this is that surface plasmons have a long propagation length which should lead to a large path length through the active material. In addition, the structures can be placed at the rear electrode, and therefore would not interfere with the incident light.

Experimental

In order to fabricate nanoscale features, several papers have employed a low-cost scalable fabrication method known as nanoimprint lithography (NIL). This technique was first developed substantially by Chou *et al.* (1995) [65]. This group were able to fabricate a PMMA stamp with sub-24 nm features. The technique is illustrated schematically in Figure 1.9. A master mold was formed from silica on silicon and this was pressed into the thermoplastic polymer PMMA. The polymer and mold were first heated above the PMMA glass transition temperature T_g, so that the polymer behaved like a viscous liquid. They then let the temperature fall below the glass transition temperature, leaving an imprinted polymer layer when the mold was removed.

Roman *et al.* have used this nanoimprinting technique in 2000 to fabricate grating structures in organic solar cells [66]. They first formed an elastomeric polymer stamp, which was used in turn to nanoindent the photoactive layer. The elastomeric stamp was obtained by transferring a grating pattern from a commercially available template into an elastomeric polymer. They then used this elastomeric stamp to emboss the PTOPT/PCBM photoactive layer. Finally, they deposited an aluminium layer via

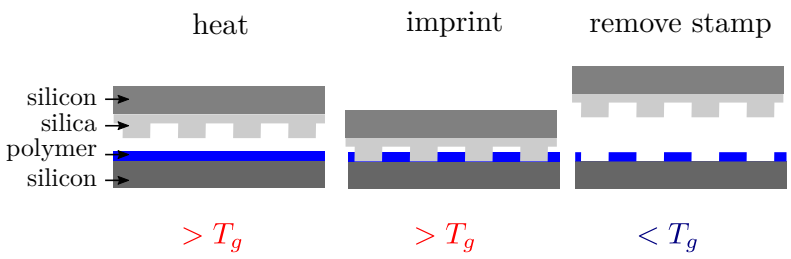

Figure 1.9 Schematic of the nanoimprinting technique developed by Chou *et al.* [65]. The polymer is imprinted by the stamp above its glass transition temperature. Once it has cooled below the glass transition temperature, the stamp is then removed.

vacuum evaporation; this electrode follows the contours of the stamped polymer to form a nanostructured electrode. The grating structure on the photoactive region was approximately triangular in shape with a periodicity of 416 nm and a height of approximately 15 nm. At the peak of absorbance within their photoactive layer, the authors note an increase in external quantum efficiency (EQE) of 26%, although absolute efficiencies were low. Through the use of optical modelling, the authors propose that the grating couples principally with the ITO contact due to its high refractive index, and the increase in efficiency in the photoactive layer is a collateral effect.

A few authors have described the use of the NIL technique to systematically enhance P3HT:PCBM solar cells. These papers vary principally in the fabrication of the master stamp and its exact geometry. Na *et al.* (2007) utilised a mold formed from the interference pattern of Ar^+ beams incident on a prepolymer which was then cured [67]. This creates a sinusoidal grating with a 500 nm period. The spectral enhancements they demonstrate in their incident photon to current efficiency (IPCE) measurements demonstrate broad enhancements. They demonstrated efficiency enhancements of 15% compared to the reference cell which had efficiencies of around 3.57%. They attribute their enhancements to the increased path length of light

through the active layer due to scattering from the grating.

Shih *et al.* (2009), on the other hand, used a textured silicon wafer with angular peaks formed through anisotropic etching [68]. This allows a large hard stamp to be formed which is then used to imprint the P3HT:PCBM active layer prior to cathode deposition. They obtain efficiency enhancements of 50% but note that the hydrostatic pressure applied during the imprinting has a large impact on the efficiency of the device itself. They suggest that the pressure provides an additional driving force for phase segregation in the bulk heterojunction. Investigations of the crystallinity of the P3HT after imprinting and annealing confirms an effect.

These last two papers do not directly attribute their enhancements to surface plasmons, although the period of the grating should lead to such an effect. I now discuss papers that make explicit mention of plasmonics as a mechanism of enhancement. In 2012, You *et al.* employed a grating to a low bandgap polymer PTB7:PCBM blend, that exhibits rather broader absorption than the P3HT:PCBM standard blend [69]. They employed an inverted device geometry, in which the ITO was followed by a layer of ZnO nanoparticles as an electron transport layer, then the active layer, and then a MoO_3 hole transport layer preceding the silver back contact. They used a rectangular grating, although the AFM scans in the paper reveal that this is somewhat smoothed at the corners. The periodicity and height of this grating are 700 nm and 40 nm, respectively. They obtain overall device efficiency improvements from 7.2% to 7.73%, and identify an enhancement due to a surface plasmon at long wavelengths around 770 nm.

More recently, in 2013, Li *et al.* employed 2D and 3D gratings to P3HT:PCBM cells in the inverted geometry [70]. The periodicity and height of the gratings were 350 nm and 55 nm, respectively. The 2D grating had a rectangular cross section and the 3D grating consisted of an array of nanopillars. The nanoimprinting method was used to

form the grating patterns on the active layer prior to deposition of a silver electrode. Starting with reference devices with efficiencies of 3.09%, they achieve enhancements of 17.5% and 24.6% for the 2D and 3D gratings, respectively, using the structured electrode. They note an increase in both the IPCE and the fill factor for devices incorporating the structured grating. The spectral measurements demonstrate a strong enhancement at long wavelengths of 700 nm and 650 nm for the 2D and 3D gratings, respectively, which they attribute to a surface plasmon.

In addition to the nanoimprinting methods used in the papers so far described, additional methods have been employed to fabricate structured electrodes. Tvingstedt *et al.* used a pre-structured aluminium cathode on which they deposited their polymer layers [71]. A thin layer of titanium was added to the aluminium electrode to facilitate charge extraction as it mitigates the negative impact of aluminium oxide. They utilised a polymer/PCBM photoactive layer, referred to as APFO Green5, and their front contact was formed from PEDOT:PSS. The grating had a period of 277 nm and a height of 50 nm. In addition to experimental results, they used a recursive Green's function technique to obtain theoretical results for the efficiencies of the cells. From their spectral absorption results, they demonstrate a particular absorption enhancement at around 550 nm. This corresponds to the surface plasmon resonance frequency and the simulations display a resonance at a similar frequency. Light polarised perpendicular to the grating excites the plasmonic response, whereas parallel polarisation does not. It is also worthy of note that in another experiment with a thicker polymer blend, the authors observe an absorption peak at 450 nm, which is a total internal reflection mode due to reflection at the polymer/air interface and grating. This additional mode could be useful to increase absorption but must be balanced against the disadvantages of employing a thicker cell, such as the increased distance for charge extraction.

Other groups have incorporated nanohole arrays into their electrodes to couple light into surface plasmons. This film acts as a transparent front electrode in place of Indium Tin Oxide. Locating the grating at the front contact differentiates it from the results previously described. The origin of this approach lies with a Nature paper by Ebbesen *et al.* (1998), which reports strongly enhanced transmission through metal films incorporating submicrometre cylindrical cavities [72]. At some frequencies, the transmitted power is twice that of the incident light and enhancements occur at wavelengths greater than the grating period. The increased transmission is attributed to surface plasmon effects. Groups based at the University of Minnesota have published papers detailing the use of similar structures as the front contact of their CuPc/C_{60} based solar cells in 2008 [73] and 2011 [74]. In the later paper the authors claim that a very thin front aluminium contact does not impact the electrical properties of the anode. In addition, the devices perform better than those employing with ITO, despite having a poorer transmission. They suggest that this is due to increased plasmonic response both through the excitation of surface plasmon modes and also increased near-fields.

Simulations

In addition to experimental results, there are a number of papers which focus on simulations to provide insight into enhancement via gratings. These include Min *et al.* (2010) who simulate a rectangular grating within the PEDOT:PSS layer of a CuPc:PTCBi planar heterojunction organic solar cell [75]. This grating extends right through this layer to the CuPc active region. They identify enhancement due to a surface plasmon mode at the silver/organic interface. They also note the dependence of their enhancements on the width of the grating employed. The results are also polarisation dependent, as expected from a surface plasmon. Whilst these results

provide a useful demonstration of surface plasmon enhancement, there has currently been a move towards bulk heterojunctions employing different photoactive materials due to preferable charge extraction properties, as previously discussed. This presents a very different cell geometry which may require a totally different design for any plasmonic structures.

Abass *et al.* have used finite element modelling simulations to model triangular grating structures [1]. The simulation geometry is given in Figure 1.10. They have used a P3HT:PCBM polymer blend as a bulk heterojunction for their photoactive layer. They did not, however, include any conducting polymer or front contact layers. They calculate the absorption within the active layer by integrating over the divergence of the Poynting vector. They start by optimising the active layer thickness by identifying the interference maxima. They then note that the absorption spectra of a planar cell with no scattering features has a dip between 620-800 nm and so they targeted their plasmonic enhancements to this region. Overall, they achieve absorption enhancements of 15.6% under TM polarised light. As identified previously, this is the only polarisation that can achieve coupling into surface plasmon modes.

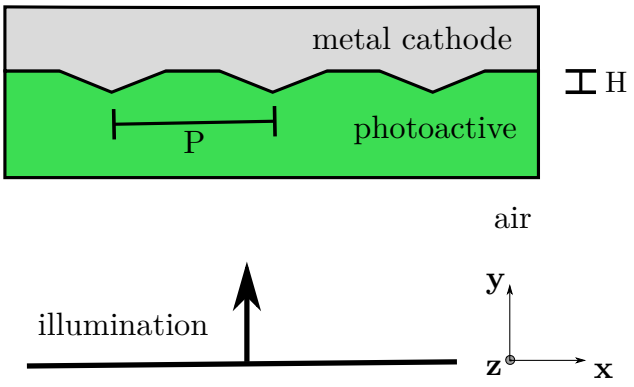

Figure 1.10 Simulation geometry employed by Abass *et al.* [1].

Abass *et al.* then attempt to identify how surface plasmon polaritons can be utilised. They estimate this by plotting how the grating periodicity will fold the band structure.

The grating periodicity is 300 nm, the thickness of the active layer is 150 nm and the height of the grating is 60 nm. They also vary the fill factor (base of triangle divided by period) between 1 and 0.5. The authors note an interesting splitting of the lower frequency mode. They refer to these as the 'dark' and 'bright' modes as the former cannot be excited at normal incidence with fill factor 0.5. They suggest that increasing the grating height leads to a flatter surface plasmon dispersion, therefore a more localised plasmonic response rather than propagation of the surface plasmon mode. They demonstrate this by running simulations with increasing grating height. In addition, they explore higher order plasmonic modes by increasing the grating period. They have also explored the use of gratings to excite polymer waveguide modes, which can occur with thicker polymer widths above 200 nm. Other simulations demonstrate localised modes by adding subwavelength grooves to their main periodic grating. This leads to multiple additional resonances in the spectra. Finally, they perform 3D simulations in which they demonstrate differing resonances but suggest that further study is required.

Sefunc *et al.* (2011) have presented FDTD simulations of P3HT:PCBM based solar cells using silver rectangular gratings [2]. They compared the effect of incorporating a grating into the PEDOT:PSS layer and also at the rear metallic contact. The geometries simulated are shown in Figure 1.11. Locating the grating before the active region leads to reflection that severely impairs the devices. In contrast, the rear grating leads to average absorption enhancements under both polarisations of up to 21% using a 140 nm grating. These enhancements drop off rapidly as the grating period is increased. By a grating period of 300 nm, the enhancement has dropped to around 16%. The absorption enhancements are compared to planar devices with the same initial thickness. This may not be a fair comparison given other optical effects that may occur due to the presence of the grating structure such as multilayer interference.

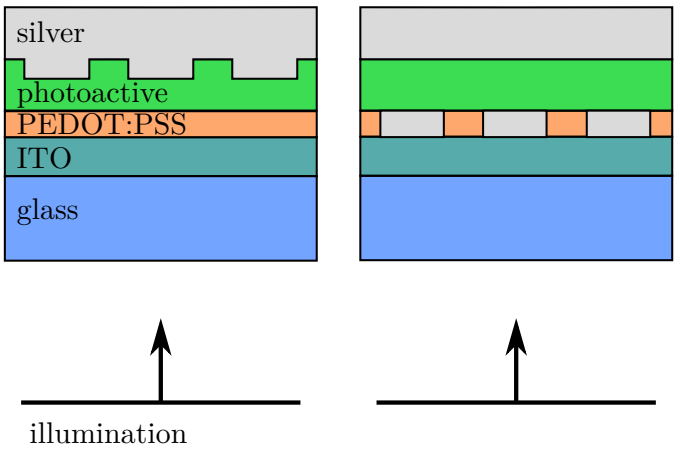

Figure 1.11 Geometry of simulations used in Sefunc *et al.* [2]

Summary of structured electrode papers

I have described a number of works that have incorporated structured electrodes into thin film organic solar cell devices in order to increase their efficiencies. Nanoimprint lithography shows particular promise due to its scalability, as one master stamp can be used to imprint multiple cells. In addition, it could potentially be incorporated into roll-to-roll based systems [76]. Recent experimental results incorporating gratings into the rear silver electrode have demonstrated device efficiency enhancements of 17.5% and 24.6% for 2D rectangular and 3D nanopillar gratings, respectively. These provide comparable enhancements to devices incorporating silver nanoparticles which demonstrate enhancements of up to 23%. Simulation results provide complementary information to the experimental work. Simulations of triangular gratings demonstrate enhancements of 15.6% under TM polarisation, and simulations of rectangular gratings demonstrate polarisation-averaged enhancements of up to 21%. The direct comparison of these results is hampered, however, as the device layer geometries simulated in both cases are very different.

1.6 Chapter summary

In this chapter, I have provided a brief overview of the solar cell device architectures that are currently under investigation. This led to a brief summary of the background to plasmonics, which is a field receiving increasing attention due to its application in a variety of fields including solar cells. A number of works have been described which investigate the use of nano-scale features to improve the efficiency of solar cell devices, with an emphasis on plasmonic enhancement. These broadly fall into two categories describing either simulations or experimental results, although there has been some attempt to match the two. I have described a variety of papers which have demonstrated enhancements in both inorganic semiconductor and organic devices. These technologies present largely different challenges due to both the geometry of the cells and also the materials employed. Significant enhancements have been demonstrated using both nanoparticles and structured electrodes.

The enhancements that have been demonstrated for P3HT:PCBM solar cells are summarised in Table 1.1. We see that the use of nanoparticles has demonstrated excellent enhancements, but these have only been reliably demonstrated using simulations of particles within the active layer. Structured rear electrodes can provide comparable enhancements to particles at the front of the devices and there is the scope for further enhancements. There is some debate surrounding the exact mechanisms of enhancement within the literature. The papers also vary greatly in the methods that are employed, and in the detail in which the devices have been investigated. In addition, there are a number of geometries and materials that are relatively unexplored.

With respect to gratings, which are the principal subject of this thesis, the previous focus has been on silver electrodes, as it is often assumed that these will provide the

Author	Enhancement	Efficiency	Type	Notes
Nanoparticles				
Morfa *et al.*[59]	70%	2.23%	experiment	Ag particles at front. Poor devices
Kim *et al.*[60]	21%	3.69%	experiment	Ag particles at front
Chen *et al.*[61]	23%	2.91%	experiment	Au particles at front
Shen *et al.*[63]	56%	N/A	simulation	Ag particles within active region
Kochergin *et al.*[64]	50%	N/A	simulation	Al particles within active region
Structured electrode				
Na *et al.*[67]	15%	4.11%	experiment	Ag sinusoidal
Li *et al.*[70]	17.5%/24.6%	3.63%/3.85%	experiment	Ag 2D rectangular/3D nanocylinder
Abass *et al.*[1]	15.6%	N/A	simulation	Ag triangular
Sefunc *et al.*[2]	21%	N/A	simulation	Ag rectangular

Table 1.1 Selected papers demonstrating enhancements in P3HT:PCBM solar cells using nanoparticles and structured electrodes. Absolute efficiencies are given for experimental devices.

strongest plasmonic response. There has been some attempt to assess the optimum parameters for enhancements using gratings, and a suggestion of the mechanisms of enhancement, but there is scope for further detailed simulations and analysis. In addition, the experimental work that has so far been performed demonstrates some promise, but a systematic study of grating geometries that correlate strongly with simulations is so far lacking.

1.7 Research outline

In this thesis, I aim to build on the work outlined so far in this chapter by providing a thorough analysis of the use of grating structures within organic solar cell devices to effect an increase in efficiency. The full device structure will be taken into account which will lead to a number of enhancements and detriments, not seen in simpler

simulations. I will then attempt to elucidate the mechanisms that lead to these effects, and their tolerance to grating geometry. This will lead to an optimisation of the device structure and a realistic appraisal of the efficacy of grating structures. In addition, I will compare both a silver and an aluminium grating and assess the relative merits of the two. I will also make comparisons between different grating geometries for both metals. To help guide the design of practical devices, I will investigate a number of factors that have direct implementations for practical devices, such as angle of incidence, illumination conditions, and material and device structure. Finally, I will describe experimental steps taken towards a practical realisation of these structures using a FIB method followed by soft lithography, which could prove valuable for further fundamental research into the use of grating structures in these devices in a systematic fashion.

CHAPTER 2

Theoretical Background

2.1 Introduction

In this section, I describe the theoretical background to the major topics introduced in the rest of this work. This theory underpins the discussion of the results in each of the remaining chapters. I begin by discussing the principles underlying plasmonics and gratings. Interference within a layered structure is then discussed, as this is relevant to layered organic solar cells. Finally, the theory underlying the Finite Difference Time Domain technique is discussed, as this technique was employed frequently throughout my research.

2.2 Plasmonics

2.2.1 Free electron model

As discussed in Section 1.4, a metal can be considered as a fixed positive ion lattice surrounded by a gas of free electrons. The approximation assumes that the ions are fixed and that there are no electron-electron interactions. When an alternating electric field is applied to the metal, the free electrons oscillate in response to this field but their motion is damped through collisions. Following the treatment in Maier [32], the equation of motion for each electron in the system is given by Equation (2.1a), where $\mathbf{E}(t)$ is the applied oscillating field with frequency ω, m is the mass of the electron, γ is the damping rate of the oscillations, and x is the displacement of the electron from the positive background. This is then solved for the displacement $\mathbf{x}$, in Equation (2.1b).

$$m_e\ddot{\mathbf{x}} + m_e\gamma\dot{\mathbf{x}} = -e\mathbf{E}(t) \tag{2.1a}$$

$$\mathbf{x} = \frac{e}{m_e(\omega^2 + i\gamma\omega)}\mathbf{E} \tag{2.1b}$$

The displacement of each electron leads to an overall polarisation $\mathbf{P} = -ne\mathbf{x}$ across the material, where n is the charge density. Using this in the equation for the displacement current $\mathbf{D} = \epsilon_0\mathbf{E} + \mathbf{P}$ leads to Equation (2.2c).

$$\mathbf{D} = \epsilon_0\mathbf{E} + \mathbf{P} \tag{2.2a}$$

$$= \epsilon_0 \left(1 - \frac{ne^2}{\epsilon_0 m_e(\omega^2 + i\gamma\omega)}\right)\mathbf{E} \tag{2.2b}$$

$$= \epsilon_0(1 - \frac{\omega_p^2}{w^2 + i\gamma\omega})\mathbf{E} \tag{2.2c}$$

In Equation (2.2b) the bulk or volume plasma frequency ω_p is defined, as given in Equation (2.3), where n is the charge density, ϵ_0 is the permittivity of free space and m_e is the effective mass of an electron.

$$\omega_p = \sqrt{\frac{ne^2}{\epsilon_0 m_e}} \tag{2.3}$$

Equation (2.2c) can now be compared against $\mathbf{D} = \epsilon_0\epsilon\mathbf{E}$ to obtain the permittivity of the free electron gas:

$$\epsilon(\omega) = 1 - \frac{\omega_p^2}{\omega^2 + i\gamma\omega} \tag{2.4}$$

This dielectric function is often known as the Drude model. At optical frequencies in particular, however, it gives a poor description of a real metal, due to interband transitions in that frequency region. Given that these are precisely the wavelengths of interest, a hybrid model incorporating Lorentz oscillators is often employed. Within this Drude-Lorentz model, the intraband (free electron) portion of the permittivity is treated as in the Drude model, and the interband (bound electron) portion as a sum of terms, as in the Lorentz oscillator model. The overall permittivity is therefore given by Equation (2.5), where ω_p is the bulk plasma frequency as before, Γ_j are damping factors and f_j are weighting factors [77]:

$$\epsilon_r(\omega) = 1 - \frac{f_0\omega_p^2}{\omega^2 - i\Gamma_0} + \sum_{j=1}^{n} \frac{f_j\omega_p^2}{\omega_j^2 - \omega^2 + i\omega\Gamma_j} \tag{2.5}$$

2.2.2 Volume plasmons

This section describes the theory underlying volume plasmons. We begin by taking Maxwell's curl equations in the following form:

$$\nabla \times \mathbf{E} = -\frac{\partial \mathbf{B}}{\partial t} \tag{2.6a}$$

$$\nabla \times \mathbf{H} = \mathbf{J_f} + \frac{\partial \mathbf{D}}{\partial t} \tag{2.6b}$$

Combining Equations (2.6a) and (2.6b) leads to a wave equation in the time domain, as given in Equation (2.7a). The solution of this equation describes the propagation of light through a medium. This can can be converted into the frequency domain via a Fourier Transform, giving the form shown in Equation (2.7b) [32], where $\mathbf{K}$ is the wave vector and indicates the direction of energy propagation in the wave.

$$\nabla \times \nabla \times \mathbf{E} = -\mu_0 \frac{\partial^2 \mathbf{D}}{\partial t^2} \tag{2.7a}$$

$$\mathbf{K}(\mathbf{K} \cdot \mathbf{E}) - K^2 \mathbf{E} = -\epsilon(\mathbf{K}, \omega) \frac{\omega_2}{c^2} \mathbf{E} \tag{2.7b}$$

Starting with Equation (2.7b), we can now consider the two cases of transverse and longitudinal travelling waves. In the former case, the wave vector is perpendicular to the electric field, such that $\mathbf{K} \cdot \mathbf{E} = 0$. In this case, a dispersion relation in the form $K^2 = \epsilon(\mathbf{K}, \omega)\frac{\omega^2}{c^2}$ is obtained. In the alternate case of longitudinal polarised waves, we obtain $\epsilon(\mathbf{K}, \omega) = 0$.

It is in the case of these longitudinal waves that the plasma frequency ω_p identified above takes on a special significance. It corresponds to the free collective oscillation frequency of the electron gas, such that all the electrons oscillate in phase. We consider an overall displacement x of the free electrons from the positive ion background. The displacement leads to a uniform electric field $E = \frac{nex}{\epsilon_0}$ through the material that acts to restore the electrons to their original position with a force $F = -neE$.

The electron cloud therefore collectively obeys the following equation:

$$nm_e\ddot{x} = -neE \tag{2.8a}$$

$$= -\frac{n^2e^2x}{\epsilon_0} \tag{2.8b}$$

$$\Rightarrow \ddot{x} = -\omega_p^2 x \tag{2.8c}$$

The plasma frequency is therefore the frequency at which the free electron gas would naturally oscillate. The quantised unit of this longitudinal plasma oscillation is referred to as a volume or bulk plasmon, and the energy of a collection of these is given by $\hbar\omega_p$ [78, 79].

2.2.3 Surface plasmons

The solution of Maxwell's equations at a suitable interface gives a propagating surface wave. We take an interface between two materials with permittivity ϵ_1 and ϵ_2, as shown in Figure 2.1. We consider a wave propagating in the x direction, with infinite planes in the y direction, and the interface between the materials occurring in the z direction, as shown. The macroscopic Maxwell's equations are used in the following form and are valid in the absence of external sources and for linear media such that

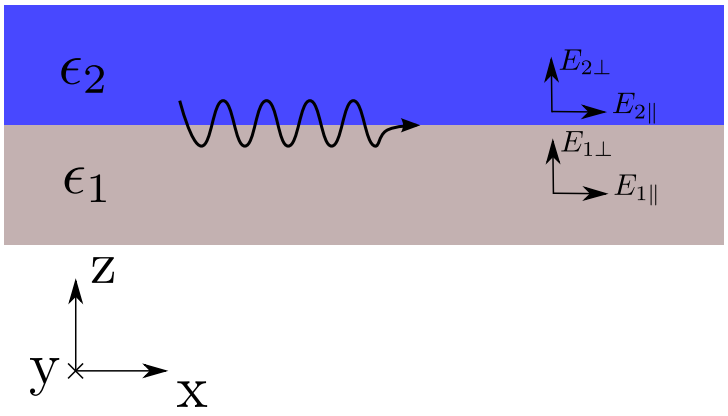

Figure 2.1 Schematic of a propagating surface plasmon wave at an interface between two materials.

$\mathbf{D} = \epsilon_0\epsilon\mathbf{E}$ and $\mathbf{H} = \frac{\mathbf{B}}{\mu_0\mu}$:

$$\nabla \cdot (\epsilon\mathbf{E}) = 0 \tag{2.9a}$$

$$\nabla \cdot \mathbf{H} = 0 \tag{2.9b}$$

$$\nabla \times \mathbf{E} = -\mu_0\mu\frac{\partial \mathbf{H}}{\partial t} \tag{2.9c}$$

$$\nabla \times \mathbf{H} = \epsilon_0\epsilon\frac{\partial \mathbf{E}}{\partial t} \tag{2.9d}$$

By taking the curl of Equation (2.9d), and using the curl vector identity along with the other Maxwell's equations, we obtain the wave equation given in Equation (2.10) for non-magnetic media, with a similar equation for the electric field.

$$\nabla^2\mathbf{H} - \frac{1}{c^2}\epsilon\frac{\partial^2\mathbf{H}}{\partial t^2} = 0 \tag{2.10}$$

We then assume that the fields are separable and periodic, such that the fields can be written $\mathbf{H}(\mathbf{x}, t) \sim \mathbf{H}(\mathbf{x})e^{i\omega t}$, leading to:

$$\nabla^2\mathbf{H} + \frac{\omega^2}{c^2}\epsilon H = 0 \tag{2.11}$$

$$\nabla^2\mathbf{H} + k_0^2\epsilon H = 0 \tag{2.12}$$

The formula for the surface plasmon wave must obey this wave equation. Only the TM polarisation solution exists as the TE polarisation, with the electric field oscillation parallel to the interface, is not supported [32]. This surface plasmon therefore only has electric field components in the x and z directions, and magnetic field components in the y direction. We are also looking for a confined field, such that the fields will exponentially decay in the z direction. For the spatial component of the magnetic component, we therefore seek a solution of the form:

$$H_y = Ae^{k_z z}e^{i(k_x x - i\omega t)} \tag{2.13}$$

Substituting 2.13 into the wave equation given in Equation (2.10), we obtain a solution provided that Equation (2.14) holds.

$$k_z = \sqrt{k_x^2 - k_0^2\epsilon} \tag{2.14}$$

Using the remaining curl equation, we also obtain the form of the electric fields,

leading to Equations (2.15a-c):

$$H_y = Ae^{k_z z}e^{i(k_x x - i\omega t)} \tag{2.15a}$$

$$E_x = -iA\frac{k_z}{\omega\epsilon_0\epsilon}e^{i(k_x x - i\omega t)} \tag{2.15b}$$

$$E_z = -A\frac{k_x}{\omega\epsilon_0\epsilon}e^{i(k_x x - i\omega t)} \tag{2.15c}$$

Taking an equation of this form in both media, labelling with subscripts 1 and 2, we obtain the two sets of equations given in (2.16a-b):

$$\left.\begin{aligned} H_{y,1} &= A_1 e^{k_{z,2} z}e^{i(k_{x,1} x - i\omega t)} \\ E_{x,1} &= -iA_1\frac{k_{z,1}}{\omega\epsilon_0\epsilon_1}e^{i(k_{x,1} x - i\omega t)} \\ E_{z,1} &= -A_1\frac{k_{x,1}}{\omega\epsilon_0\epsilon_1}e^{i(k_{x,1} x - i\omega t)} \end{aligned}\right\} \text{ medium 1} \tag{2.16a}$$

$$\left.\begin{aligned} H_{y,2} &= A_2 e^{-k_{z,2} z}e^{i(k_{x,2} x - i\omega t)} \\ E_{x,2} &= iA_2\frac{-k_{z,2}}{\omega\epsilon_0\epsilon_2}e^{i(k_{x,2} x - i\omega t)} \\ E_{z,2} &= -A_2\frac{-k_{x.2}}{\omega\epsilon_0\epsilon_2}e^{i(k_{x,2} x - i\omega t)} \end{aligned}\right\} \text{ medium 2} \tag{2.16b}$$

We then apply the boundary conditions such that the parallel component of the electric and magnetic fields are continuous. This leads to the requirements given in

Equations (2.17a-b):

$$A_1 = A_2 \tag{2.17a}$$

$$\frac{k_{z,1}}{\epsilon_1} = -\frac{k_{z,2}}{\epsilon_2} \tag{2.17b}$$

We require the fields to decay in the z direction for a physical solution, so the real parts of the dielectric function must be of opposite sign.

Using Equation (2.17b) in combination with Equation (2.14), we obtain the dispersion relation for the surface plasmon given in Equation (2.18). This is valid in general for complex values of both ϵ_1 and ϵ_2.

$$k_x = k_0\sqrt{\frac{\epsilon_1\epsilon_2}{\epsilon_1 + \epsilon_2}} \tag{2.18}$$

As an illustrative example, the dispersion relation for a perfect Drude metal/air interface with $\epsilon_1(\omega) = 1 - \frac{\omega_p^2}{\omega^2}$ and $\epsilon_2 = 1$ is plotted in Figure 2.2, normalised to the bulk plasma frequency. At short wavevector $\mathbf{k}$ (low frequencies), the wavevector approaches k_0 close to the the light line. At large wavevectors, the surface plasmon frequency approaches $\omega_{sp} = \frac{\omega_p}{\sqrt{1+\epsilon_2}}$. For an air interface with $\epsilon_2 = 1$, the Ritchie result $\omega_{sp} = \frac{\omega_p}{\sqrt{2}}$ is recovered [29].

It can be seen in Figure 2.2 that the surface plasmon dispersion always falls to the right of the light curve and is therefore non-radiative. This also means that it cannot be excited by an incident photon without additional momentum transfer, as previously discussed. This momentum can be provided by a prism, plasmonic

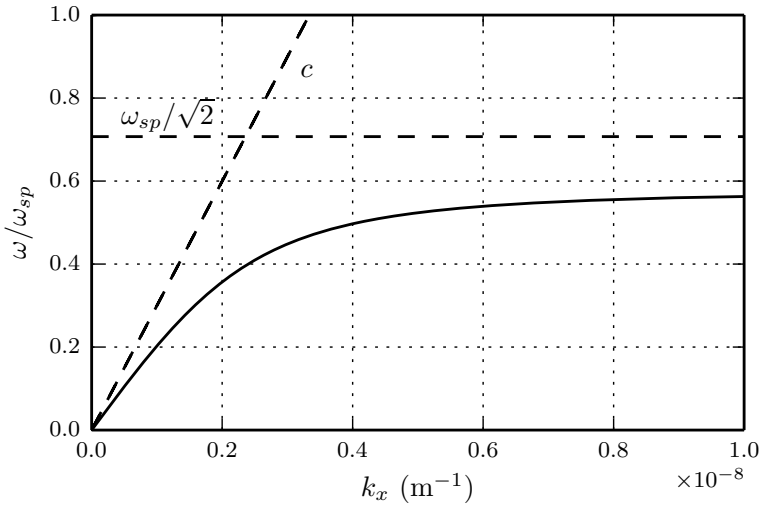

Figure 2.2 Dispersion relation for a surface plasmon formed at the interface between a Drude metal and air. The light line in air, and bulk plasma frequency of the metal are also shown.

scattering feature or grating.

As the field decays in the perpendicular direction, we can describe the confinement of the surface plasmon. In the metal we define a skin depth where the field decays by 1/e. This is given by $(\mathrm{Im}(k_z))^{-1}$, and at large wavevectors, at the surface plasmon condition, the surface plasmon is strongly confined to the surface with corresponding enhancement of the field. This confinement is relevant to the design of plasmonic enhancement features as it is most efficient to increase the electromagnetic field in regions of the device that contribute the majority of extracted charge carriers.

Surface plasmons propagate along the interface and lose energy due to the evanescent decay into the surrounding absorbing materials. The intensity of the surface plasmon decays as the square of the electric field leading to a propagation length of $L = (2\,\mathrm{Im}(k_x))^{-1}$. This, together with the vertical confinement, leads to a mode that is strongly confined at the interface and propagates over a long distance.

2.3 Gratings

I begin by examining the theory underlying gratings. In an idealised grating, we consider that the light that hits the grating acts as a point source, according to Huygen's principle. The light leaving the grating at a particular position away from the grating is a superposition of all of these point sources. The path length from the point sources will depend on the geometry of the grating. A difference in path length will manifest itself as a difference in phase. This difference in phase will lead to varying constructive and destructive interference. There will be distinct points of maximum interference which occur at angles given by the Grating Equation (2.19), where θ_i is the angle of incidence, θ_m is the scattered angle of the grating mode, and m is an integer. These modes are labelled by the integer index m which is referred to as the 'order' of the mode.

$$\sin(\theta_m) = \sin(\theta) + \frac{m\lambda}{P} \tag{2.19}$$

If the grating is formed on a metal, the scattering of photons at the grating into the grating order modes provides momentum to the nearly free electrons of the metal of magnitude $k_g = \frac{2\pi}{P}m$, where k_g is a unit of additional momentum provided by the grating, P is the grating period, and m is the index labelling the mode, as before. The momentum k_g is equal to the magnitude of the reciprocal lattice vector of the grating. This additional momentum can provide the necessary coupling from the incident photon into a surface plasmon mode. The coupling condition is that the in-plane momentum $k_x = k_i \sin(\theta_i)$ matches between the incoming photon and the surface plasmon, as shown in Equation (2.20), where k_{sp} is the momentum of the surface plasmon, k_i is the momentum of the incident light, and θ_i is the angle of

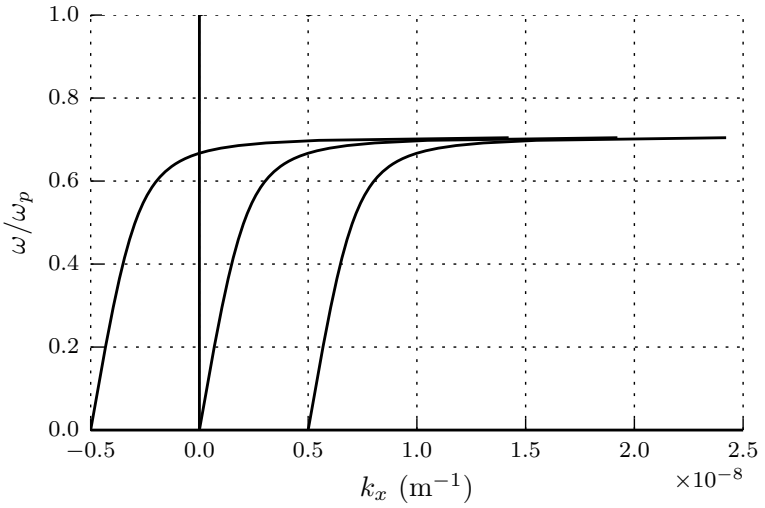

Figure 2.3 Surface plasmon dispersion for a Drude metal under the action of a grating, for $m = -1, 0, 1$.

incidence.

$$k_{sp} = k_i \sin(\theta_i) + mk_g \tag{2.20}$$

This grating coupling is illustrated in Figure 2.3 for an air/silver interface using a simple Drude model with a 350 nm grating within the silver. The surface plasmon dispersion equation has been used with the metal modelled using the simple Drude form, as before. Employing the planar interface equation for the surface plasmon is only strictly valid for the case of a shallow grating, which can therefore be treated as a small perturbation. The dispersion for SPPs travelling in the positive direction is plotted, including modes resulting from the addition of integer multiples of the grating vector with $m = -1, 0, 1$. Coupling to normally incident light with $k_x = 0$ is now possible.

2.4 Multilayer interference

I will now describe the theory underlying the interference of light passing through a layered structure. Let us first consider one layer in isolation, as shown in Figure 2.4.

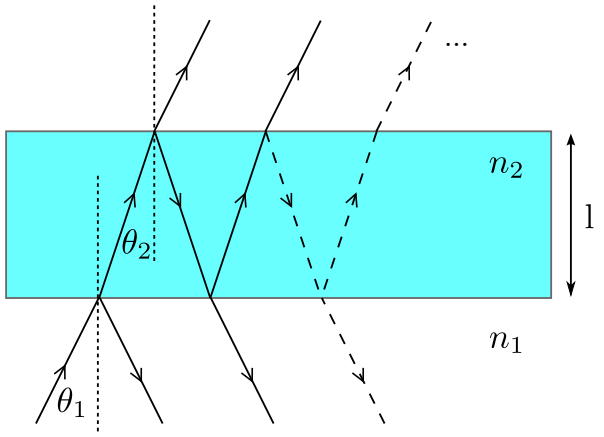

Figure 2.4 Schematic of interference within a single layer of a structure.

As light enters the layer, it is partially reflected and partially transmitted. The intensity of the reflected and transmitted components can be represented by reflection and transmission coefficients r and t. The magnitude of these coefficients can be calculated using the Fresnel equations. There may also be a phase change at the boundaries of the layer, which is also accounted for in the Fresnel equations, given in Equations (2.21), where the subscripts s and p denote the polarisations with the electric field perpendicular and parallel to the plane of incidence polarisation, respectively [80, 81].

$$r_s = \frac{n_1 \cos\theta_1 - n_2 \cos\theta_2}{n_1 \cos\theta_1 + n_2 \cos\theta_2} \tag{2.21a}$$

$$t_s = \frac{2n_1 \cos\theta_1}{n_1 \cos\theta_1 + n_2 \cos\theta_2} \tag{2.21b}$$

$$r_p = \frac{n_2 \cos\theta_1 - n_1 \cos\theta_2}{n_1 \cos\theta_2 + n_2 \cos\theta_1} \tag{2.21c}$$

$$t_p = \frac{2n_1 \cos\theta_1}{n_1 \cos\theta_2 + n_2 \cos\theta_1} \tag{2.21d}$$

In addition, as light travels through the layer, it accumulates a phase difference. The phase of the light at a position along its path is dictated by the distance it has travelled, the optical path length. The optical path length of a wave that has travelled a distance r in a medium with refractive index n is given by Equation (2.22). As the waves pass through different media, an optical path length accumulates as a sum of terms of that form.

$$d = nr \tag{2.22}$$

Two waves that were initially in phase will accumulate a phase difference ($\Delta\phi$) given by Equation (2.23), where d_i is the path length of each wave and λ is the wavelength of the waves:

$$\Delta\phi = 2\pi \frac{d_2 - d_1}{\lambda} \tag{2.23}$$

Returning to Figure 2.4, the light transmitted from the front of the layer reaches the rear where it again splits into a reflected a transmitted component. The reflected wave then reaches the front surface where it partially reflects. This reflection and splitting occurs recursively and leads to an infinite series of interfering waves inside and outside the layer. The overall superposition of these waves dictates the overall reflection and transmission from the layer.

In a complex multilayer structure, such as a solar cell, incident waves split into a reflected and transmitted component at each interface within the structure. This results in a complex interference pattern with light being distributed amongst the layers. The overall reflection and transmission is therefore a calculation involving a sum over an infinite number of reflections from each layer. This is a computationally difficult problem to solve. Alternatively, a transfer-matrix method (TMM) can be used in order to calculate this complex interference.

Within this method, the problem is simplified by employing the continuity conditions for the fields imposed by Maxwell's equations at each interface. Following the treatment in Heavens [82], at each interface forward and backward propagating waves are described on either side of the interface and written as vectors. Imposing the continuity of the fields at the interface leads to an interface matrix relating the fields on either side. This incorporates the Fresnel coefficients given above. In addition, there is a phase change and absorption as the field propagates through a layer, as discussed above, which is also included [83]. The propagation of the light through each intervening layer is therefore described by an overall matrix, known as a transfer matrix. The overall system matrix is solved by computing the product of these matrices. Finally, the reflection and transmission coefficients are derived from this overall system matrix. Alternatively, the Finite Difference Time Domain method, described below, allows explicit simulation of light propagating throughout complex structures in the time domain using Maxwell's equations.

2.5 Finite Difference Time Domain simulations

Finite Difference Time Domain (FDTD) is a method to simulate the propagation of electromagnetic radiation through a region. Within the method, Maxwell's equations are solved using a finite difference technique in the time domain. The complex refractive index is defined throughout the region, which is divided into mesh cells, in a method proposed by Yee [84]. Following this treatment, let us consider Maxwell's curl equations written in the following form:

$$\nabla \times \mathbf{E} = -\frac{\partial \mathbf{B}}{\partial t} \tag{2.24a}$$

$$\nabla \times \mathbf{H} = \mathbf{J_f} + \frac{\partial \mathbf{D}}{\partial t} \tag{2.24b}$$

Adopting a Cartesian co-ordinate system (x,y,z) we obtain the set of Equations (2.25) below, where it is assumed that there are no free currents within the region:

$$\frac{\partial \mathbf{B}_x}{\partial t} = \frac{\partial \mathbf{E}_y}{\partial z} - \frac{\partial \mathbf{E}_z}{\partial y} \tag{2.25a}$$

$$\frac{\partial \mathbf{B}_y}{\partial t} = \frac{\partial \mathbf{E}_z}{\partial x} - \frac{\partial \mathbf{E}_x}{\partial z} \tag{2.25b}$$

$$\frac{\partial \mathbf{B}_z}{\partial t} = \frac{\partial \mathbf{E}_x}{\partial y} - \frac{\partial \mathbf{E}_y}{\partial x} \tag{2.25c}$$

$$\frac{\partial \mathbf{D}_x}{\partial t} = \frac{\partial \mathbf{H}_y}{\partial z} - \frac{\partial \mathbf{H}_z}{\partial y} \tag{2.25d}$$

$$\frac{\partial \mathbf{D}_y}{\partial t} = \frac{\partial \mathbf{H}_z}{\partial x} - \frac{\partial \mathbf{H}_x}{\partial z} \tag{2.25e}$$

$$\frac{\partial \mathbf{D}_z}{\partial t} = \frac{\partial \mathbf{H}_x}{\partial y} - \frac{\partial \mathbf{H}_y}{\partial x} \tag{2.25f}$$

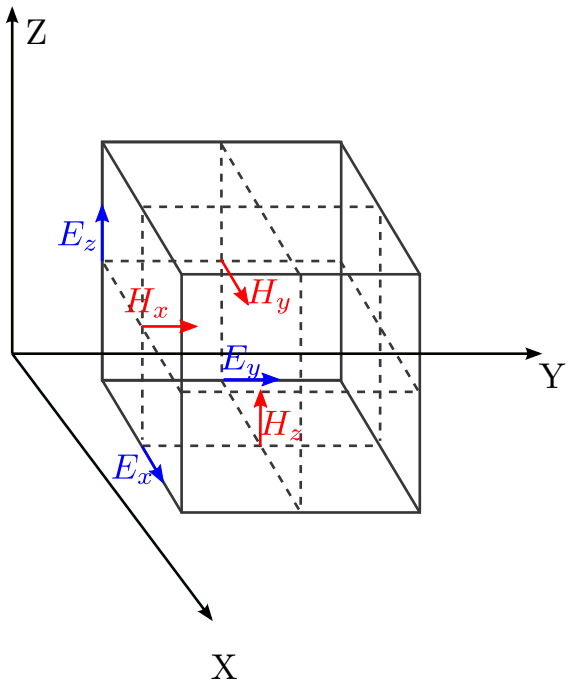

Figure 2.5 Schematic of the Yee cell meshing scheme.

The simulation region is broken up into discrete cuboidal 'Yee cells' which are labelled with integers i, j, and k. Any grid position can then be written as $(x, y, z) = (i\Delta x, j\Delta y, k\Delta z)$, where Δx, Δy and Δz are the size of the mesh steps used. The various components of the electric and magnetic fields are calculated at different positions within the Yee cell, such that the electric fields are calculated at the edges, whereas the magnetic fields are calculated perpendicular to the faces, as illustrated in Figure 2.5. Time is also discretised and labelled by an integer n, and any function of space and time is denoted by $F(i\Delta x, j\Delta y, k\Delta z, n\Delta t) = F^n_{i,j,k}$.

In order to solve numerically the Cartesian form of Maxwell's curl equations, given in (2.25), a central difference approach is taken to evaluate the spatial and time

derivatives as follows:

$$\left[\frac{\partial F}{\partial x}\right]_{j,k,n} = \frac{F^n_{i+\frac{1}{2},j,k} - F^n_{i-\frac{1}{2},j,k}}{\Delta x} + O((\Delta x)^2) \tag{2.26a}$$

$$\left[\frac{\partial F}{\partial y}\right]_{i,k,n} = \frac{F^n_{i,j+\frac{1}{2},k} - F^n_{i,j-\frac{1}{2},k}}{\Delta y} + O((\Delta y)^2) \tag{2.26b}$$

$$\left[\frac{\partial F}{\partial z}\right]_{i,j,n} = \frac{F^n_{i,j,k+\frac{1}{2}} - F^n_{i,j,k-\frac{1}{2}}}{\Delta z} + O((\Delta z)^2) \tag{2.26c}$$

$$\left[\frac{\partial F}{\partial t}\right]_{i,j,k} = \frac{F^{n+\frac{1}{2}}_{i,j,k} - F^{n-\frac{1}{2}}_{i,j,k}}{\Delta t} + O((\Delta t)^2) \tag{2.26d}$$

The second order and higher terms from the above Taylor series are then neglected but a good approximation is maintained if the spatial steps are sufficiently small. Due to the separation of the electric and magnetic field components on the Yee cell, it is possible to evaluate the central differences for the electric and magnetic field components in an alternating fashion, whilst stepping forward in increments of half a time-step $\frac{\Delta t}{2}$. The magnetic fields are calculated at odd multiples of the half-time step and the electric fields are calculated at even multiples. Applying the central differences equations of (2.26) to the Cartesian Maxwell's equations of (2.25) at the appropriate half-time steps, we obtain the following update equations which can be computed numerically:

$$B^{n+\frac{1}{2}}_{x_{i,j+\frac{1}{2},k+\frac{1}{2}}} = B^{n-\frac{1}{2}}_{x_{i,j+\frac{1}{2},k+\frac{1}{2}}} + \Delta t \left(\frac{E^n_{y_{i,j+\frac{1}{2},k+1}} - E^n_{y_{i,j+\frac{1}{2},k}}}{\Delta z} - \frac{E^n_{z_{i,j+1,k+\frac{1}{2}}} - E^n_{z_{i,j,k+\frac{1}{2}}}}{\Delta y} \right) \tag{2.27a}$$

$$B^{n+\frac{1}{2}}_{y_{i+\frac{1}{2},j,k+\frac{1}{2}}} = B^{n-\frac{1}{2}}_{y_{i+\frac{1}{2},j,k+\frac{1}{2}}} + \Delta t \left(\frac{E^n_{z_{i+1,j,k+\frac{1}{2}}} - E^n_{z_{i,j,k+\frac{1}{2}}}}{\Delta x} - \frac{E^n_{x_{i+\frac{1}{2},j,k+1}} - E^n_{x_{i+\frac{1}{2},j,k}}}{\Delta z} \right) \tag{2.27b}$$

$$B^{n+\frac{1}{2}}_{z_{i+\frac{1}{2},j+\frac{1}{2},k}} = B^{n-\frac{1}{2}}_{y_{i+\frac{1}{2},j+\frac{1}{2},k}} + \Delta t \left(\frac{E^n_{x_{i+\frac{1}{2},j+1,k}} - E^n_{x_{i+\frac{1}{2},j,k}}}{\Delta y} - \frac{E^n_{y_{i+1,j+\frac{1}{2},k}} - E^n_{y_{i,j+\frac{1}{2},k}}}{\Delta x} \right) \tag{2.27c}$$

$$D^{n+1}_{x_{i,j+\frac{1}{2},k+\frac{1}{2}}} = D^n_{x_{i,j+\frac{1}{2},k+\frac{1}{2}}} + \Delta t \left(\frac{H^{n+\frac{1}{2}}_{y_{i,j+\frac{1}{2},k+1}} - H^{n+\frac{1}{2}}_{y_{i,j+\frac{1}{2},k}}}{\Delta z} - \frac{H^{n+\frac{1}{2}}_{z_{i,j+1,k+\frac{1}{2}}} - H^n_{z_{i,j,k+\frac{1}{2}}}}{\Delta y} \right) \tag{2.27d}$$

$$D^{n+1}_{y_{i+\frac{1}{2},j,k+\frac{1}{2}}} = D^n_{y_{i+\frac{1}{2},j,k+\frac{1}{2}}} + \Delta t \left(\frac{H^{n+\frac{1}{2}}_{z_{i+1,j,k+\frac{1}{2}}} - H^{n+\frac{1}{2}}_{z_{i,j,k+\frac{1}{2}}}}{\Delta x} - \frac{H^{n+\frac{1}{2}}_{x_{i+\frac{1}{2},j,k+1}} - H^{n+\frac{1}{2}}_{x_{i+\frac{1}{2},j,k}}}{\Delta z} \right) \tag{2.27e}$$

$$D^{n+1}_{z_{i+\frac{1}{2},j+\frac{1}{2},k}} = D^n_{y_{i+\frac{1}{2},j+\frac{1}{2},k}} + \Delta t \left(\frac{H^{n+\frac{1}{2}}_{x_{i+\frac{1}{2},j+1,k}} - H^{n+\frac{1}{2}}_{x_{i+\frac{1}{2},j,k}}}{\Delta y} - \frac{H^{n+\frac{1}{2}}_{y_{i+1,j+\frac{1}{2},k}} - H^{n+\frac{1}{2}}_{y_{i,j+\frac{1}{2},k}}}{\Delta x} \right) \tag{2.27f}$$

Sources of electromagnetic radiation are defined within the simulation region by setting the initial field values. Equations (2.27a-c) and (2.27d-e) are then used alternately to calculate the magnetic and electric fields, respectively. In order to maintain numerical stability, the time step must be sufficiently small, in accordance with the Courant-Friedrichs-Levy stability criterion, Equation (2.28). This ensures that the field does not change significantly between time and spatial steps and is therefore dictated by the maximum speed of light propagation v_{max} within the simulation region. In addition, the spatial steps must be small, of order $\lambda/20$ for good numerical accuracy.

$$\Delta t \leq \left(v_{max} \sqrt{\frac{1}{x^2} + \frac{1}{y^2} + \frac{1}{z^2}} \right)^{-1} \tag{2.28}$$

The update equations (2.27) contain all four fields E, D, B, H and therefore (2.27a-c)

and (2.27d-f) cannot be directly calculated from one another. The relationships between them are contained within the constitutive equations, which in an isotropic medium are defined as follows:

$$\mathbf{D} = \epsilon(\omega)\mathbf{E} \tag{2.29a}$$

$$\mathbf{B} = \mu(\omega)\mathbf{H} \tag{2.29b}$$

where ϵ is the electrical permittivity, which is in general complex, and μ is the magnetic permeability, which is often equal to μ_0 in non-magnetic media. The following discussion will therefore focus only on the permittivity. As the permittivity is frequency dependent, but the update equations are defined in the time domain, the constitutive equations cannot be directly applied. In the time domain Equation (2.29a) takes the form of a convolution:

$$\mathbf{D}(t) = \epsilon(t) \otimes \mathbf{E}(t) \tag{2.30a}$$

This is a resource-intensive calculation and instead the permittivity is represented as an analytical function of ω. A Fourier transform can be performed on this analytical function in order to represent it in the time domain. In practice, the components of D are calculated using the update equations (2.27d-f), and then the transformed analytical function is used to calculate E which can then be used in (2.27a-c). A variety of forms of the analytical functions can be trialled in order to obtain the best fit to any experimental data available over the wavelengths of interest.

Since the simulation region is finite to make computations feasible, we need to consider what happens to light when it reaches the boundary of the simulation region. Boundary conditions are therefore applied to the fields, with appropriate properties for the simulations in question. Common boundary conditions include Perfectly Matched Layers (PML) which are designed such that light incident at the boundary is absorbed with as few reflections as possible. They are not, however, perfect and some reflections will occur. They are most effective when the incoming light is at normal incidence and become increasingly ineffective at steep angles of incidence. Other boundary conditions include symmetric and anti-symmetric conditions which impose conditions on the continuity of the electric and magnetic field vectors at the boundary. There are also Bloch and metallic boundary conditions, amongst others, which will be described as required later in this work.

Having obtained numerical values for the magnitude of the electric and magnetic field components at all grid positions in the simulation region as a function of time, a Fourier Transform of the data from $t \rightarrow \omega$ can be performed in order to obtain information on the fields as a function of frequency ($E(\omega)$ and $H(\omega)$). As the simulation has a finite length, it is effectively multiplied by a rectangular window in the time domain, and the Fourier transform will therefore contain a convolution with a sinc function in the frequency domain. It is therefore important to run the simulation for long enough that the time-domain field intensities are very low at the end of the simulation. It is also possible to use alternative windowing functions to improve aspects of the frequency-domain data according to requirements.

The resulting data from the Fourier transform is complex and the real and imaginary components have important meanings. Representing the data in modulus-argument form $A\exp(i\phi)$ at each wavelength, the modulus represents the time-averaged field throughout the simulation. The square of this gives the average field intensity. The

phase of the signal gives information on the time evolution of the signal. In order to isolate the field at a particular time, the real component of the complex field is taken for a particular phase value. By multiplying by an additional phase factor $\exp(i2\pi\Delta\phi)$ $(0 < \Delta\phi < 2\pi)$ prior to taking the real component, the fields at any point in the optical cycle for a particular wavelength can be computed. This is due to the property of Fourier transforms such that the Fourier transform of a function multiplied by the above phase factor in the frequency domain is equivalent to a convolution with a delta function $\delta(t - \phi)$ in the time domain.

2.6 Chapter summary

In this chapter, I have provided a broad overview of several important principles that govern the enhancement of thin film solar cells using gratings. The principles of plasmonics are of great importance as plasmonic modes can be excited when nano-scaled features are included in a structure. The influence of gratings on surface plasmon phenomena has also been described. The theory of multilayer interference, which arises due to the thin films present in organic solar cell devices, has been presented. Finally, an overview was provided of the FDTD technique, which plays a strong role in the remainder of this work.

CHAPTER 3

Basic cell modelling and grating enhancement mechanisms

3.1 Introduction

In this chapter, I present simulations of organic solar cells based on P3HT:PCBM using the FDTD technique outlined in Section 2.5. The FDTD method, a time-domain technique, is selected over finite element modelling techniques as it allows a broadband response to be computed from a single simulation. This is of particular benefit due to the large number of broadband simulations required in this work. In addition, it enables an intuitive visualisation of the propagation of light through the system, mirroring a practical experiment. The chapter opens with a discussion of the

general simulation method, followed by a description of the principal calculations used to process the simulation data. These general methods also underpin the simulations performed in Chapter 4. The first results in Section 3.4 detail investigations of planar solar cell devices, including an investigation of the effect of layer geometry on the efficacy of these planar devices. The results provide an important benchmark from which to investigate enhanced devices. Results of simulations of devices incorporating gratings then follow in Section 3.5, along with a detailed investigation into the sources of the enhancements and suppressions that arise. I then move on to quantify the relative importance of the sources of enhancement in Section 3.6 and provide new insight into the design of thin film organic solar cells incorporating grating structures.

3.2 General simulation methodology

A commercial Finite Difference Time Domain (FDTD) software package (Lumerical Solutions [85]) was used to simulate the propagation of light through thin-film organic solar cells. The electric fields present within the photoactive region of the cell were recorded, along with the refractive index at each spatial location as a function of wavelength. From these data it was possible to calculate the fraction of light absorbed within the active region of these solar cells. Refractive index data for the P3HT:PCBM active region, the transparent ITO contact, and the PEDOT:PSS hole transport layer were taken from Monestier *et al.* [86] and Tumbleston *et al.* [87]. These data are obtained by ellipsometric measurement and are used frequently in the literature for modelling purposes. The same data are used in works with which I make direct comparison [1, 2]. The data for the metals used in the contacts was taken from Palik [88]. This work is also considered as a standard reference for these materials.

Anti-symmetric boundary conditions were applied at the edge and in the middle of the simulation region. This simulates an infinite periodic structure but reduces the computational requirement by half compared to simulations in which periodic boundary conditions are applied at the lateral boundaries. Absorbing PML boundary conditions, as described in Section 2.5, are employed at the top and bottom of the simulation region, so that any light reflected from or transmitted through the cell is lost. The device is illuminated at normal incidence using a uniform intensity broadband plane wave source with wavelengths in the range 300 nm to 900 nm covering the full range of wavelengths in which the active region can absorb incident light. The incident radiation is polarised with the electric field displacement in the plane of the simulation (TM polarisation) unless otherwise stated, as this is the predominant polarisation that can excite surface plasmon modes in the featured device. A schematic of the TM and TE polarisations, relative to a typical grating, is shown in Figure 3.1.

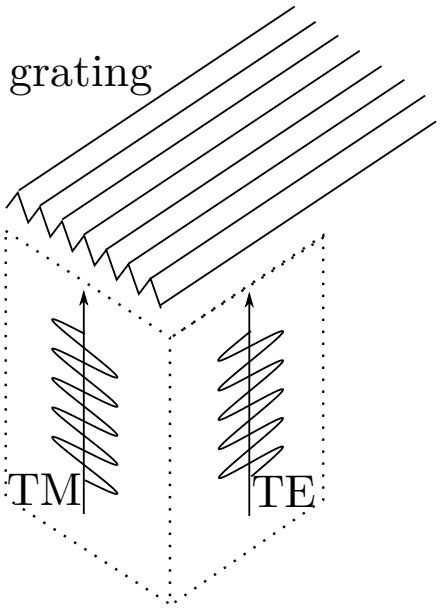

Figure 3.1 Schematic illustrating the definition of TM and TE polarisations of incident light relative to a grating.

Light is assumed to be incident from within a glass interface, which is a common substrate used for these devices. The simulations therefore ignores any reflections from the air/glass interface. This has the benefit that it greatly reduces unnecessary simulation overhead as the thick glass substrate does not need to be simulated. This would otherwise greatly increase the computational demands as it is many times thicker than the active photovoltaic device. The effects of a simple glass/air interface are well understood and can be added as a post-simulation step by calculation using the Fresnel equations discussed in Section 2.4.

A proprietary conformal mesh technology [85] was employed in order to improve accuracy at larger mesh sizes and therefore allow faster convergence with respect to mesh size. This technology is based upon altering the update equations for the magnetic component of the field in order to perform a contour integral over the cell that accounts for the boundary between dielectric materials within it. The principles of this technique are demonstrated for perfect electric conductors by Mittra & Yu [89].

Simulations were performed on a custom-built workstation with a 6 (12 virtual) core i7-3930K processor, 62GB RAM, and a fast solid state hard drive (SSD). The simulations were run in parallel across the cores. This hardware combination allowed a high volume of simulations to be run in a relatively short time. This permits relatively large parameter sweeps of device parameters to be performed.

3.3 Calculations

An absorption metric $A(\lambda)$ is defined as the fraction of energy absorbed in the active layer as a function of wavelength. This can be calculated by integrating the

divergence of the Poynting vector over the photoactive region as follows:

$$A(\lambda) = -0.5 \int \text{real}(\nabla \cdot \mathbf{P})\text{dV} \tag{3.1}$$

where λ is the wavelength of incident light and $\mathbf{P}$ is the Poynting vector. This can be computed with higher numerical accuracy by rewriting as follows, in the case of non-magnetic materials:

$$\begin{aligned} A(\lambda) &= 0.5 \int i\omega \mathbf{E}(\lambda) \cdot \mathbf{D}\text{dV} \\ &= -0.5 \int \omega\lambda |\mathbf{E}|^2(\lambda)\, \text{Im}(\epsilon)\text{dV} \\ &= -0.5 \int \frac{2\pi c}{\lambda} |\mathbf{E}|^2(\lambda)\, \text{Im}(\epsilon)\text{dV} \end{aligned}$$

where λ is the wavelength of incident light, E is the electric field normalised at each wavelength to the incident field on the device, and ϵ is the permittivity of the active layer. The integral is performed solely over the active layer, therefore excluding absorption within the metal and PEDOT:PSS layers which would not contribute to photocurrent in a real device. In order to achieve this, I exclude all mesh cells which contain metal by examining the imaginary component of their refractive index.

$A(\lambda)$ provides useful information on the spectral distribution of energy absorption within the active layer. It is possible to calculate the total absorbed energy in the wavelength range of interest bounded by λ_{min} and λ_{max} from $A(\lambda)$ by integrating across these wavelengths as shown in Equation (3.2). The values of λ_{min} and λ_{max} are set to the limits of the absorption within the photoactive material, so 300 nm

and 900 nm, respectively, for devices based on P3HT:PCBM.

$$A_{tot,E} = \int_{\lambda_{min}}^{\lambda_{max}} A(\lambda)\mathrm{d}\lambda \tag{3.2}$$

Equation (3.2) is a metric that is sometimes reported in the literature but doesn't fully reflect the useful absorption within a device. This is because the current generated by the device is related not to the energy absorbed, but to the number of photons absorbed. Conversion between the two can be achieved by dividing by the energy of a photon at each wavelength $E_{photon}(\lambda) = \frac{hc}{\lambda}$. The standard incident spectrum used in the solar cell community is AM1.5G. This is calculated assuming an air mass of 1.5, corresponding to 1.5 atmosphere thickness, and includes both direct and diffuse components of the incident light. By contrast, an AM1.5D spectrum only includes the direct component of the incident light. Figure 3.2 illustrates the incident energy and photons present in AM1.5G light in terms of energy and photons. These are sometimes referred to as the spectral irradiance and spectral photon flux density, respectively. The longer wavelengths appear more heavily weighted due to the lower energy of photons at these wavelengths. This is a more useful metric as solar cells produce at most one exciton, and thus electron per incident photon [90]. The efficiency of converting absorbed photons into electrons is defined through the internal quantum efficiency (IQE).

A total absorption metric $A_{tot}(\lambda)$ is defined which describes the total photons absorbed over the incident wavelength range as follows:

$$A_{tot} = \int_{\lambda_{min}}^{\lambda_{max}} \frac{hc}{\lambda} A(\lambda)\mathrm{d}\lambda \tag{3.3}$$

As a useful figure of merit, I finally introduce an *absorption current density* J_{abs}, as

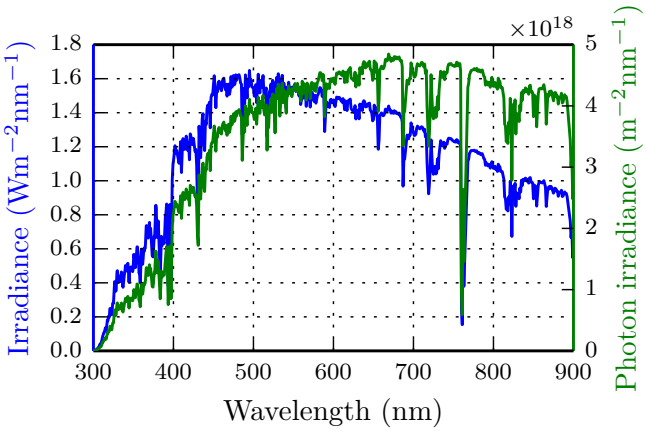

Figure 3.2 Incident AM1.5G light in units of energy and photons.

the maximum rate at which photoexcited charge could be generated per unit area of the device under AM1.5G solar illumination:

$$J_{abs} = q_e \int \frac{\lambda}{hc} P_{AM1.5G}(\lambda) A(\lambda) \mathrm{d}\lambda \tag{3.4}$$

where q_e is the electron charge, and $P_{AM1.5G}(\lambda)$ is the AM1.5G spectral power density.

A perfect IQE of 1 is assumed in the above equation, so that every absorbed photon leads to a captured electron. Whilst perfect extraction is unlikely, P3HT:PCBM devices have been demonstrated with high IQEs of over 0.85 [91] and approaching 1 for alternative polymer blends [92]. The parameter J_{abs} is my principal figure of merit as it provides an approximation to the maximum photocurrent J that the device could generate. It is an absolute figure that enables fair comparison between different device geometries.

3.4 Planar devices

3.4.1 FDTD simulations

It is instructive to first examine the refractive index data used as an input to the simulations. A fit is applied to the sampled data and the quality of this fit has a marked influence on the accuracy of the results obtained. For all of the materials used, the fitted functions show extremely good agreement with the sampled data across the whole spectrum. The final functions used in the simulations throughout this thesis are shown in Figure 3.3, where the sampled data has been omitted as it falls so close to the fitted lines.

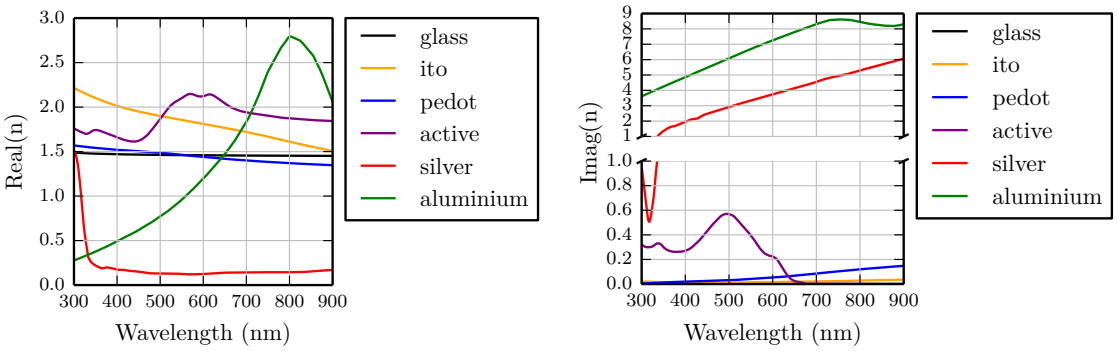

(a) Re(n) (b) Im(n)

Figure 3.3 Refractive index data (n) for the layers used in the simulations. The data are taken from various sources [86–88].

Simple control devices were first simulated with planar electrodes, as shown in Figure 3.4. 2D simulations were performed to reduce the computational time and give an excellent approximation to 3D devices in this simple planar case. The absorption spectrum within the active layer of such a typical device is shown in Figure 3.5.

The polymer absorbs strongly at the shorter wavelengths, with a steep decline around

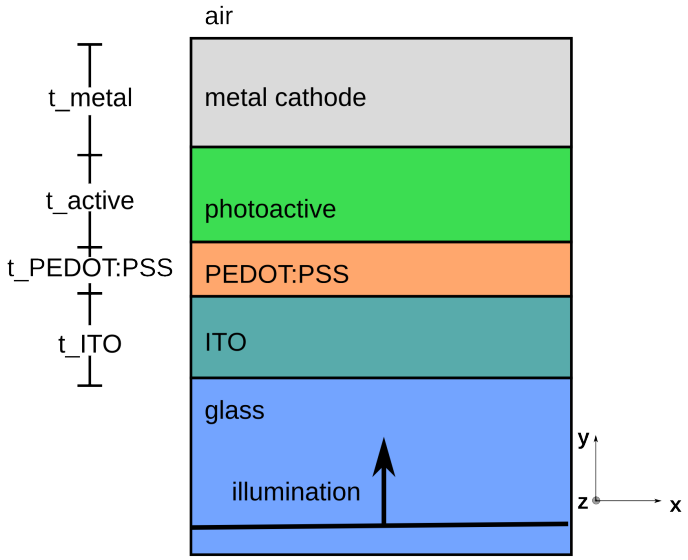

Figure 3.4 Simulation geometry for simple planar control devices

600 nm. This is to be expected from the imaginary components of the refraction index of the active region, shown in Figure 3.3b. Whilst it would be beneficial to boost absorption in all areas of the spectrum, there is a particular deficit at longer wavelengths. This shortfall can be addressed somewhat through the introduction of plasmonic structures at the electrode.

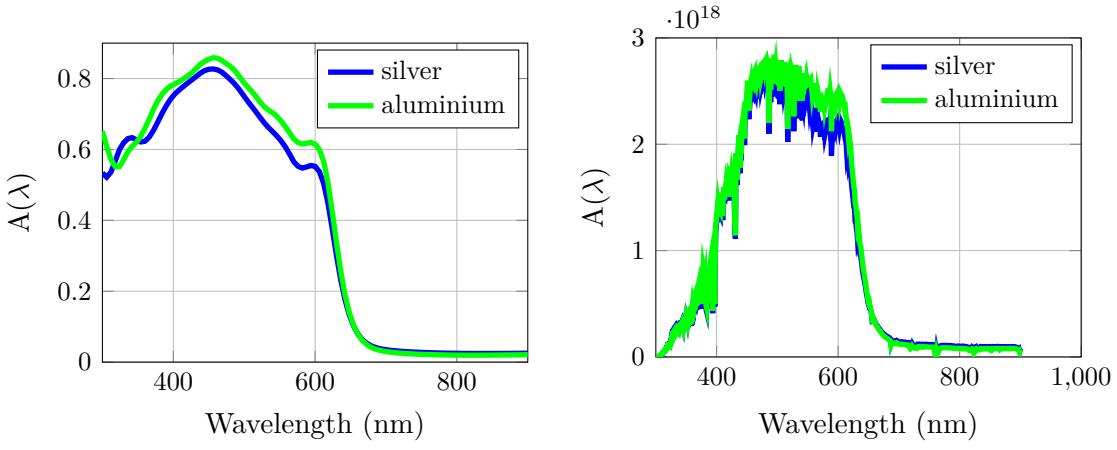

(a) Fraction of absorbed energy under uniform illumination

(b) Photons absorbed under AM1.5 light

Figure 3.5 Typical absorption spectrum for a control device with active layer thickness 100 nm.

Previous work suggests that the thickness of the layers within the device has a marked influence on overall device performance. Moulé *et al.* (2006), for example, note the effect of altering the active layer thickness on device performance [93]. This provided the motivation for a parameter sweep of the control devices, varying the active layer and ITO thicknesses at a constant PEDOT:PSS thickness of 50 nm, and the active layer and PEDOT:PSS thicknesses at a constant ITO thickness of 100 nm. False colourscale plots of J_{abs} as a function of the layer thicknesses for silver and for aluminium electrodes are shown in Figure 3.6.

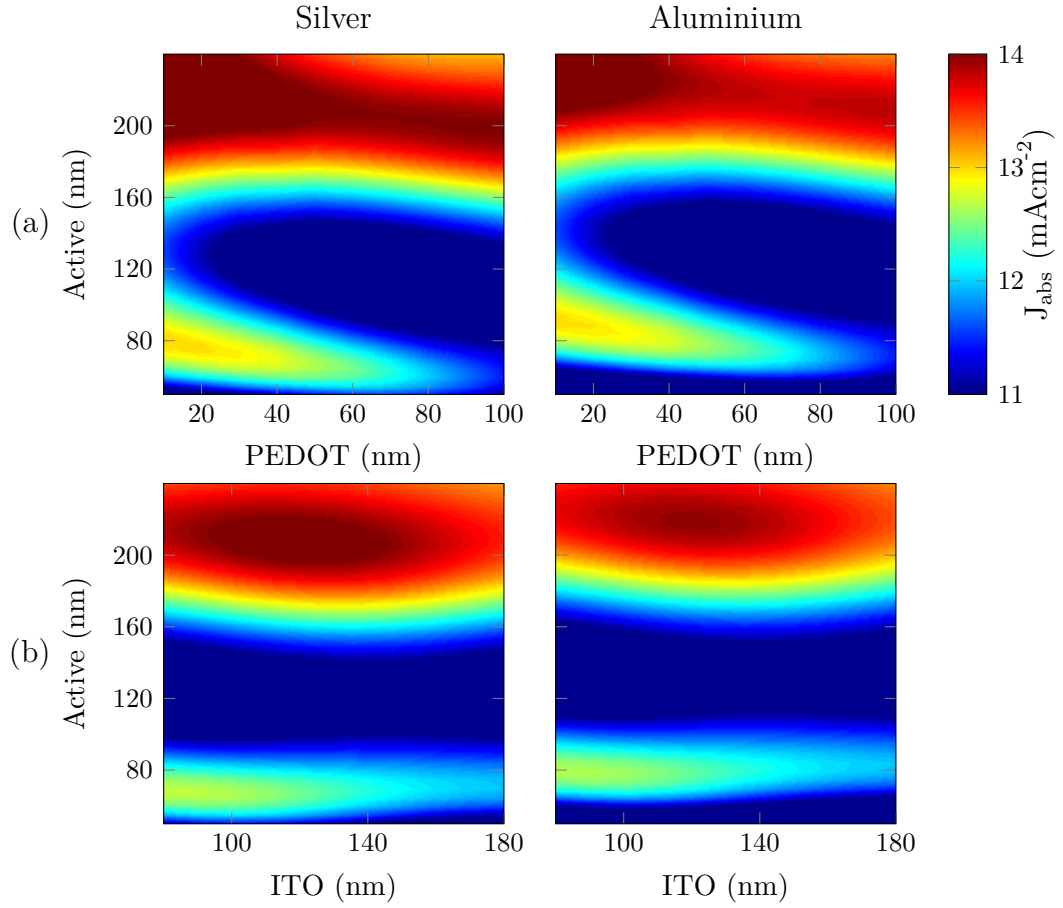

Figure 3.6 Absorption current density J_{abs} as a function of layer thicknesses, simulated using an FDTD method, as follows: (a) active layer against PEDOT:PSS with a fixed 100 nm ITO layer (b) active layer against ITO with a fixed 50 nm PEDOT:PSS layer. Results are shown for silver (left) and aluminium (right) electrodes.

These results confirm that varying the layer thicknesses strongly influences the photon absorption within the active region. As the PEDOT:PSS thickness is increased,

absorption within the active layer decreases. The optimum active layer thickness is a function of the PEDOT:PSS thickness, with an increase in thickness of the PEDOT:PSS layer necessitating a thinner active layer. This strongly supports the theory that the differences are due, in part, to interference at the various layers within the multilayer stack. This interference leads to an increasing fraction of the confined field occurring within the PEDOT:PSS. In addition, as the path length through the PEDOT:PSS increases, so too does the absorption. This absorption takes place at longer wavelengths, as seen in Im(n) from Figure 3.3b, and may therefore be particularly detrimental to these devices, as absorption is already low in this spectral region. Ideally, no PEDOT:PSS layer should therefore be employed, but in practice it is essential due to the benefits it creates for charge extraction, as discussed in Section 1.3. In addition, in practice there is a minimum thickness for this layer in order to achieve a complete conformal layer using conventional solution processed deposition techniques. This typically falls around 50 nm.

The overall result of the interference and absorption is that there are two absorption maxima which occur for a silver electrode at active layer thicknesses of 80 nm and 210 nm, providing absorption currents J_{abs} of 13.0 mA/cm^2 and 14.6 mA/cm^2 respectively, with these values decreasing slightly as the PEDOT:PSS thickness is increased. This corresponds to an absorption of 39% and 42% of the incident photons, respectively, in the range 300 nm to 900 nm. It is worth noting, however, that this result is highly sensitive to the layer thicknesses. For an aluminium electrode the results are broadly similar, but the optimal thicknesses for the active layers are about 10 nm greater than for the silver electrode.

Altering the ITO layer thickness also has a strong influence on absorption. As the thickness of this layer is increased at a constant PEDOT:PSS thickness of 50 nm, the absorption current within the active region also decreases due to increased absorption

within the ITO as the path length through it increases. The absorption within the ITO increases with wavelength, following the increase in Im(n) in Figure 3.3b, and therefore has a particularly detrimental effect on overall current density in organic devices. There is a smaller correlation between the ITO thickness and the optimal active layer thickness, in contrast to the case when altering the PEDOT:PSS thickness. This difference may be due to the strongly wavelength-dependent real component of the refractive index of the ITO, which decreases from 2.2 at 300 nm to 1.5 at 900 nm, shown in Figure 3.3a. This change in refractive index will obscure the effects of the multilayer interference as each wavelength will have a different spatial profile of the confined field as a function of layer thickness. In general, therefore, increasing the ITO thickness reduces absorption within the active layer and it is preferable to use an ITO layer which is as thin as possible. This must be balanced, however, against the beneficial charge extraction properties of the ITO layer, as the ITO conductivity is proportional to the layer thickness [94].

These results strongly support those that have been previously demonstrated. Min Nam *et al.* (2010) use a transfer matrix method to simulate the exciton generation within a cell [95]. This method enables rapid simulations to be performed of planar devices. They demonstrate interference peaks at very similar values for the active layer thickness to those reported here. In addition, they identify a dependence on the thickness of the PEDOT:PSS layer. Similarly, Moulé & Meerholz [96] have previously noted the dependence on both ITO and PEDOT:PSS thickness for a more limited range of active layer thicknesses [96]. The results demonstrated from the FDTD method therefore show good agreement with this previous work. Using the FDTD method, more complex electrode structures can now be simulated, breaking away from the planar device to which the transfer matrix method is best suited.

The key result emerging from the above discussion is that absorption maxima

occur when the multilayer interference leads to a maximum field within the active region. The active layer thickness for which this occurs shows a dependence on both PEDOT:PSS and ITO thickness, but these are typically constrained by other factors in practical devices. In the case of the PEDOT:PSS, the layer should also be as thin as possible, but there is in practice a minimum thickness required to provide the beneficial electronic properties. In the case of ITO, it should also be as thin as possible, but a minimum thickness is required in order to permit adequate conductivity. I now pick an ITO thickness of 100 nm and a PEDOT:PSS thickness of 50 nm, which are typical dimensions found in working devices [97]. Taking these dimensions, there are two absorption maxima evident at active layer thicknesses of around 80 nm and 210 nm. The lower maximum provides benefits in terms of a shorter distance for charge extraction and also in terms of ease of fabrication. The results for the remainder of this work will therefore focus on devices in the lower thickness regime. The results so far presented for planar devices now provide a baseline for the study of the effect of structured electrodes on optical absorption.

3.4.2 Transfer Matrix Modelling

To provide some verification of the FDTD models, the same simulations were performed using a transfer matrix approach. This was accomplished using an open source Python package [98]. The same data was used for the permitivities of the materials as was used for the FDTD simulations. The results of the TMM simulations are shown in Figure 3.7 and can be compared directly with the FDTD results shown in Figure 3.6. It can be seen that these two simulation methods show strong agreement. This provides some corroboration of the FDTD simulation results and gives confidence in the validity of the results before moving forwards with more advanced simulations.

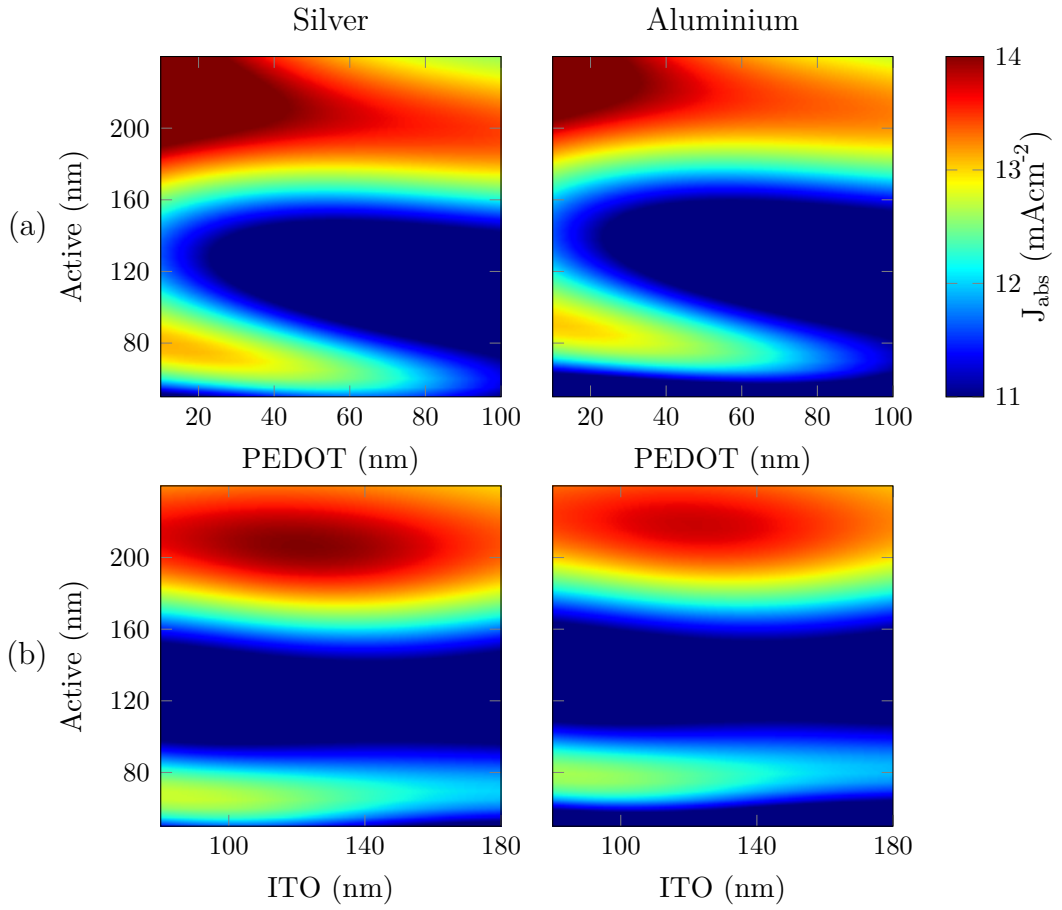

Figure 3.7 Absorption current density J_{abs} as a function of layer thicknesses, simulated using a TMM method, as follows: (a) active layer against PEDOT:PSS with a fixed 100 nm ITO layer (b) active layer against ITO with a fixed 50 nm PEDOT:PSS layer. Results are shown for silver (left) and aluminium (right) electrodes.

3.5 Plasmonic devices

In this section, a 1D grating is introduced at the rear metallic electrode. This provides additional in-plane momentum k_x which allows coupling into surface plasmon modes, as discussed in Section 1.4. Initially, a simple grating geometry of a periodic array of triangles is investigated, as shown in Figure 3.8. This design is motivated by the potential fabrication routes that could be employed in real devices. The grating geometry is described by its periodicity (P), height (H) and fill factor (FF), defined as the quotient of the feature width (W) and periodicity: FF = W/P. Abutting triangles are simulated, such that the fill factor is equal to 1. The device is illuminated with normally-incident uniform light and anti-symmetric boundary conditions were applied as in the planar devices.

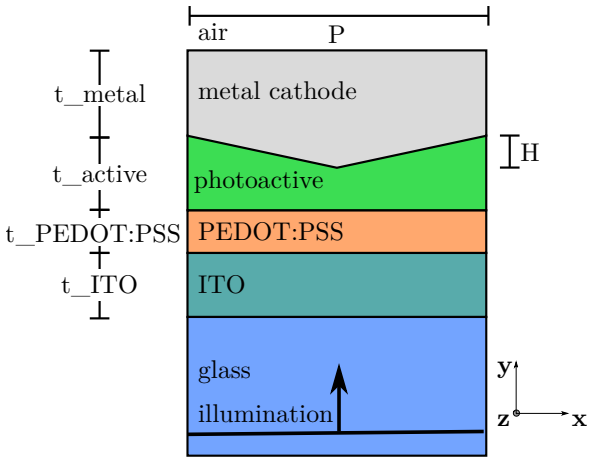

Figure 3.8 Schematic of the triangular grating geometry.

A typical absorption spectrum $A(\lambda)$ for a device incorporating a 400 nm grating with height 60 nm is shown in Figure 3.9. These plots show the fraction of incident photons absorbed at each wavelength. These gratings dimensions are chosen as they provide clearly identifiable features in the spectrum. There is a large broadband increase in absorption, along with a peak at around 780 nm and 710 nm for silver

and aluminium, respectively. This peak is provisionally attributed to the excitation of a surface plasmon mode, which has a longer path length through the active layer and therefore leads to increased absorption there. The position of this resonance can be altered by varying the grating period.

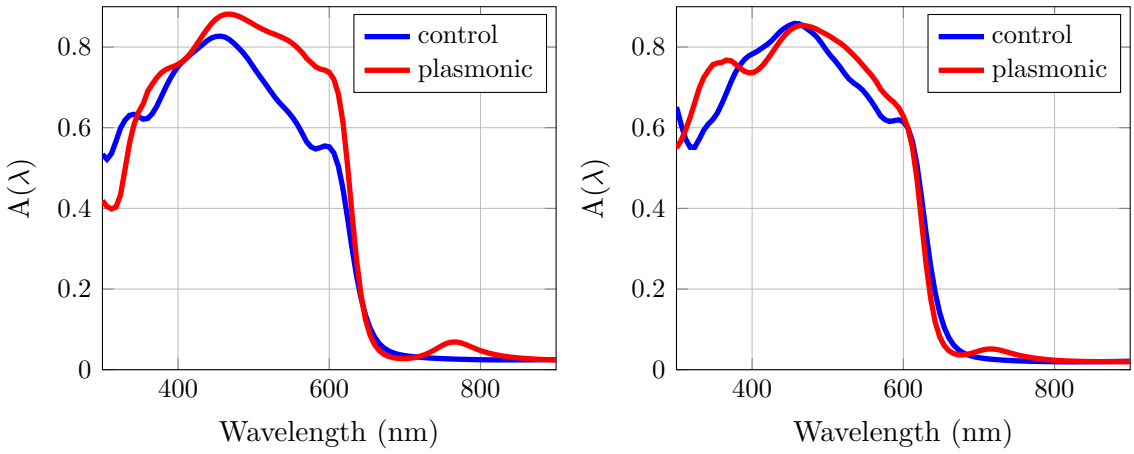

(a) Silver

(b) Aluminium

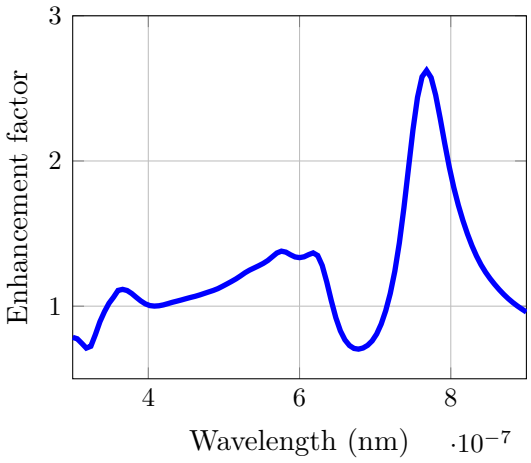

(c) Silver

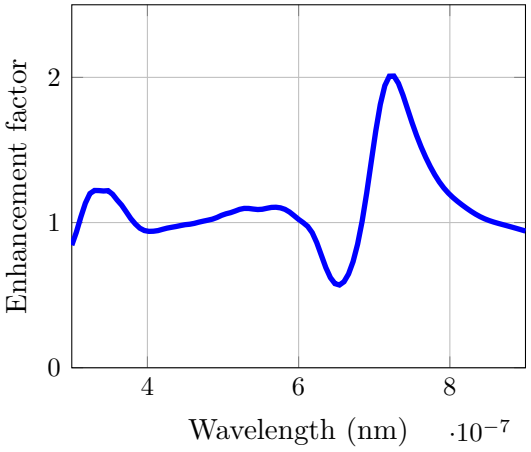

(d) Aluminium

Figure 3.9 Typical absorption spectra $A(\lambda)$ within the active layer for a device incorporating a 400 nm period grating with active layer thickness 100 nm for both silver and aluminium electrodes (a,b). The control spectrum is shown for reference. The relative enhancement of the planar compared to the control devices (c,d).

To assess the impact of the grating more clearly, the relative increase in absorption is plotted as a function of wavelength alongside the absorption spectra in Figure 3.9. From this figure, several-fold enhancement at the surface plasmon peak can be identified. There is also a broadband enhancement from around 450 nm to 600 nm.

There are dips in the spectrum at short wavelengths, around 320 nm for silver and even shorter for aluminium, and a strong dip below unity at wavelengths just short of the surface plasmon peak for both metals. The mechanisms leading to these enhancements and suppressions will be examined in Section 3.6.

These spectra are useful to assess the relative enhancements of the devices, but assume a uniform incident light source. In order to assess the typical performance of the device under sunlight, it is necessary to multiply $A(\lambda)$ by the standard AM1.5G solar photon flux irradiance, having first interpolated to the FDTD simulation wavelengths. The result is shown in Figure 3.10.

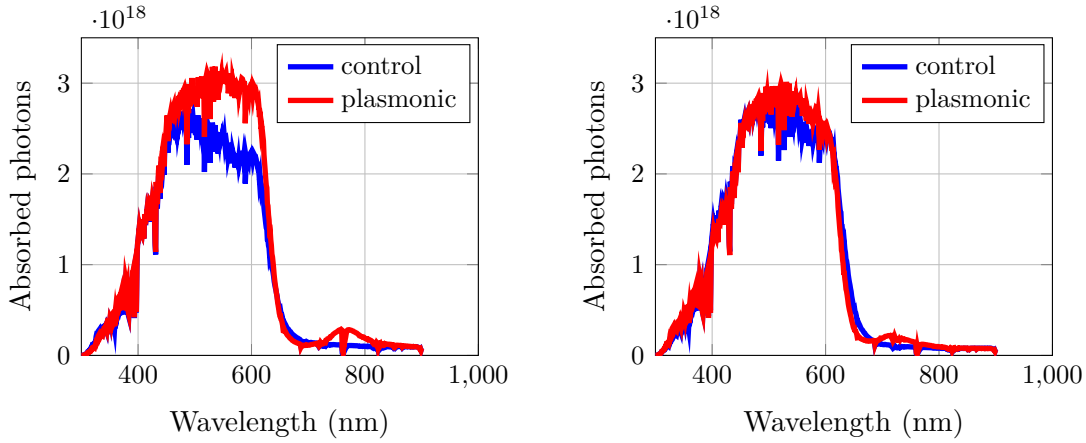

(a) Silver (b) Aluminium

Figure 3.10 Typical photon absorption spectrum within the active layer for a device incorporating a 400 nm period grating with active layer thickness 100 nm under AM1.5G solar irradiation for both silver and aluminium electrodes.

The total number of absorbed photons at the surface plasmon peak is relatively small compared to the main absorption peak, but the simulated device has not been optimised at this stage. The broad enhancement from 400 nm to 600 nm is again evident in these photon absorption spectra. The detriments at short wavelengths are now masked due to the relatively small number of incident photons present in the incident AM1.5 spectrum at these wavelengths. Now that the enhanced regions of the spectrum have been identified, albeit with suppression in other areas, it is now

of great interest to identify the origins of these enhancements.

3.6 Mechanisms of enhancement

The spectral modifications identified due to the incorporation of the grating were highly dependent on the periodicity of this grating. As a result, a series of simulations were run whilst sweeping the period of the grating at a fixed grating height of 60 nm and a fill factor of 1. The light absorbed, as a function of grating period, is shown in Figure 3.16. Both the absolute fraction of light absorbed (3.16a), and also the relative change compared to a planar cell with the same initial active layer thickness (3.16b) are shown.

For both grating geometries, there is a periodicity-dependent absorption peak which extends from 600 nm up to higher wavelengths. This feature occurs at slightly shorter wavelengths for the aluminium compared to the silver electrode. This is the peak that has so far been attributed to the surface plasmon mode, which exists due to the periodicity of the grating. This mode propagates along the metal/active interface, and therefore has a long path length through the active region where it can be absorbed. This leads to the increase in absorption observed.

The surface plasmon resonance is dependent on the periodicity of the grating, as this dictates the additional momentum provided as discussed in Section 2.3, and this is borne out in the absorption feature observed. To further confirm that this is indeed a surface plasmon mode, a simulation sweep under TE polarisation was performed. It is not possible to excite surface plasmon modes when the electric field is orientated parallel to the grating and the mode should therefore not be evident under TE polarisation. A plot of $A(\lambda)$ and the change in $A(\lambda)$ for TE polarisation is

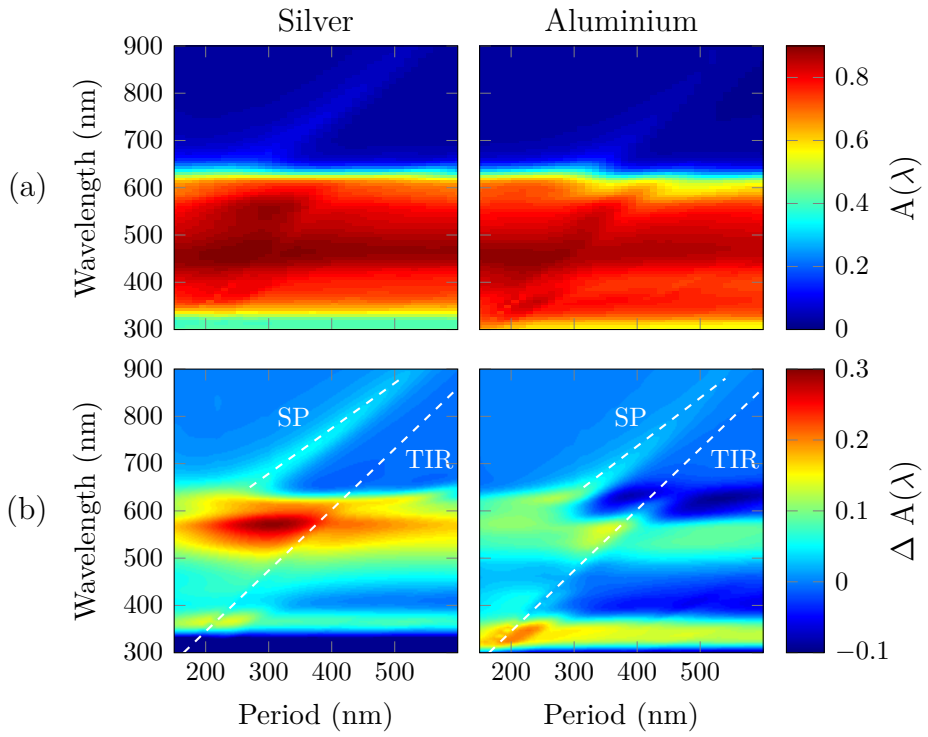

Figure 3.11 Plot of $A(\lambda)$, the fraction of incident photons absorbed by the active layer (a), and the absolute increase of A(λ), $\Delta A(\lambda)$, compared to a planar device (b), for a cell with active layer thickness 100 nm incorporating a triangular grating with height 60 nm, with a silver (left column) and aluminium (right column) electrode under TM illumination. The surface plasmon mode (SP) and total internal reflection cutoff (TIR) are labelled with dashed lines as a guide for the eye.

given in Figure 3.12. The mode is indeed absent in this plot, giving further evidence that the feature is due to a surface plasmon mode.

Finally, the surface plasmon mode can be directly observed by inspecting the spatial absorption profile within the active layer. To achieve these plots, simulations of full devices were performed, as before, but now $A(\lambda)$ is plotted as a function of position, for a specific wavelength. In effect, this gives the average field distribution over the course of one optical cycle at the given wavelength. Figure 3.13 demonstrates the spatial absorption profile of the first order surface plasmon mode for a triangular grating with a periodicity of 350 nm. The electric field is strongly confined near the electrode interface, as expected from a surface plasmon mode. The field decays into the photoactive material and leads to a strong enhancement there. By taking the

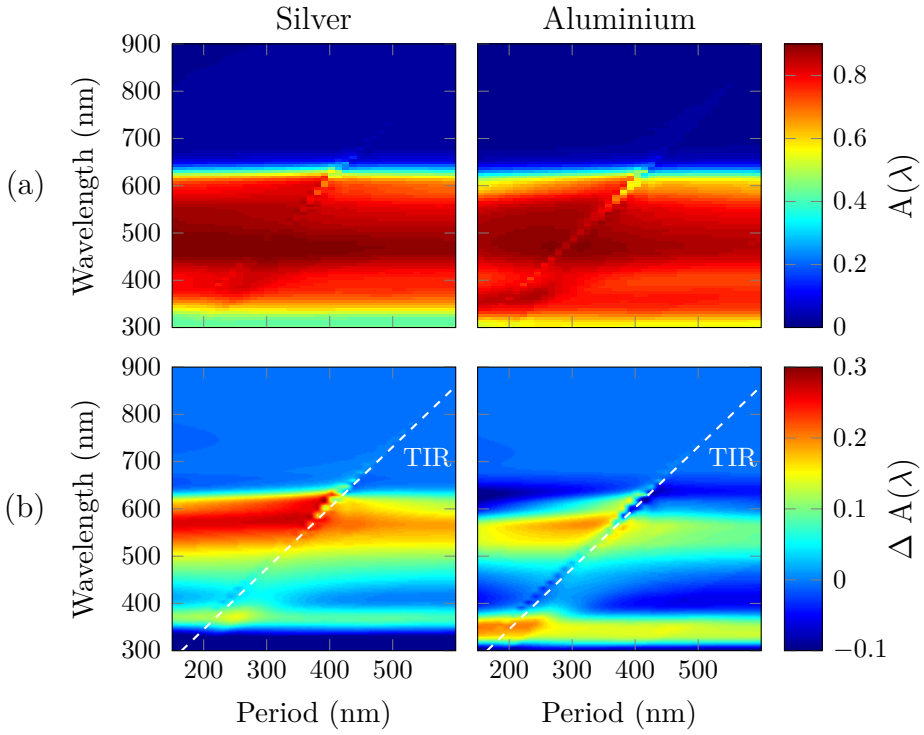

Figure 3.12 Plot of $A(\lambda)$ (a) and $\Delta A(\lambda)$ (b) as a function of grating period, under TE polarisation. The surface plasmon mode (SP) and total internal reflection cutoff (TIR) are labelled with dashed lines as a guide for the eye.

real component of the electric field having multiplied by a phase factor $\exp(i2\pi\Delta\phi)$ $(0 < \phi < 2\pi)$, as described in Section 2.5, the time evolution of the field over the course of an optical cycle was calculated at the surface plasmon wavelength. A typical set of images for E_y at various stages within the optical cycle is shown in Figure 3.14. This takes the form of a surface plasmon mode, as expected.

Returning to Figure 3.16, there is a broad enhancement in absorption evident around

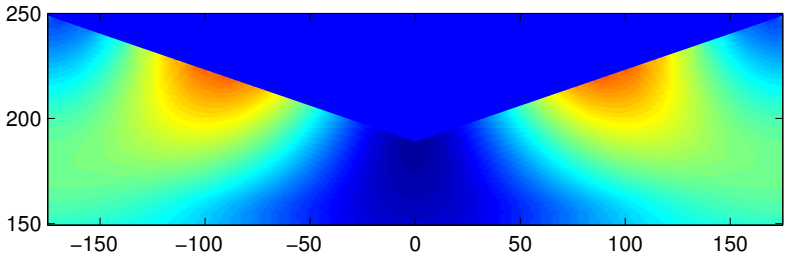

Figure 3.13 Electric field map intensity of the first order surface plasmon mode within the active region at a wavelength of 670 nm.

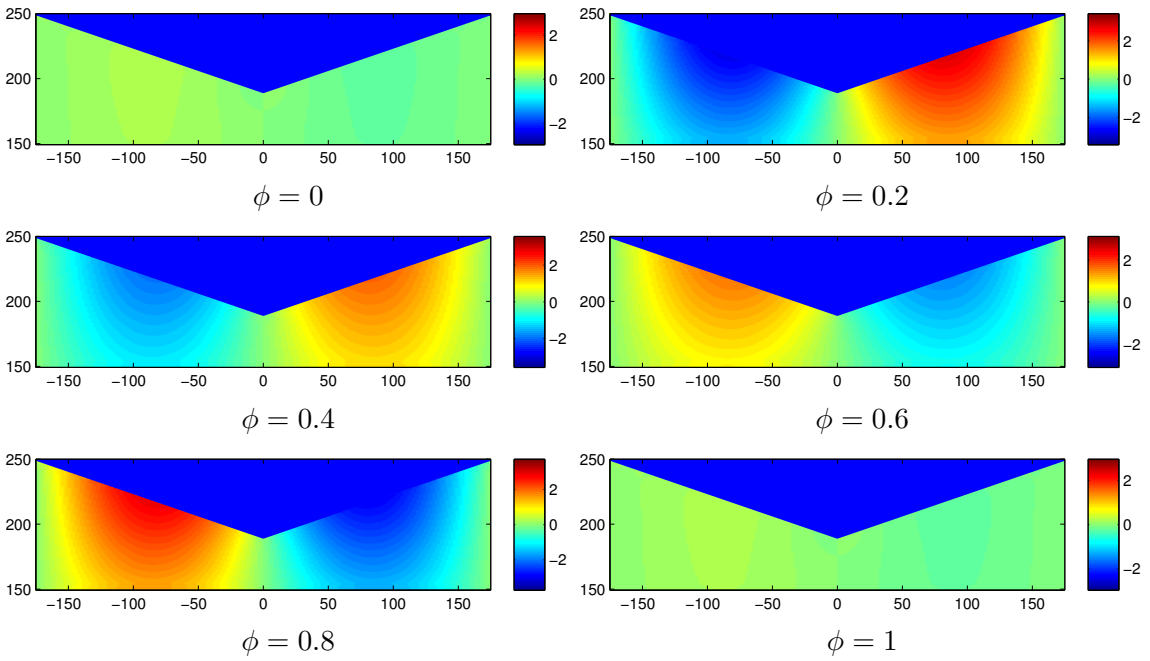

Figure 3.14 Field evolution of E_y at the 1st order surface plasmon mode. The fractional position within the optical cycle is labelled by ϕ.

550 nm and 350 nm. Comparison between the TM and TE polarisation plots of 3.16 and 3.12 reveals that these enhancements are present in both polarisations. In addition, they are periodicity independent suggesting that they are not due to a property of the grating. This apparent enhancement is therefore likely due to multilayer interference within the solar cell stack. The reason that these appear as an enhancement when the electrode grating is introduced is that the electrode displaces some of the active region, effectively decreasing its thickness. This shifts the spectral position of the interference modes, as discussed in Section 2.4. If this were the case, there should be a corresponding decrease in other areas of the spectrum, as these are shifted outside the constructive interference conditions. This is indeed clearly observed in Figure 3.16b, particularly evident for an aluminium electrode at wavelengths centred around 450 nm and 625 nm, where there is a significant detriment to the absolute absorption.

The changes in absorption due to multilayer absorption are somewhat poorly defined,

and this is due to the shape of the triangular grating used. The height profile of the grating means that different spatial positions within the cell exhibit different active layer thicknesses, and there is therefore a gradient in the conditions that lead to light trapping due to multilayer interference at the different positions across the grating. The overall effect is therefore to smooth the effects of interference leading to these somewhat ill-defined regions of enhancement and suppression.

To help visualise the multilayer interference, Figure 3.15 shows the averaged electric field plots at several wavelengths at a fixed grating period. The position and intensity of the field is generally seen to shift with small changes in wavelength, as can be seen in the sequence a-c). This wavelength dependence is exactly as expected from thin film interference. The field pattern is complex, however, and the maximum field intensity follows the grating profile. The overall effect of the interference is therefore difficult to predict without running simulations of the type demonstrated in this work. At shorter wavelengths around 350 nm, there is a good localisation of the field within the active region. This, coupled, with the high absorption properties of the polymer at these wavelengths leads to the strong absorption demonstrated in the short wavelength regions shown in Figure 3.16. At intermediate wavelengths around 450 nm, shown in Figure 3.15d, the field has a relatively high intensity in the PEDOT:PSS region where it will not contribute to photo-current. This is mirrored in the drop in absorption in these wavelengths. At longer wavelengths, around 500 nm, the polymer absorbs very strongly, so by this wavelength region strong absorption is evident.

Returning to Figure 3.16, there is a periodicity-dependent step-like feature starting at around 300 nm for a 200 nm period and extending up to around 600 nm for a 400 nm period. Several sources for this feature were investigated and it was found that the feature disappeared when the simulation was truncated such that it started within

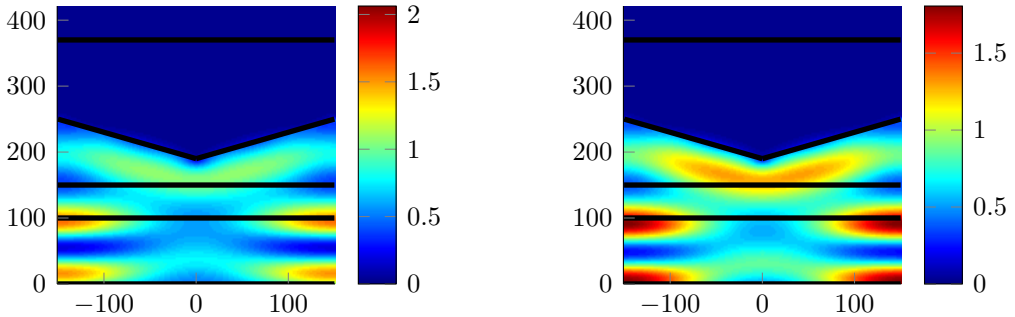

(a) 330 nm

(b) 350 nm

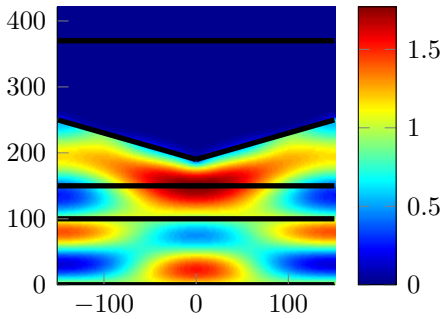

(c) 370 nm

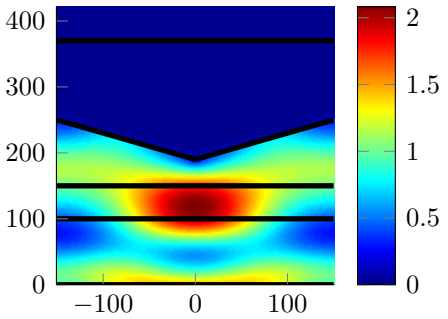

(d) 450 nm

Figure 3.15 Average electric field intensity plots at a number of wavelengths, as labelled.

the active region, as shown in Figure 3.16. The glass/ITO interface therefore plays a vital role in the appearance of this feature. The horizontal bands of enhancement due to multilayer interference are also seen to shift to longer wavelengths in this figure. This is due to the altering of the multilayer interference when the glass/ITO interface is removed.

Motivated by the difference in refractive index contrast between the ITO (2.25-1.6) and glass (1.5), I suggest that the step-like absorption feature could be due to total internal reflection (TIR). The grating will not be 100% efficient at coupling into surface plasmon modes and some of the light will be scattered as normal grating diffraction order modes. These result because light diffracts from the grating and the resulting destructive and constructive interface between light from different positions in the grating leads to a series of maxima and minima in intensity. Maxima occur at

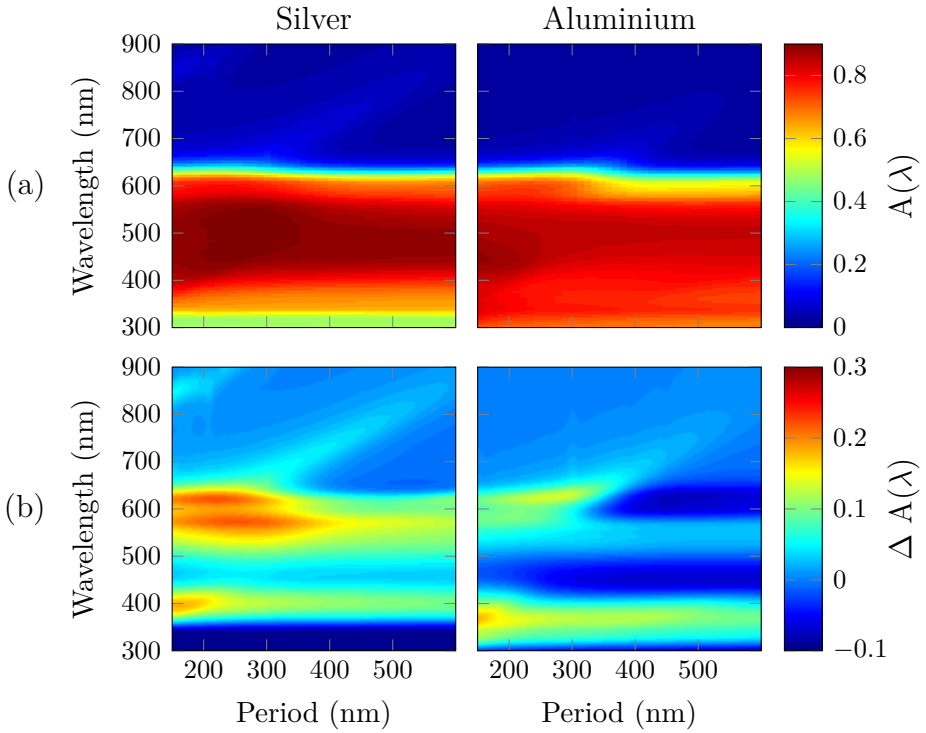

Figure 3.16 Plot of $A(\lambda)$, the fraction of incident photons absorbed by the active layer (a), and the absolute increase of A(λ), $\Delta A(\lambda)$, compared to a planar device (b), for a cell with active layer thickness 100 nm incorporating a triangular grating with height 60 nm, with a silver (left column) and aluminium (right column) electrode under TM illumination, with the simulation region was truncated within the ITO region.

angles θ_m given by Equation (3.5), where θ_i is the angle of incidence and the grating orders are indexed by an integer m, as discussed in Section 2.3.

$$\sin(\theta_m) = \sin(\theta) + \frac{m\lambda}{P} \tag{3.5}$$

Let us now focus on the primary grating order, for which $m = 1$, and normal incidence such that $\theta_i = 0°$. In this case, the mode scatters at an angle given by Equation (3.6), where n_a is the refractive index of the active layer:

$$\sin(\theta_m) = \frac{\lambda}{Pn_a} \tag{3.6}$$

This mode is refracted in the various layers of the solar cell structure, and is incident on the ITO layer with an angle θ_{ito} given by:

$$\sin(\theta_{ito}) = \frac{n_a}{n_i}\frac{\lambda}{Pn_a} \tag{3.7}$$

$$= \frac{\lambda}{Pn_i} \tag{3.8}$$

The critical angle for the ITO/glass interface, above which incident light undergoes total internal reflection, is given by Equation (3.9), where n_g and n_i are the refractive indices of the glass and ITO, respectively.

$$sin(\theta_c) = \frac{n_g}{n_i} \tag{3.9}$$

Thus, the condition for the scattering grating mode to undergo total internal reflection is given by:

$$\sin(\theta_{ito}) \geq \theta_c \tag{3.10a}$$

$$\frac{\lambda}{Pn_i} \geq \frac{n_g}{n_i} \tag{3.10b}$$

$$\lambda \geq n_g P \tag{3.10c}$$

Light that has undergone total internal reflection makes another pass through the active region where it has another chance to be absorbed, leading to an absorption enhancement. Wavelengths greater than $n_g P$ should be enhanced, and this explains the step-like feature. We would also not expect any polarisation dependence for this effect given this explanation, and this is indeed the case as can be observed from the step-like TIR enhancement feature in the TE absorption data of Figure 3.12. The enhancement from the TIR occurs in conjunction with the enhancement due to the multilayer interference, and it is therefore masked in several regions of the spectrum. The step is most clearly visible for grating periods from 300 nm to 400 nm.

In summary, I have identified three sources of enhancement which arise from the introduction of the grating at the rear electrode:

1. surface plasmon excitation

2. shift in the multilayer interference

3. total internal reflection of the 1st order grating mode

It is now instructive to assess the relative magnitudes of the enhancements due to these three mechanisms. Although the surface plasmon mode demonstrates a strong enhancement compared to the planar device, this occurs in a region of the spectrum where the polymer actually absorbs relatively weakly (see Figure 3.5). In absolute terms, the absorption at the surface plasmon mode contributes an additional 6% at its resonance wavelength. The enhancement occurs over a wavelength range of around 50 nm, but the absolute enhancement drops off quickly with wavelength, as the resonance criteria is no longer fulfilled. We can compare this with the absolute enhancement from the TIR of the grating mode, which leads to a further enhancement of around 5% at its onset. There will also be enhancement at higher wavelengths, but this is difficult to separate from the contribution due to the multilayer interference.

As noted above, the TIR enhancement is most noticeable at grating periods between 300 nm to 400 nm. Section 4.4 will also demonstrate that this range of periods leads to the best overall device enhancements. This implies that the contribution from TIR plays a significant role, and perhaps one that has been underplayed in the literature. It is difficult to isolate the proportion of the enhancement that is due to multilayer interference, as this mechanism provides both an enhancement and a detriment in different regions of the spectrum. For this reason, the most practical method to assess the optimum grating devices is to perform large parameter sweeps, as demonstrated in Chapter 3. The FDTD method is ideally suited to performing these sweeps.

3.7 Chapter summary

I have identified that a strong degree of optimisation can take place even within a simple planar device geometry. Results of simulations using both FDTD modelling and transfer-matrix methods were presented and show close agreement. Varying the thickness of the various layers in the device structure has a strong influence on the absorption within the active layer. This is due to interference within the multilayer stack which alters the spatial distribution of light within the device. In general, it is preferable from an optical standpoint to use thin layers prior to the active region, but this must be balanced against their electrical functions in the device. The active layer should then be optimised to make best use of the maxima due to the multilayer interference.

Gratings can be employed to alter the absorption within these devices and make a difference to both the spectral distribution and overall magnitude of absorption. I have assessed the mechanisms underlying the enhancement of thin film organic solar cells based on a P3HT:PCBM bulk heterojunction using short period gratings and have identified three primary mechanisms by which this enhancement takes place. There is a strong absorption due to a 1st order surface plasmon enhancement which occurs at long wavelengths where the absorption within the active region begins to diminish. This provides a welcome boost in absorption in this wavelength region which contributes a significant overall absorption current enhancement to the full devices. In addition, multilayer interference within the devices leads to both enhancement and detriment in absorption in different regions of the spectrum, with a strong dependence on the layer thicknesses. This behaviour is drastically altered with the incorporation of a grating as this effectively changes the length of the active region in a non-uniform fashion across the device. Finally, the grating order

modes can couple back into the device due to the refractive index contrast at the interfaces between the layers, leading to an additional pass through the active layer and increased absorption there. The above enhancements play comparable roles in the final absorption currents and occur simultaneously. In order to design optimum devices, it is therefore not possible to consider one effect in isolation.

CHAPTER 4

Optimising gratings at normal incidence

4.1 Introduction

In this chapter, I describe several techniques and simulations in order to further investigate the effect of a structured electrode on thin film organic cells. Theoretical dispersion plots are calculated for the plasmonic interfaces and these are correlated with the previous simulation data. These results lead to a calculation of the propagation length of surface plasmons at the metal/active interface. The results from the above explorations provide an insight into the methods that can be used to optically enhance thin film organic solar cells.

I then proceed to perform an optimisation of the grating geometry in order to achieve

maximal absorption. This is initially performed for a triangular grating, but leads to a comparison between both a triangular and a rectangular grating geometry. A brief qualitative discussion of the potential charge extraction effects of incorporating a grating into these devices is also included. I also take into account practical fabrication considerations which leads to an investigation of the effect of rounding of the sharp features of triangular gratings. Finally, I discuss the possibilities of 2D gratings as a means to mitigate the polarisation dependence of a 1D grating. Overall, the results of this chapter provide an important insight into the realistic optical benefits achievable from the incorporation of a nano-scale grating in the rear electrode of organic solar cell devices.

4.2 Methods

The methods employed in this section build upon the FDTD simulation methods described in Chapter 3. Where additional calculations or methods are employed, they are described within the relevant sections.

4.3 Theoretical band structure calculations

The results from the previous chapter have provided information on the mechanisms of enhancement by assessing the absorption within the active layer. This absorption is ultimately the most important metric when designing solar cells. In addition, however, I now take a more fundamental look at the mode structure within the device by investigating the dispersion plots of the structure. For these, I plot the energy of a mode as a function of the in-plane momentum k_x. These plots enable us to identify surface plasmon modes within the structure and these can then be correlated

with the absorption spectra. In addition, they can identify the surface plasmon excitation wavelength, even where this is not evident directly from the absorption plots. The highly wavelength-dependent permittivities of the photoactive material lead to complex dispersions. They help to explain why only certain ranges of the grating period provide enhancements via surface plasmons, and therefore provide greater insight into the design of the grating structures.

One method of generating dispersions for the gratings is to plot the dispersion for the surface plasmon, then take into account the additional momentum provided by the grating. The theory underlying this is explained in Section 2.3. This method was achieved using code written in the Python programming language. The dispersion curve for the surface plasmon was calculated using Equation (2.18) in which ϵ_a and ϵ_m, the wavelength-dependent permittivities of the active and metal layers, respectively, were used:

$$k_{sp} = \frac{2\pi}{\lambda}\sqrt{\frac{\epsilon_a \epsilon_m}{\epsilon_a + \epsilon_m}}. \tag{4.1}$$

The permittivity data was the same as that used for the FDTD simulations in Section 3.2. The resulting surface plasmon dispersion curve is shown in Figure 4.1c. This is shown alongside two further dispersion curves where the active layer was treated as a dielectric with a constant real refractive index of 2 in Figure 4.1a, and where the metal was treated under the Drude-Lorentz model in Figure 4.1b. The figures have been plotted using wavelength on the y-axis, rather than energy or frequency which are more typically employed. They are also truncated to the wavelengths of interest for organic solar cells. This is useful in the current context and helps to directly relate the plots to features in absorption data. The figures demonstrate the strong effect of the input refractive index data on the conclusions drawn. Using a constant value for the refractive index of the active layer is insufficient to capture the intricacies of the surface plasmon dispersion curve. Using experimental

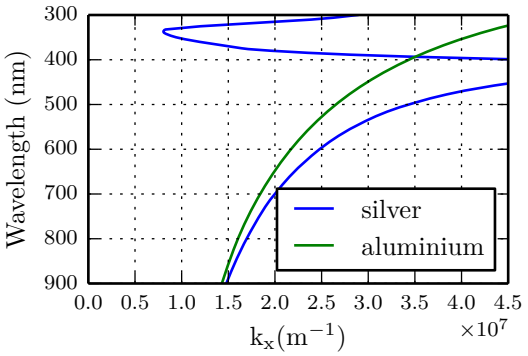

(a) Metal: experimental data; active: dielectric with constant refractive index n=2

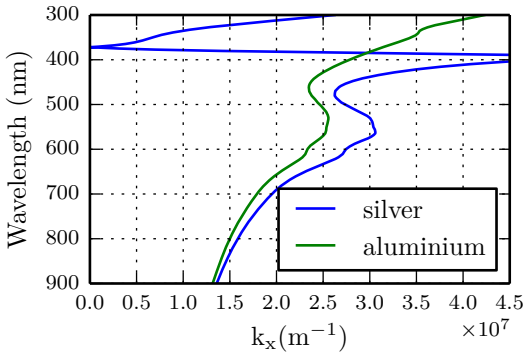

(b) Metal: Drude-Lorentz model; active: experimental data.

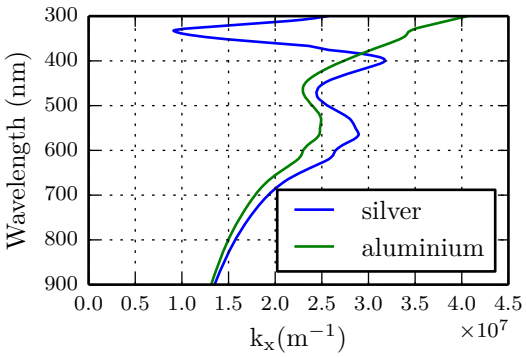

(c) Metal: experimental data; active: experimental data

Figure 4.1 Calculated dispersion curves for an active/metal interface. The source of the permittivity data is given in the figure label for the metal and active layer. Experimental data are taken from literature sources [86, 88]

data for the active layer and a Drude-Lorentz model for the metal does a better job, but there are still some discrepancies, particularly noticeable at shorter wavelengths. The raw experimental permittivity data was therefore used for the theoretical calculations that follow.

In order to generate dispersion plots that take into account the effect of the grating at the electrode, Equation (2.19) was employed. The equation is restated here, followed by substitution for the in-plane momentum k_x and rearrangement:

$$k_{sp} = k_i \sin(\theta_i) + mk_g \tag{4.2a}$$

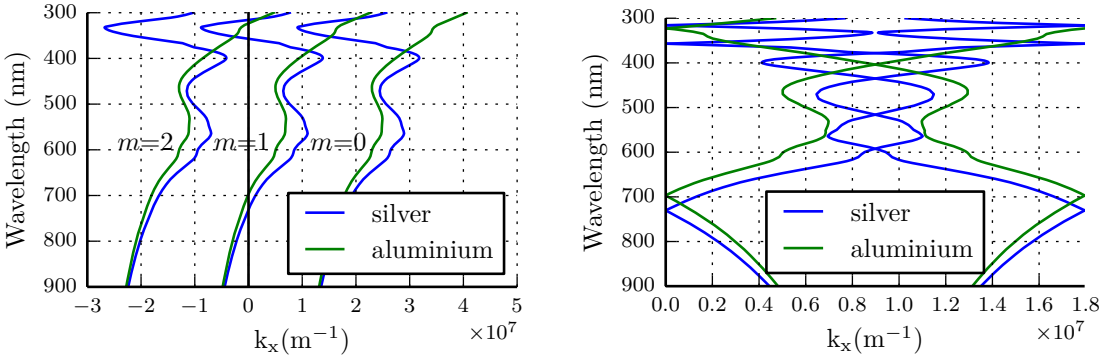

(a) Dispersion for $k_{sp} > 0$ with modes labelled by grating order integer m

(b) Band structure in the reduced zone scheme for $0 < k_x < k_g$

Figure 4.2 Calculated dispersion for an active/metal interface incorporating a grating with periodicity 350 nm.

$$k_x = k_{sp} - mk_g \tag{4.2b}$$

Equation (4.2b) was then used with the grating momentum $k_g = \frac{2\pi}{P}$, and k_{sp} from the surface plasmon dispersion equation using experimental data to plot the wavelength of the incident light against k_x. This is shown in Figure 4.2 for a grating period of 350 nm. Only positively propagating values for k_{sp} are included in Figure 4.2a, for clarity. The modes have been labelled with the integer m from Equation (4.2b), that corresponds to the order of the grating mode that would excite the SPP. In Figure 4.2b, all values of k_x are included, but the range of k_x is truncated to k_g. The plots are therefore analogous to band structure plots in the reduced zone scheme used in condensed matter physics and will be referred to as such for the rest of this section.

Under the action of the first order grating mode, with $m = 1$, there is sufficient momentum to excite the surface plasmon. There is a crossing with $k_x = 0$ at around 730 nm and 700 nm for the silver and aluminium electrodes, respectively. This corresponds to the wavelength at which the SPP can be excited under normal

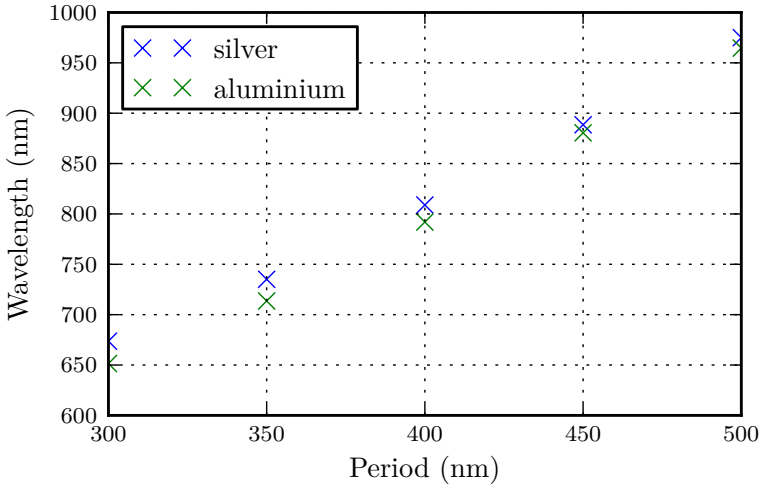

Figure 4.3 Wavelength of the first order surface plasmon mode resonance as a function of grating period.

incidence, for which $k_x = 0$. This is of great importance for the design of plasmonic solar devices which are typically oriented normally to the incident light. This also corresponds to the incident source used in the absorption plots previously. At angled incidence, the surface plasmon mode can also be excited and exhibits two branches increasing and decreasing in wavelength.

To assess the effect of altering the periodicity of the grating on the surface plasmon, the first order crossing with $k_x = 0$ was plotted for a variety of grating periods, as shown in Figure 4.3. This provides a useful overview of the dependence of the surface plasmon enhancement on the periodicity of the grating in order to obtain coupling at normal incidence. It also confirms that a grating periodicity of 300 nm to 400 nm is required in order to achieve a surface plasmon enhancement that falls within a useful region of the absorption tail of the P3HT:PCBM blend.

These theoretical band structures show good agreement with the location of the observed absorption tails evident in the absorption plots of Figure 3.16, shown again in Figure 4.4 for reference. This lends further evidence that the absorption tail identified previously is due to enhancement via the excitation of an SPP.

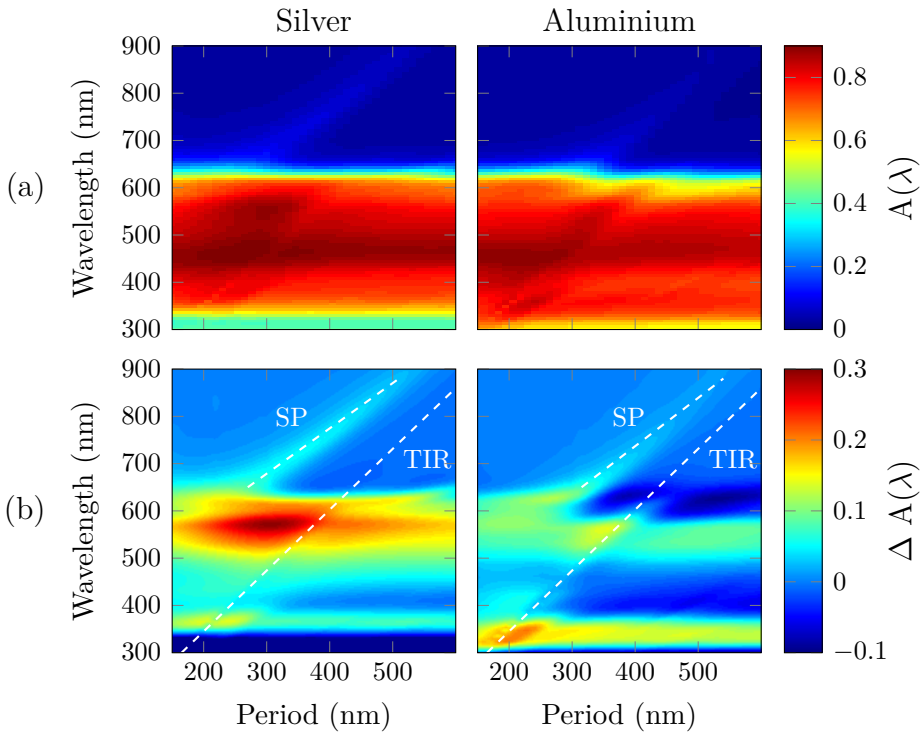

Figure 4.4 Plot of $A(\lambda)$, the fraction of incident photons absorbed by the active layer (a), and the absolute increase of A(λ), $\Delta A(\lambda)$, compared to a planar device (b), for a cell with active layer thickness 100 nm incorporating a triangular grating with height 60 nm, with a silver (left column) and aluminium (right column) electrode under TM illumination. Duplicated for reference.

It is useful to consider the reason for the limited range of grating periods for which first order surface plasmon excitation is beneficial. At grating periods below 250 nm, which are not shown in Figure 4.3, the surface plasmon bands become increasingly difficult to discern in the absorption spectra of Figure 3.16. Comparison with the theoretical band structure plots shown in Figure 4.5a reveals the cause. At these shorter wavelengths, the surface plasmon no longer makes a $k_x = 0$ crossing at higher wavelengths, but does so at far shorter wavelengths of around 400 nm, due to a sudden change in the refractive index of the photoactive polymer at these wavelengths. There is already strong absorption in the photoactive region at these wavelengths, so the effect of the surface plasmon is difficult to discern.

Now, for grating periods larger than 500 nm, also omitted from Figure 4.3, the

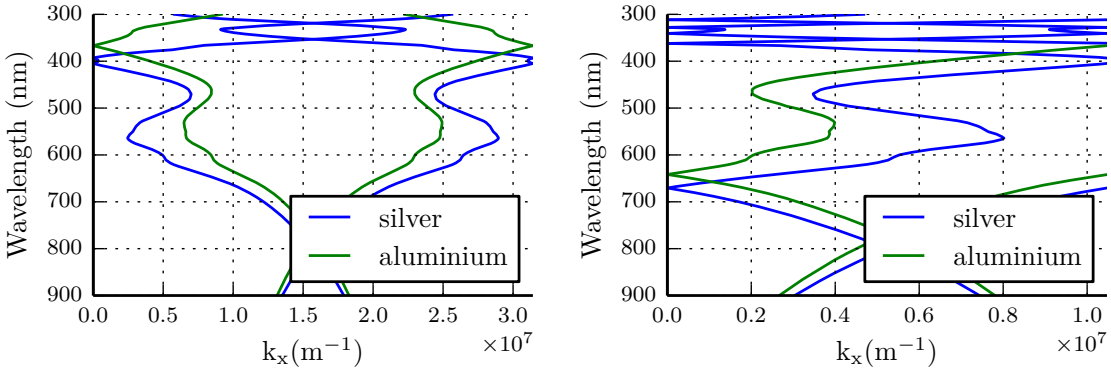

(a) 200 nm periodicity

(b) 600 nm periodicity

Figure 4.5 Theoretical band structures for an active/metal interface, for grating periods as labelled.

first order surface plasmon occurs at wavelengths beyond the absorption of the P3HT:PCBM. Continuing to even higher periods around 600 nm, however, results in an additional crossing in the wavelength range of interest due to the second order surface plasmon mode. This is shown in the theoretical band structure plot of Figure 4.5b. These do not appear to make a significant contribution to absorption current as these longer grating periods do not lead to significant enhancements over control devices. This may be because other factors limit the absorption current at these longer periodicities. In addition, coupling into higher order modes is weaker than the first order modes. This suggests that higher order modes do not play a significant role in the enhancement of P3HT:PCBM solar cells.

The preceding discussion serves to illustrate the significance of the wavelength dependent permittivity of the active layer on the surface plasmon response. The sudden changes in permittivity at around 500 nm lead to changes in the surface plasmon dispersion such that the range of wavelengths for which a k_x can be effected are somewhat limited for 1st order surface plasmon modes. It is also highly important to design grating structures using real material data, and not to rely on Drude metal approximations which would not recreate this behaviour.

There is an additional surface plasmon which occurs at the metal/air interface of the rear electrode. In reality, it is difficult to excite this additional surface plasmon mode directly, as light incident from the air would not have sufficient k_x to allow the coupling. However, it is possible to excite this mode by coupling from the surface plasmon at the active/metal interface. This occurs for a metal film which is sufficiently thin such that the confinement of the surface plasmon mode from the active/metal interface extends to the upper interface. For the cell structure in question, however, the electrode is too thick to efficiently support this coupling. It is therefore not observed in the absorption spectra of Figure 3.16. In any case, it would not lead to an increase in absorption within the active material and would therefore be parasitic in nature and should therefore be avoided by employing a sufficiently thick rear electrode. In practical devices, the rear contact is typically sufficiently thick to prevent this coupling.

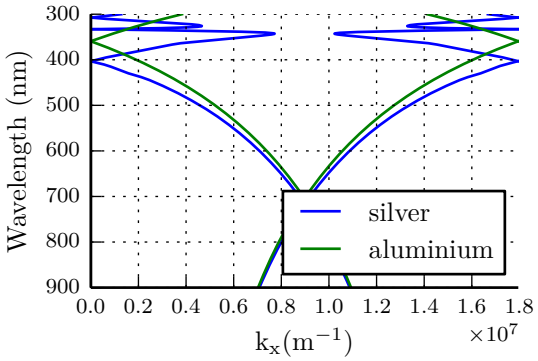

Figure 4.6 Theoretical band structure for a metal/air interface with periodicity 350 nm.

It is also instructive to look at the theoretical propagation lengths of the surface plasmons within the devices. These were calculated using the formula discussed in Section 2.2.3 and the results are shown in Figure 4.7. From the figure it is apparent that the propagation length is very short up to a wavelength of 500 nm at which point it begins to increase before increasing dramatically from around 600 nm. This is due to the strong absorption below 600 nm of the photoactive polymer. Comparing

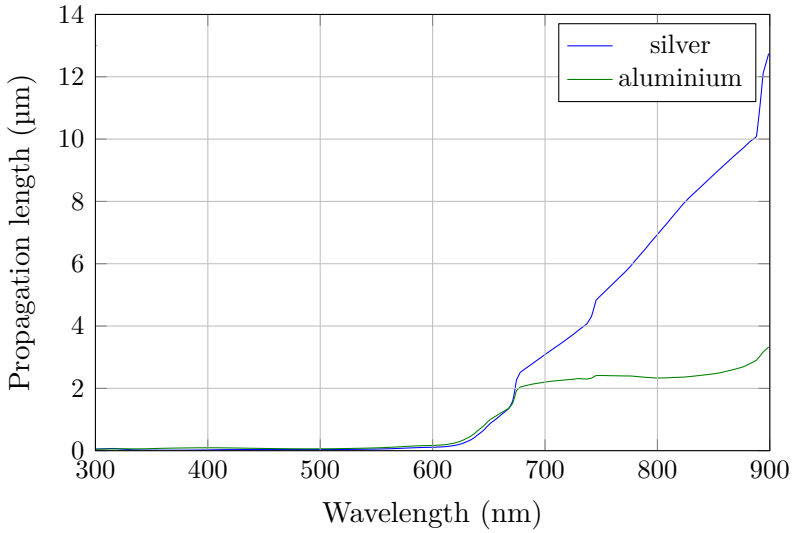

Figure 4.7 Propagation length of surface plasmons at an active/metal interface for silver and aluminium, as labelled.

silver and aluminium, the silver exhibits a much longer propagation length than aluminium towards longer wavelengths. This implies that it will be a more effective electrode material to effect surface plasmon enhancement in this wavelength region.

Finally, it is worthwhile noting that the band structures so far presented are an approximation to the true band structure of the solar cell devices. This is because the dispersion equation for a planar interface has been used to describe the surface plasmon momentum k_{sp}. In reality, the dispersion curve for an interface incorporating a grating is a complicated function of the grating parameters. For shallow gratings, the planar dispersion provides a reasonable approximation [99], as demonstrated by the good correlation with the absorption data. FDTD simulations inherently take into account the exact geometry of the grating and therefore give a more accurate insight into the optical effects within featured solar cells.

4.4 Optimisation of devices

In order to assess the overall performance of the devices, it is necessary to integrate across the whole absorption spectrum. Equation (3.4), described in Section 3.3, was therefore employed to calculate the absorption current J_{abs} for the plasmonic devices. This allows a direct comparison with the results for planar devices from Chapter 3. Anticipating that the absorption current will depend strongly on the grating parameters, I swept both the grating period and height. The sweep was confined to values that provided good enhancements. Longer period gratings, for example, did not provide significant enhancements over planar devices and in fact led to a detriment due to the reduction of photoactive material, without significant enhancement.

Three grating geometries were investigated: triangular, rectangular, and sinusoidal. These were chosen as they are the simplest periodic shapes. All periodic structures can be described as a superposition of sinusoidal functions. The frequency of these, known as the spatial frequencies, can be ascertained using a Fourier Transform. The sinusoidal grating has only a single frequency, whereas the triangular and square gratings are formed of an infinite series of odd harmonics. It was interesting to observe whether these would have a significant effect on the enhancement. This section opens with a discussion of the triangular grating, which led to the optimum enhancement. This is followed by a discussion of the rectangular and then sinusoidal grating, in order of diminishing enhancement.

4.4.1 Triangular grating

The width of the grating is chosen to be equal to the period at this stage, such that the fill factor was equal to 1. The active layer thickness was also varied, as this might strongly alter the absorption properties. The simulation geometry is shown in Figure 4.8. The results of these sweeps are shown in Figure 4.9.

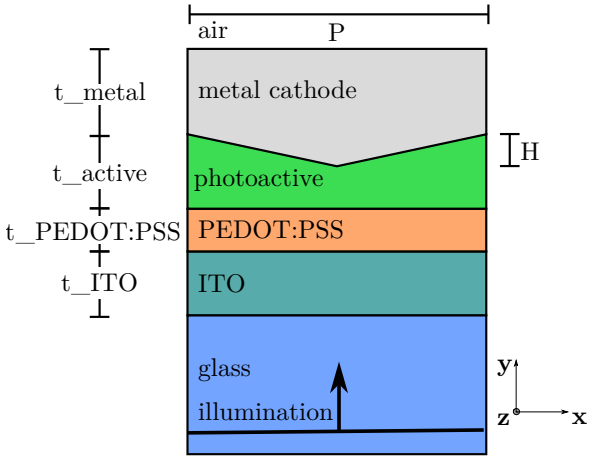

Figure 4.8 Schematic of the triangular grating geometry.

Absorption currents of up to 13.86 mA cm^{-2} and 13.13 mA cm^{-2} are possible for silver and aluminium, respectively, with optimal periods of about (280 ± 30) nm and (300 ± 30) nm, respectively. The optimum enhancements are obtained for an active layer thickness of 120 nm, incorporating a 70 nm high grating. This may have implications for the fabrication of real devices as shorter periods are often harder to obtain using Focussed Ion Beam techniques, as will be discussed in Chapter 6. The aluminium electrode leads to optimum devices with smaller absorption currents than those with a silver electrode. This must be balanced against the charge extraction properties, however, for which aluminium is a more conventional choice. This is due to its lower workfunction of 4.25 eV, which better matches the LUMO of PCBM, compared to the work function of 4.35 eV [100] for silver, and therefore improves the charge extraction properties. In addition, aluminium is a lower cost material so

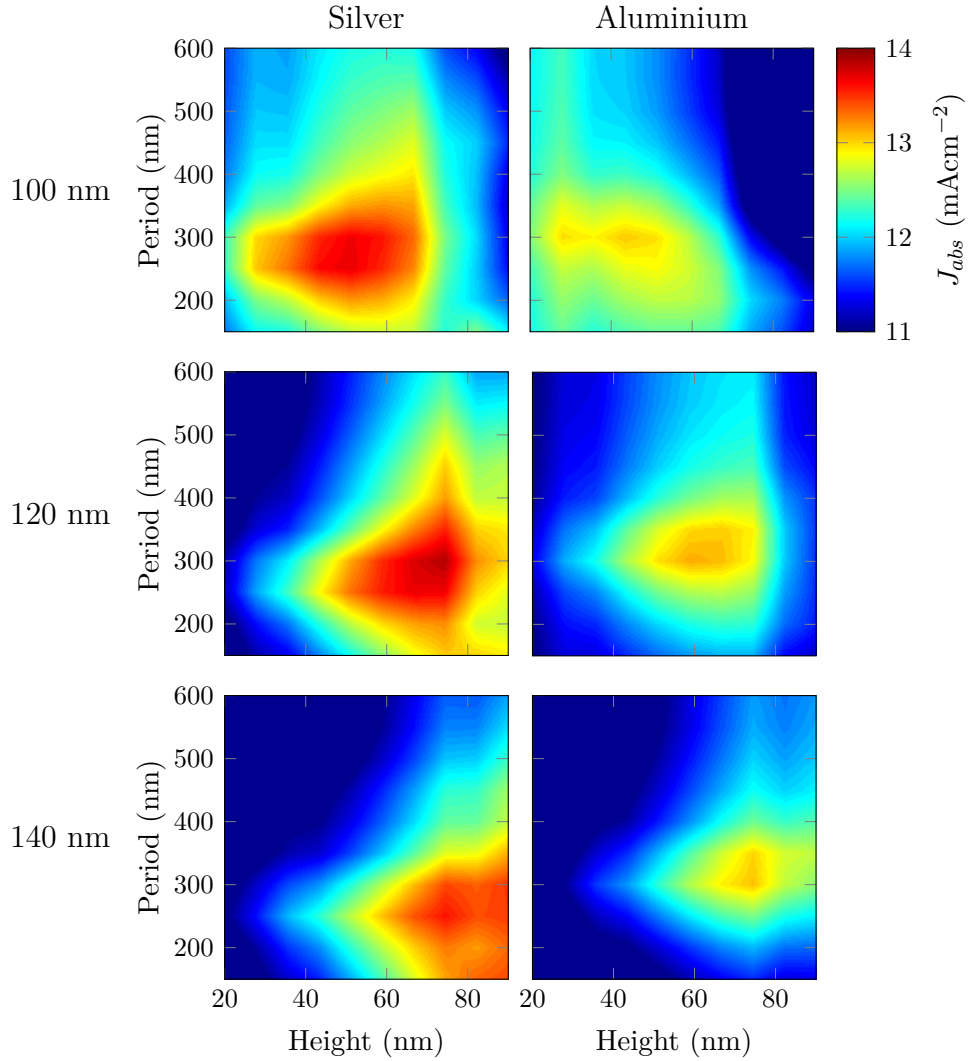

Figure 4.9 Absorption current J_{abs} within an active layer of thickness 100 nm, 120 nm, and 140 nm, as a function of grating height and period, for both silver and aluminium triangular gratings, as labelled.

provides a cost benefit.

It is interesting to consider the propagation lengths of the surface plasmons using the two different electrode materials. Referring back to Figure 4.7, the propagation lengths of the surface plasmon for silver and aluminium are both around 1 µm to 2 µm at a surface plasmon wavelength of 650 nm. This is clearly sufficient to effect a significant increase in the absorption within the active layer. At longer wavelengths, the silver has an increasing propagation length compared to aluminium. At longer grating periods, the surface plasmon wavelength is longer and so the propagation length increases. Due to this, the silver maintains a stronger absorption tail at longer periods than the aluminium grating. There is, however, still a significant enhancement from the aluminium electrode so a relatively short propagation length of a few micrometres is sufficient for enhanced absorption.

The height of the grating should bear a strong relation to the degree of coupling into the surface plasmon mode [101]. At small grating heights, the grating is treated as a weak perturbation of the planar surface and the coupling into the surface plasmon mode follows the square of the amplitude of the grating. At larger heights, the phase velocity of the surface plasmon decreases, leading to a distortion of the surface plasmon dispersion. On the one hand, there is therefore an optimum height for the grating which will lead to maximal coupling into the surface plasmon modes at the desired wavelength. On the other hand, as the grating height increases, an increasing volume of active material is displaced which therefore decreases absorption. This must be balanced against the beneficial absorption arising from the surface plasmon. For a given active layer thickness, there is therefore an optimum height that arises from this balance. This optimum is relatively broad, however, and large currents are observed over a height range of around ±60 nm. The absorption currents are therefore relatively robust to changes in grating height.

There is similarly a robustness to changes in grating period. The regions of maximal current allow a range of periods of around 100 nm centred at the optimum. The period will affect the position of the surface plasmon resonance, and this therefore suggests that this position is not critical for the enhancement of the devices, within a small range. The dependence of the surface plasmon wavelength on the grating period was previously investigated in Section 4.3. In that section, an explanation was provided for the limited range of grating periods for which this surface plasmon mode can be excited. It explains why there is a steep cut-off as a function of grating period. At longer periods, the first order surface plasmon mode falls outside the absorption tail of the polymer. There is still, however, a relatively high robustness of the absorption to grating period. This robustness is of benefit for the fabrication of practical devices, as it allows a broad tolerance in the fabrication of the grating.

The grating parameters required to achieve an optimum enhancement display a clear dependence on the thickness of the active layer, however. As the active layer is made thicker, a taller grating is required in order to effect an optimum enhancement. For the triangular case, the optimum grating height occurs at a height of approximately half of the active layer thickness. It is interference effects within the multilayer stack which lead to this dependence on the active layer thickness. Overall, the grating devices demonstrate good insensitivity to active layer thickness, however, when compared with the planar devices seen previously, as enhancements are achievable over a broad range of active layer thicknesses. They do benefit from optimisation of the grating geometry to the active layer thickness, but with broad tolerance to grating parameters. This provides an additional advantage over planar devices.

It is common within the literature to compare optimum devices incorporating gratings to planar devices with the same original active layer thickness. Using this method on my results, enhancements of up to 30% and 25% were obtained for silver and

aluminium electrodes, respectively. This suggests that by starting with a cell of a particular active layer thickness and incorporating a grating, it is possible to achieve a substantial increase in absorption. To put this in context of previous work, Abass *et al.* demonstrated enhancements compared to planar devices of 15.6% using a silver electrode [1]. Those simulations included only the polymer active region and cell cathode, however, and the effect of additional hole transport and anode layers present in a working device was not taken into account. The current work therefore demonstrates that greater enhancements are possible with the inclusion of all the layers in the structure. These additional layers have a strong influence on the optical response of the structure and introduce additional modes which act to enhance the absorption, as discussed in Section 3.6.

The above comparison to planar devices is also not strictly fair, as the incorporation of the grating displaces some of the active material reducing the average thickness. The absorption current is strongly dependent on active layer thickness, as seen previously in Figure 3.6, due to multilayer interference effects. As a result some of the large enhancements seen above are simply due to changing this active layer thickness, effectively moving position on Figure 3.6. In order to negate this effect, I make a comparison to an optimised planar device, maintaining a PEDOT:PSS thickness of 50 nm, which is typical for fabricated devices. In this case, enhancements of 9.8% and 4.3% are obtained for silver and aluminium electrodes, respectively. This is a marked decrease from the large enhancements often cited in the literature, but gives a more accurate reflection of the optical benefits that can be obtained using these gratings.

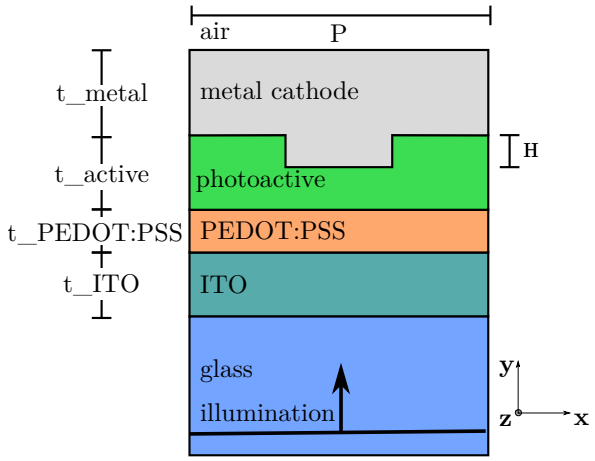

Figure 4.10 Schematic of the rectangular grating geometry.

4.4.2 Rectangular grating

An alternative simple grating geometry is that of a periodic array of rectangles. The fill factor is set to 0.5, such that the grating is symmetric and presents one periodicity, and will have the same area as the triangular grating studied previously. A schematic of this geometry is given in Figure 4.10. This grating geometry could conceptually be fabricated using methods such as electron beam lithography.

Figure 4.11 displays the absorption current densities for a rectangular grating. The optimum rectangular grating affords slightly lower current densities than the triangular grating at 13.44 mA cm^{-2} (silver) and 12.70 mA cm^{-2} (aluminium) compared to 13.86 mA cm^{-2} (silver) and 13.13 mA cm^{-2} (aluminium) obtained for a triangular grating previously. The optimum region for the rectangular grating is more clearly defined than the triangular grating, and may therefore be more sensitive to fabrication tolerance. This is particularly evident with respect to the grating period and height, where there is a sharp cut-off. This may be due to the smearing of the multilayer interference that occurs due to the gradual change in height of the triangular grating. This contrasts with the rectangular grating which has a sharp

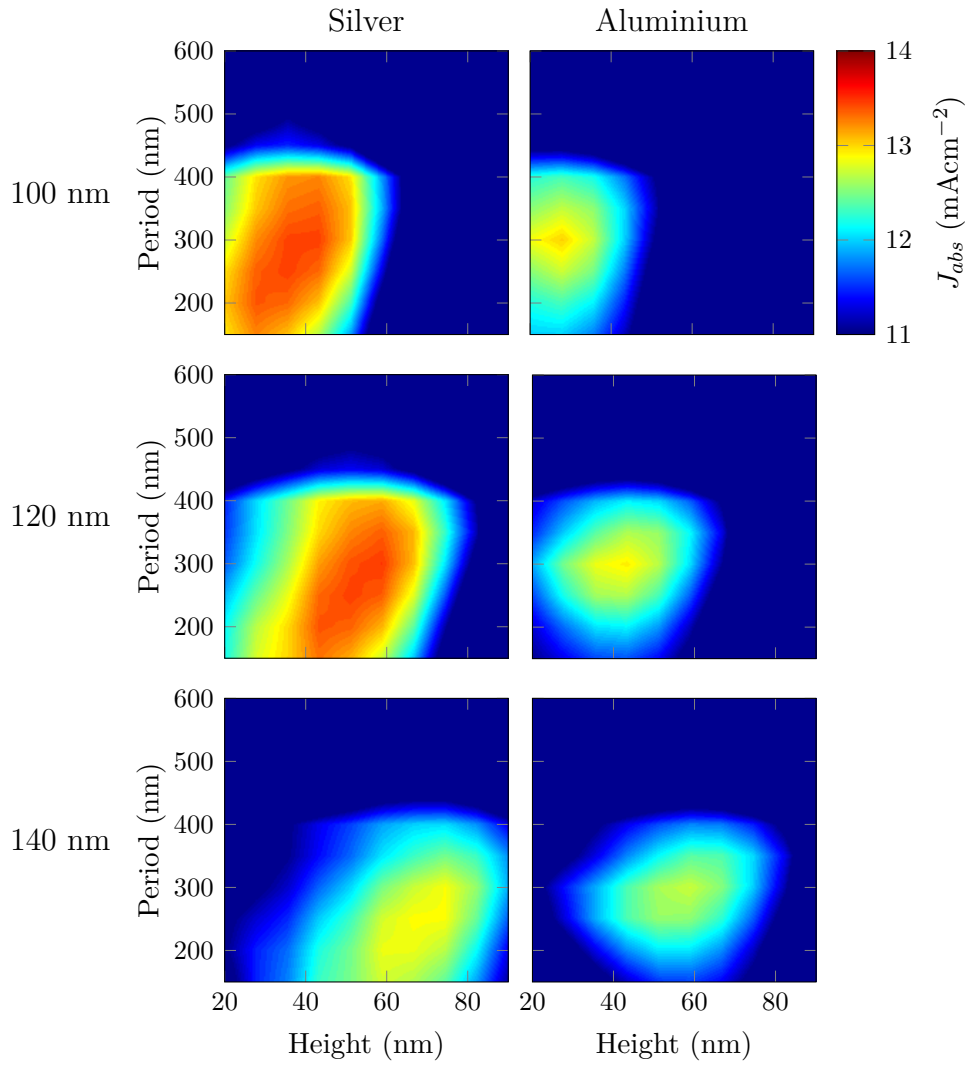

Figure 4.11 Absorption current J_{abs} within an active layer of thickness 100 nm, 120 nm, and 140 nm, as a function of grating height and period, for both silver and aluminium rectangular gratings, as labelled.

step change in height. In addition, the rectangular grating necessitates a grating that is about 10 nm shallower than the triangular case.

A comparison can be made to the results of the simulations obtained by Sefunc *et al.* [2]. They demonstrated optimal enhancements of up to 21% averaged between TE and TM polarisation. The optimum occurs at an extremely short grating period of around 140 nm. In addition, the enhancement tails off rapidly as the grating period increases. This contrasts with my results which demonstrate optimal enhancements at

far longer periods of around 300 nm. A strong surface plasmon peak is not apparent in the spectral absorption data of the Sefunc *et al.* paper. This is perhaps indicative that the true origin of their enhancements at these short periods do not lie with surface plasmons. I observe a small absorption tail extending up to 680 nm for a grating period of 350 nm in their data. This is far more reminiscent of the surface plasmon peak that I observe in my absorption data.

4.4.3 Sinusoidal grating

A sinusoidal grating is a simple grating geometry and the other grating geometries can be considered as a superposition of sinusoidal gratings. A schematic of the sinusoidal geometry is shown in Figure 4.12. The absorption current as a function of grating parameters is displayed in Figure 4.13.

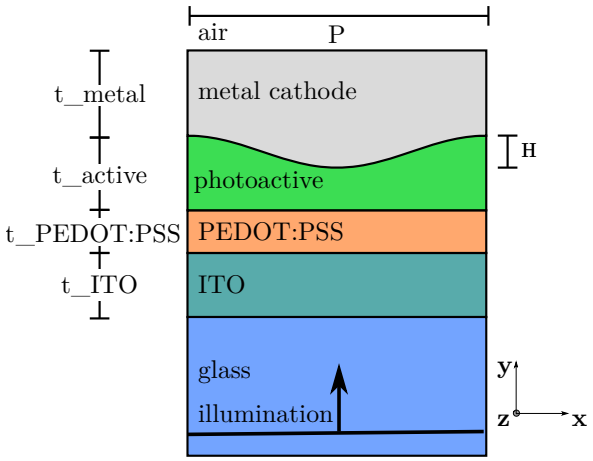

Figure 4.12 Schematic of the sinusoidal grating geometry.

The optimum grating parameters lead to absorption currents of 13.62 mA cm^{-2} and 12.96 mA cm^{-2} for silver and aluminium gratings, respectively. The region of enhancement is broad and not clearly defined like the rectangular case, and is more reminiscent of the triangular grating. This is likely due to the gradual change

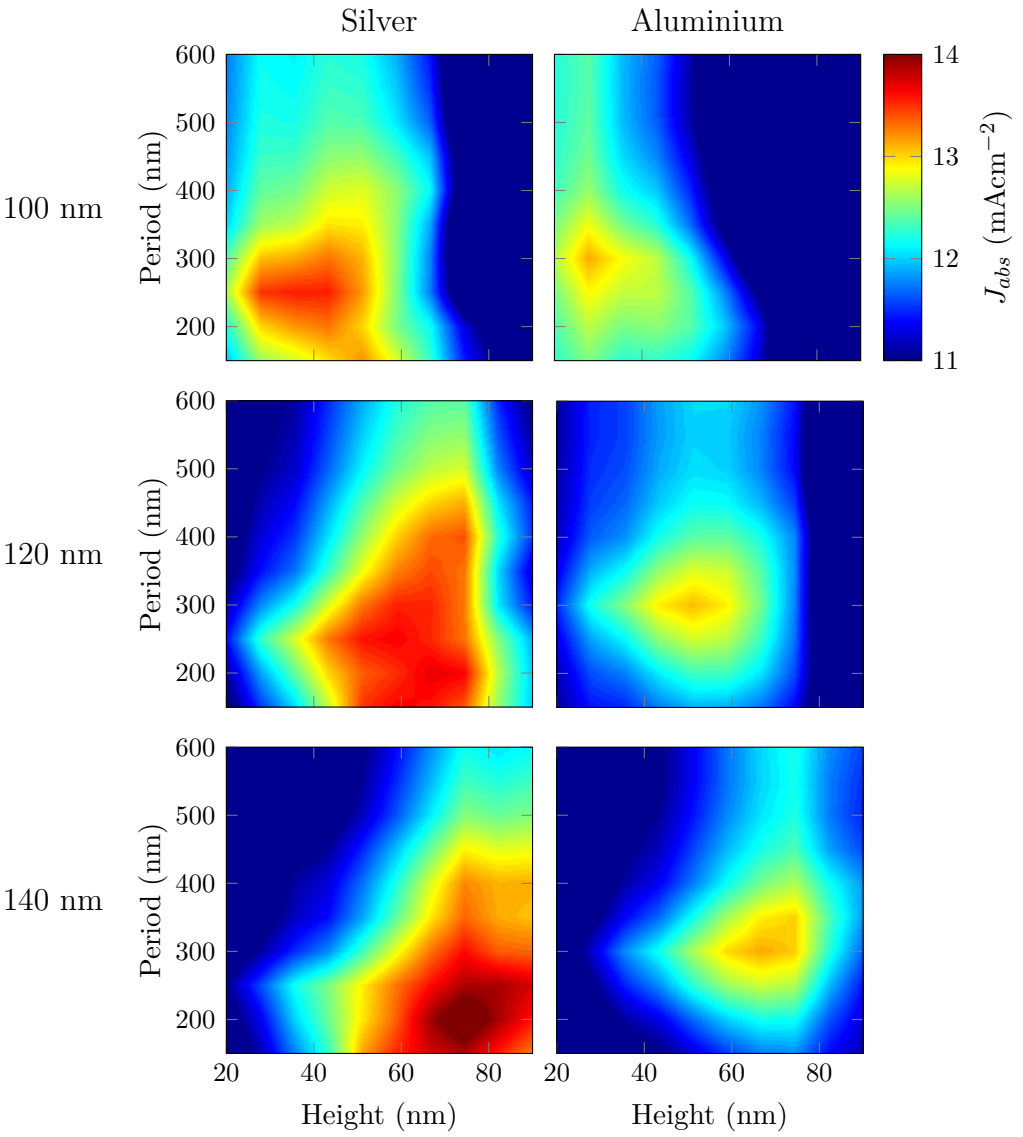

Figure 4.13 Absorption current J_{abs} within an active layer of thickness 100 nm, 120 nm, and 140 nm, for a sinusoidal grating, as a function of grating height and period, for silver and aluminium sinusoidal electrodes, as labelled.

in grating height due to the sinusoidal shape, which leads to a smoothing of the interference effects, as discussed for the triangular case. Broad enhancements are therefore visible over a periodicity range of arout 200 nm and a height range of around 40 nm. This has positive implications for the fabrication of real devices, as before, as the tolerance to variability in fabrication is high.

4.4.4 Optimisation summary

To summarise, the different grating geometries exhibit optimum absorption currents as given in Table 4.1.

	Metal	
	Silver	Aluminium
Planar	12.62	12.59
Sinusoidal	13.62 (P=220, H=70, T=140)	12.96 (P=300, H=70, T=140)
Triangular	13.86 (P=280, H=70, T=120)	13.13 (P=300, H=70, T=120)
Rectangular	13.44 (P=300, H=60, T=120)	12.70 (P=300, H=45, T=120)

Table 4.1 Summary of optimised absorption currents J_{abs} in $\mathrm{mA\,cm^{-2}}$ for a number of grating geometries, for both silver and aluminium electrode materials. The grating geometry for the optimum absorption is listed in nm, where P is the grating period, H is the grating height, and T is the active layer thickness.

It can be seen from the summary that whilst all of the grating geometries offer some enhancement over the optimised planar devices, the triangular grating affords the most enhancement, followed by the sinusoidal, and then rectangular geometry. For a given periodicity, the first order surface plasmon wavelength will be largely similar for the different geometries.

The triangular and rectangular gratings can be decomposed into an infinite series of odd harmonics of the fundamental period of the grating. These additional harmonics will permit additional modes, both for surface plasmons and TIR. However, the sinusoidal grating actually leads to larger optimum absorption currents compared to the rectangular grating. This suggests that these additional modes do not contribute significantly. This may be due to poor coupling efficiency, but also because the wavelength range for these modes would be in regions of the spectrum where it would not be beneficial, due to the limited absorption spectrum of the photoactive polymer.

The coupling efficiency for the different gratings into the first order mode will depend

on the shape of the grating. In addition, the Fabry-Perot and TIR enhancements will differ for the different grating geometries. It has previously been demonstrated that these other mechanisms play a substantial role in the enhancement of the devices. The triangular grating has a lower average height than the square and sinusoidal gratings and its shape may therefore lead to a beneficial balance between the Fabry Perot, TIR, and surface plasmon modes. The square grating, which has a step change in height, has clearly smaller and more clearly defined regions of enhancement. The height of this grating may therefore need to be tuned more finely than the triangular and sinusoidal gratings in order to achieve optimal practical devices.

4.5 Additional benefits

There may be additional benefits from the inclusion of the grating, aside from the optical effects detailed above, such as enhanced charge extraction. This is likely to be increased but a full analysis is beyond the scope of this thesis. Here, however, is a brief discussion of some of the effects that may influence the charge extraction. Firstly, the incorporation of a grating leads to an increase in the electrode area which may improve charge extraction, due to the reduction in the average distance to the electrode in the photoactive region. If the same absorption is obtained but with an increased electrode area, the increase in charge extraction may in itself be beneficial. This has implications for the choice of grating geometry. A triangular grating increases the electrode area by a factor of $\sqrt{\mathrm{P^2FF^2} + 4\mathrm{H^2}}$. In comparison, a rectangular grating increases the electrode area by a periodicity and fill factor-independent 2H. The difference between these two enhancements is shown in Figure 4.14. It is apparent that the rectangular grating leads to a far greater increase in the electrode area. At an optimal grating height of 80 nm, for example, the rectangular grating increases the electrode area 4.5 times more than the triangular

grating. When comparing triangular and rectangular gratings, the difference in electrode area may be a significant factor that has to be taken into account along with any difference in optical properties.

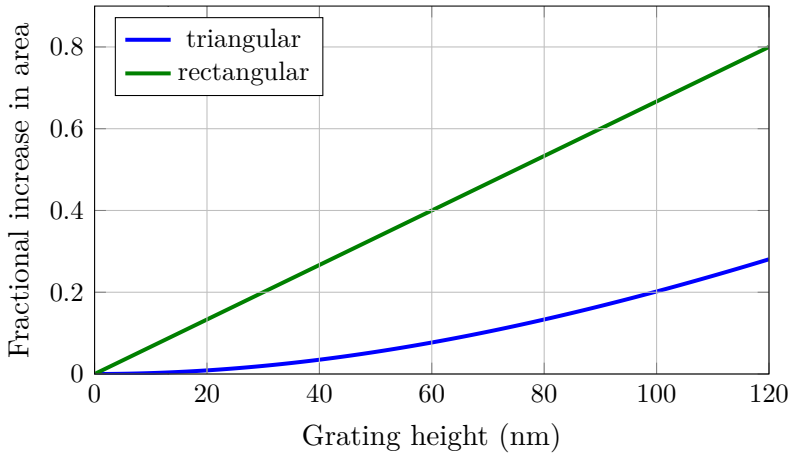

Figure 4.14 Fractional increase in electrode area for a triangular and rectangular grating.

In addition, the presence of the structured electrode will influence the electric fields present within the electric device. The field strength is a function of the distance between the electrodes. This will be modified by the introduction of the grating, and the increased field may lead to altered extraction, as the charges move under the electric drift and diffusion equations. Furthermore, absorption and therefore charge generation within the active layer will be non-uniform due to the grating. This localisation of charge generation will also affect the overall rate of charge extraction. A model taking into account these factors is again beyond the scope of this thesis, but works such as Koster *et al.*[102] describe the methods that are typically employed.

4.6 Fabrication considerations

Having compared idealised grating geometries, it is now important to consider the practical fabrication of such structures. The rectangular grating is a vertical structure,

which would therefore benefit from fabrication via lithographic techniques. The gratings in question have a short period, and therefore require high resolution, and a high aspect ratio. Techniques such as electron-beam lithography are therefore most suited to these structures. With respect to a triangular grating, it may be difficult to produce a sharp triangular grating using conventional techniques. It is far more feasible to construct a large area sinusoidal grating using techniques such as laser beam interference. In this technique, interfering laser beams are used to cure a polymer, which therefore results in a sinusoidal pattern. This is clearly less defined than the triangular structures so far presented. In addition, other techniques might lead to a blunting of the triangle.

Simulations were therefore run in which the tip and trough of the triangular grating was blunted in order to assess whether this would have a strong effect on the absorption current. The rounding of the triangular features was achieved by employing a circle of a fixed radius such that it just touched the sides of the triangle. For a circle with radius r, this occurs at a position y above the triangle tip given by the following, where H and W are the height of the triangle respectively:

$$y = r\sqrt{\frac{2H}{W}^2 + 1} \tag{4.3}$$

The radius of the circle was varied in order to vary the amount of blunting of the triangle. The simulation geometry, along with the absorption currents obtained, are shown in Figure 4.15. There is a very slight increase in absorption current as the triangle is blunted. This is likely to be due to the increase in available active material as the triangle becomes more blunt. The reason for this insensitivity to the grating sharpness is probably that the mechanisms of enhancement identified in Section 3.6 are primarily dependent on the period of the grating, although the grating shape will have some effect. This is a welcome result for device fabrication as it shows that

a sharp triangle, which would be experimentally difficult to achieve, is not required.

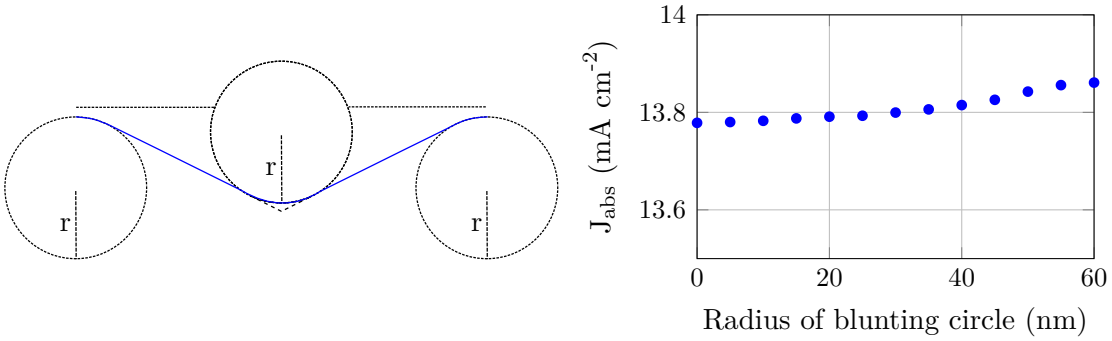

(a) Blunted triangle schematic (b) J_{abs} for a silver grating

Figure 4.15 Schematic of the grating geometry, along with a graph of absorption current as a function of the radius of the blunting circle (r).

Appreciable absorption enhancements have been demonstrated using both a silver and aluminium electrode. The value of aluminium as a suitable metal to excite surface plasmons in solar cells has not been focussed on in the literature. In both the Abass *et al.* [1] and the Sefunc *et al.* [2] papers, for example, silver was employed for the electrode. This is perhaps because the majority of work employing nanoparticles has been performed using silver due to the beneficial position of its surface plasmon resonance, as calculated using Mie theory. It was perhaps assumed that aluminium would therefore have little value as a grating too, but my results demonstrate otherwise. This is promising for practical devices, for which aluminium may be a better choice due to its better matching work function for charge extraction, and reduced cost.

At this point, it is interesting to compare the results from these simulations to previous experimental work. Experimentally, enhancements of 15% have been observed by Na *et al.* [67], using a silver sinusoidal grating. The planar devices are not previously optimised in this paper, so the enhancements observed are difficult to reconcile with the simulations in this thesis. In addition, the simulations do not take into account charge extraction effects which would be present in experimental devices. In the case

of rectangular gratings, a greater enhancement of 17.5% has been observed by Li *et al.* [70] using a silver grating. It would be interesting to see the comparative effect of an aluminium grating on these devices.

4.7 2D gratings

The 1D gratings described so far have a polarisation dependence. This is because the surface plasmon mode cannot be excited when the incident electric field is aligned parallel to the grating. In this configuration, the grating will not provide additional in-plane momentum to couple the light into the surface plasmon mode. This effect is demonstrated in Figure 4.16 where the surface plasmon peak at long wavelengths disappears under TM illumination.

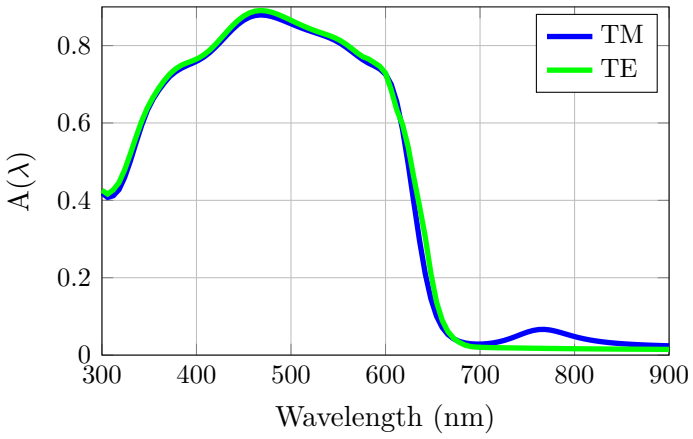

Figure 4.16 Absorption spectrum under uniform TM and TE polarised light, for a silver grating with periodicity 400 nm.

In order to mitigate this problem, a 2D grating could potentially be used, sometimes referred to as a bi-periodic grating. In this case, features are fabricated such that there is a periodically repeating shape in two orthogonal directions. Motivated by the optimal enhancements from a triangular grating, a 2D grating comprising square-bottomed pyramids was therefore simulated using full 3D calculations. The

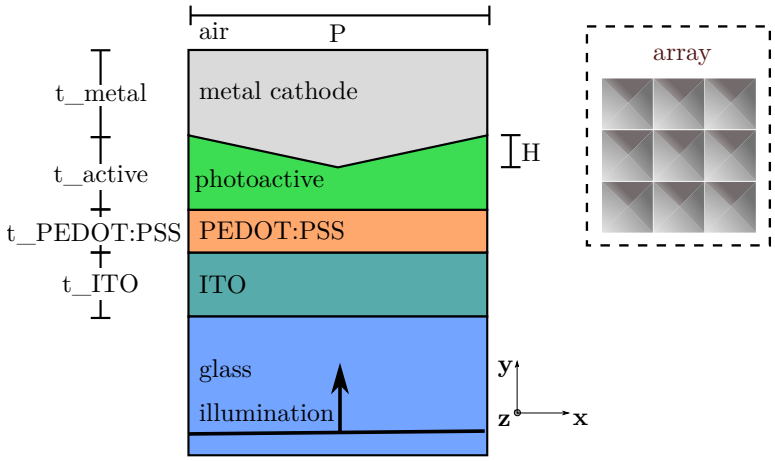

Figure 4.17 Schematic of a 2D triangular grating. The array consists of square-bottomed pyramids and is shown inset.

same periodicity was employed in both orthogonal directions. The grating features are illustrated schematically in Figure 4.17. Such a grating could be fabricated with similar lithographic methods as previously described, such as FIB or e-beam lithography. The latter method presents some challenges for grating shapes such as the square-bottom pyramids described, however, due to the sloping structures required.

In order to get an understanding of the enhancement due to a 2D grating, simulations were performed in which the period of the grating was varied. These simulations require increased computational time and increased the memory requirements compared to the 2D simulations performed previously. It was possible to make use of symmetry in a similar way to the 2D simulations, but the computational requirements were still relatively large. The results of sweeping the periodicity of a 2D grating from 180 nm to 550 nm are shown in Figure 4.18.

The introduction of a 2D grating led to an additional mode most evident starting at a periodicity of 600 nm and wavelength of 600 nm and extending upwards in wavelength towards longer periods. This is most likely due an additional momentum component

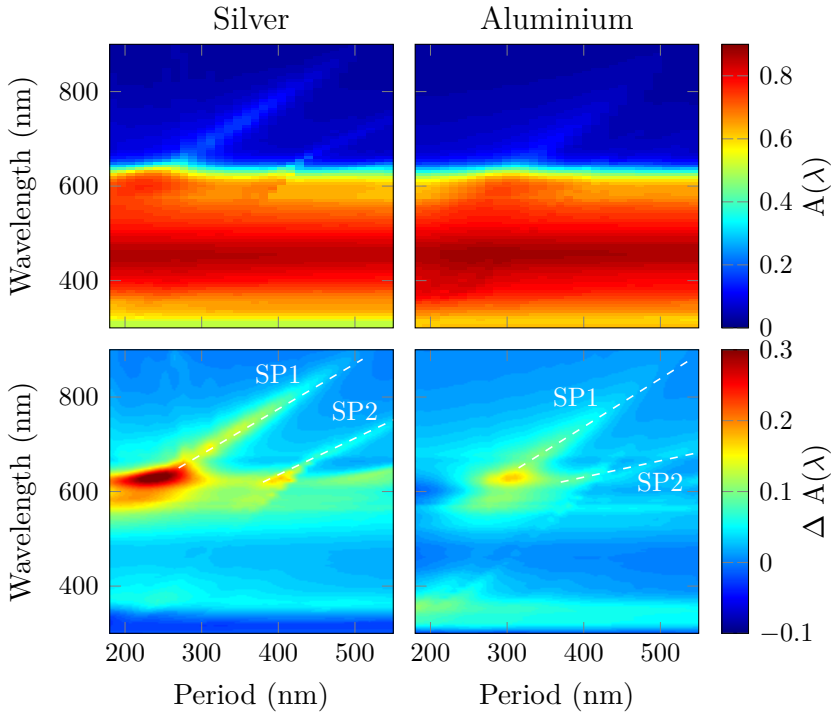

Figure 4.18 Plot of $A(\lambda)$, the fraction of incident photons absorbed by the active layer (a), and the absolute increase of A(λ), $\Delta A(\lambda)$, compared to a planar device (b), for a cell with active layer thickness 120 nm incorporating a 2D triangular pyramid grating with height 70 nm, with a silver (left column) and aluminium (right column) electrode under TM illumination. The surface plasmon modes are labelled with dashed lines as a guide for the eye. The mode labelled SP1 corresponds to the mode that is also present in devices with 1D gratings and the mode labelled SP2 corresponds to the additional mode introduced by the 2D grating.

provided by a 2D grating. This additional momentum is equal to the magnitude of the reciprocal lattice vector of the grating. Previously, the additional in-plane momentum took the form $k_g = \frac{2\pi}{P}m$, where m is an integer index labelling the mode. In the case of the 2D grating, the in-plane momentum includes a contribution from two orthogonal directions. The momentum component therefore requires an additional index and can be labelled as $k_{g(m,n)}$, where m and n are integers indexes in the two directions. The three lowest order modes would have indices of (1,0), (0,1) and (1,1). The first two are degenerate in the case of equal periodicities in the two orthogonal grating directions, with $k_g = \frac{2\pi}{P}$. The (1,1) mode will provide a larger momentum of $k_g = \sqrt{2}\frac{2\pi}{P}$. This leads to an additional surface plasmon mode, which will occur at longer wavelengths than the first order mode.

Returning to Figure 4.18, the first order surface plasmon mode for the (1,1) grating vector is not visible as it would fall at long wavelengths just outside the absorption of the active layer. The additional feature observed is therefore due to a second order surface plasmon mode, which now falls in a useful region of the absorption spectrum of the photoactive polymer. This mode is somewhat weaker than the first order mode of the (1,0) and (0,1) grating vectors.

In addition, there is a faint shallower TIR mode visible, more evident for the aluminium electrode, starting at a wavelength of 300 nm and a periodicity of 300 nm and increasing in wavelength as the periodicity increases. This is again attributed to the additional (1,1) momentum component provided by the 2D grating. This will modify the TIR equation previously derived by a factor of $1/\sqrt{(2)}$ leading to the shallower additional TIR mode present.

Having ascertained these additional sources of enhancement, simulations were run in order to optimise the grating geometry, as before. Due to the computational demands of the 3D simulations, it was not practical to run the same breadth of

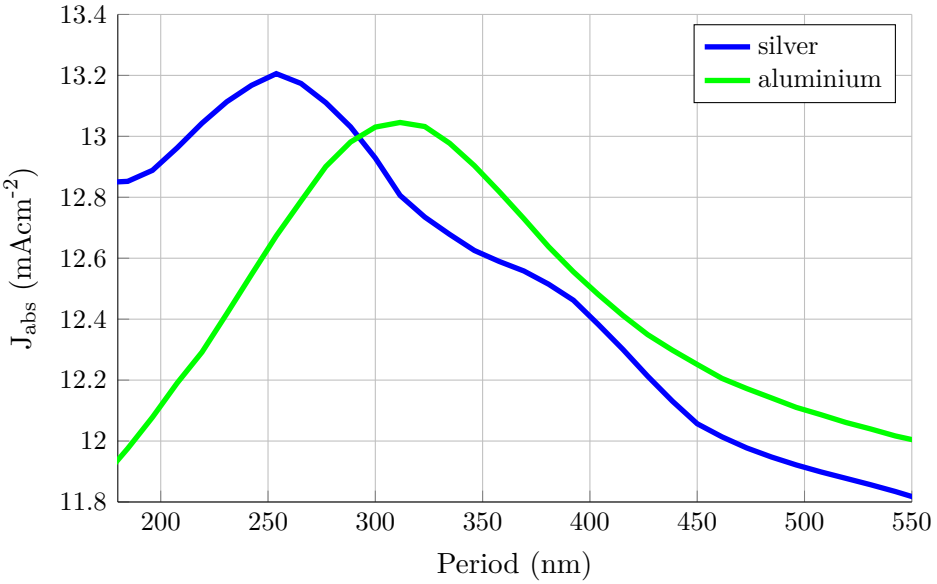

Figure 4.19 Absorption current as a function of grating period for a 2D triangular grating with height 70 nm and active layer thickness of 120 nm.

parameter sweep as before. A sweep was therefore run varying the grating period but maintaining a fixed grating height of 70 nm and focussing only on a single active layer thickness of 120 nm. These were selected as they gave good enhancements for a 1D grating. The thickness of each of the other layers were kept the same as for the 1D grating simulations. The absorption current J_{abs} achieved as a function of grating period are shown in Figure 4.19.

The maximal absorption current achieved is 13.21 mAcm^{-2} at a period of 250 nm. In addition, a second smaller peak is apparent at a grating period of around 370 nm. This arises from the additional surface plasmon mode identified previously in Figure 4.18. It is interesting to note that longer periods do not lead to optimal devices and that there is a decline in absorption as grating period increases. This suggests that the contribution from this surface plasmon mode is not significant enough to warrant the losses due to the introduction of the grating at longer wavelengths.

Recent work by Fallahpour *et al.* compared planar devices with devices incorporating

2D rectangular gratings [103]. They also incorporated a simple charge extraction model to account for the effect that this would have on real devices. This work was achieved using a finite element modelling technique, in comparison to the FDTD technique used here. They looked only at an aluminium grating, which is the common choice for practical devices. In addition, they looked at a rectangular array, rather than the triangular pyramids studied here. They directly compared with planar devices of the same active layer thickness. As demonstrated in Section 3.6, that neglects the alteration of multilayer interface by the introduction of the grating. This therefore leads to misrepresentation of the true enhancements, and leads to an exaggeration of the benefits provided by the grating. They did, however, identify a comparable range of grating periods for which optimal enhancements take place, helping to corroborate the current work.

Comparing the 1D and 2D grating geometries, the optimal absorption current demonstrated for a 2D grating is slightly lower than the 1D case. This may be due to the fact that the 2D grating has not been fully optimised with respect to the height of the grating and active layer thickness, although these are likely to be fairly similar. As noted previously, the 2D grating introduces new modes not identified in the 1D case. These seem not to provide significant further enhancements, as the absorption current is not significantly higher than the 1D case. It therefore appears that results from 1D gratings can be used as useful guides to inform the design of 2D gratings. The significant benefit of the 2D grating therefore appears to be the periodicity-independent enhancements that it leads to. In real devices, this will lead to a significant advantage over 1D gratings.

4.8 Chapter summary

I have employed theoretical band structure plots to confirm and elucidate the mechanisms of enhancement, focussing on the surface plasmon mode. This led to a summary plot demonstrating the dependence of the surface plasmon mode wavelength on grating period. The grating periods that provide a surface plasmon enhancement are somewhat limited due to the wavelength-dependent permittivity of the active material involved. This plot therefore provides a useful reference for a standard P3HT:PCBM blend and demonstrates a method that could be applied to other photoactive materials to aid the design process.

I have performed an optimisation of the overall absorption current J_{abs} within the devices. This absorption current is a strong function of the grating parameters, and sweeps of these parameters reveal optimum regions for strong absorption. These regions show broad tolerances to the grating height and period, and reduce the sensitivity of the solar cell devices to active layer thickness when compared to planar devices. These results have important implications for fabricating real devices incorporating such structures.

The optimum absorption currents achievable with the gratings studied are $13.86\,\mathrm{mAcm^{-2}}$ (silver) and $13.13\,\mathrm{mAcm^{-2}}$ (aluminium) for a triangular grating, and $13.44\,\mathrm{mAcm^{-2}}$ (silver) and $12.70\,\mathrm{mAcm^{-2}}$ (aluminium) for a rectangular grating, and $13.62\,\mathrm{mAcm^{-2}}$ (silver) and $12.96\,\mathrm{mAcm^{-2}}$ (aluminium) for a sinusoidal grating. These compare to currents of around $12.6\,\mathrm{mAcm^{-2}}$ for comparable planar control devices. The sensitivity of the absorption currents to the grating parameters is more strongly defined in the case of the rectangular grating than the triangular or sinusoidal grating. Ease of fabrication means that a triangular or sinusoidal grating may also be preferable. Blunting of the triangular grating does not have a marked impact on

the achievable absorption currents, which is promising for practical devices, where fabrication methods may not allow sharp features. The grating structures provide enhancements that have a good insensitivity to the angle of incidence of the illumination. This is promising for practical devices, where the angle of incidence may vary without expensive tracking equipment. Finally, I have demonstrated the potential of 2D gratings, which mitigate the polarisation-dependence inherent with 1D gratings. Sampling the parameter space, I have identified enhancements of up to 22% compared to planar devices. Having identified that gratings can make a substantial improvement to the absorption within these devices, I will investigate factors that affect the application of such structured devices in the real world.

CHAPTER 5

Considerations for practical devices

5.1 Introduction

In this chapter, I discuss factors that affect the practical realisation of the devices so far described. The application of solar cells in the real world leads to additional challenges and considerations not so far presented. A major factor is that the illumination conditions are frequently different from the ideal normally incident spectrum so far described. The illumination conditions vary significantly depending on factors such as geographical location, time of day, season, and local weather conditions. Although normally incident light has been assumed so far, in reality light will therefore be incident from a range of angles. In addition, its spectrum will not be

the assumed AM1.5G. In this chapter, I present simulations and calculations to help understand how grating-enhanced devices will perform under varying illumination conditions.

In addition, the active photovoltaic devices are deposited on a substrate, which has so far been assumed to be glass. The choice of substrate will influence the optical properties of the final devices, however, and is largely dictated by the proposed usage of the device. I compare the use of glass and PET, which can be used to fabricate flexible devices, and discuss how the choice of substrate influences the optical efficiency of devices incorporating gratings.

The field of thin-film solar cells is rapidly evolving and the range of materials employed is ever widening. The different choice of materials will influence the optical properties of the device. This effect is compounded, because different materials may require altered layer structures, with a corresponding influence on the optical properties. This thesis has focussed so far on P3HT:PCBM solar cells as a relative stable benchmark. In this chapter, I present data to illustrate how alternative photo-active materials will influence the enhancements that may be achieved using gratings. Finally, I explore the effect of additional buffer layers in the device, which are frequently employed to enhance the charge extraction properties of thin film solar devices.

5.2 Angled illumination

In the real world, the illumination angle will not always be perpendicular to the solar device. In fact, in these featured devices normal incidence may not even be optimal. This is because increasing the angle of incidence effectively supplies additional in-plane momentum which will enable coupling to surface plasmon modes and TIR

at different wavelengths. In addition, the optical path length through the device is increased at steeper angles. This must balanced against the decreased average irradiation, however, that occurs at oblique incidence.

For this reason, simulations were performed to investigate the effect of altering the angle of incidence on optimised plasmonic devices. In order to simulate periodic structures with angled source injection, Bloch boundary conditions were employed using a module within the FDTD software. If the structures within the simulation region are periodic with a lattice vector $\mathbf{R}$, and the initial incident source distribution also shares this periodicity, then any field A can be written as in Equation (5.1) [104]:

$$A(\mathbf{r} + \mathbf{R}) = A(x) \exp(i\mathbf{k} \cdot \mathbf{R}). \tag{5.1}$$

The field amplitude is therefore periodic, but there is a phase shift dictated by the projection of $\mathbf{k}$ onto $\mathbf{R}$ given by $\mathbf{k} \cdot \mathbf{R}$, now referred to as the in-plane momentum k_x. The total field within the simulation region, having undergone any scattering or absorption, is also Bloch periodic, such that this momentum is conserved. In order to enforce this, the Bloch condition above is applied to the fields at the boundaries of the simulation region. In the case of the current simulations, the simulation region is periodic in the x direction, with a periodicity given by the grating. Bloch boundary conditions were therefore applied at the lateral simulation boundaries. PML boundaries were maintained at the top and bottom of the simulation region to absorb any radiation leaving the simulation region.

A schematic of the simulation geometry is given in Figure 5.1. As the simulations are broadband, this presents an additional challenge for FDTD simulations. This is due to the wavelength-dependence of the in-plane k-vector k_x given in the following

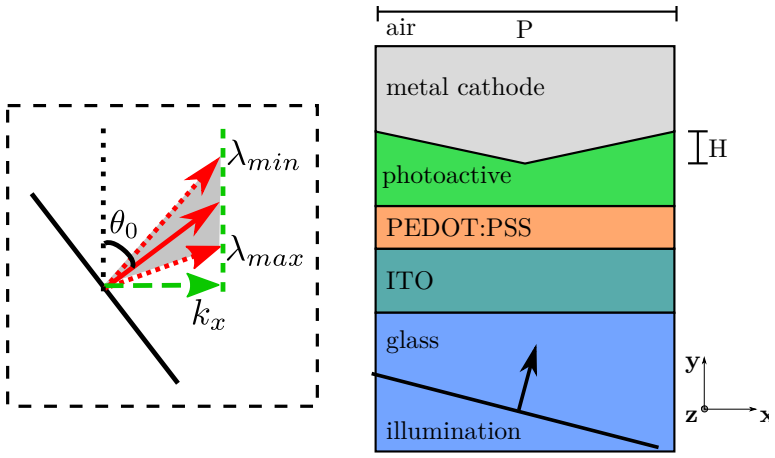

Figure 5.1 Schematic of the simulation geometry for simulations with angled illumination. The wavelength-dependence of the source injection angle is illustrated within the inset, where the nominal injection angle for the simulations is labelled θ_0.

equation, where λ is the incident wavelength and θ is the injection angle:

$$k_x = \frac{2\pi}{\lambda}\sin(\theta) \tag{5.2}$$

When employing Bloch boundary conditions for a given injection angle, periodicity is achieved by fixing k_x. This means that the effective source angle changes as a function of wavelength. In a broadband simulation, a wide range of wavelengths are present and each will have a different effective source angle. This range of angles is illustrated in the inset of Figure 5.1. It is, however, possible for any simulation to interpolate the results back to a common set of angles θ_0, by rearranging 5.2 to give the following, where $\theta_0\lambda$ is the common injection angle as a function of wavelength λ, λ_{sim} is the central simulation wavelength, θ_{sim} is the nominal source injection angle:

$$\theta_0(\lambda) = \sin^{-1}(\frac{\lambda}{\lambda_{sim}}\sin(\theta_{sim})) \tag{5.3}$$

At each imposed value of k_x, there will be a number of wavelengths whose effective source angle will be greater than 90°. In order to mitigate this problem, the broadband simulation can be split into narrower wavelength regions within which no angle is greater than 90°. The final results are obtained by grouping the data from these individual simulations.

A further challenge that arises with angled simulations is that reflections from the PML absorbing boundaries become more prominent at steeper angles, as discussed in Section 2.5. This in turn can lead to diverging simulations, as light is effectively trapped within the simulation region. This situation is not physical and leads to erroneous results or simulations that do not converge. It was therefore necessary to optimise the parameters of the PML boundaries to ensure that this did not occur.

In practical devices, there will also be reflection at the air/substrate interface which will depend on the angle of incidence. The amount of reflection and transmission is given by the Fresnel equations, as discussed in Section 2.4. In addition, light will be refracted as it passes across the interface, with the angle dictated by Snell's Law, as given in Equation (5.4), where n_1 and n_2 are the refractive indices in media 1 and 2, respectively, and θ_1 and θ_2 are the angles to the normal. As the substrate will have a higher refractive index, the light will be refracted towards the normal, reducing the angle of incidence at the substrate/ITO interface. This effectively reduces the maximum range of incidence on the active device to within ∼42°.

$$\sin(\theta_2) = \frac{n_1}{n_2}\sin(\theta_1) \tag{5.4}$$

A further consideration when the angle of incidence is varied is that the average irradiation will drop as the angle is increased and is proportional to $\cos(\theta)$, where θ is the angle of incidence. The absorption currents simulated must therefore be

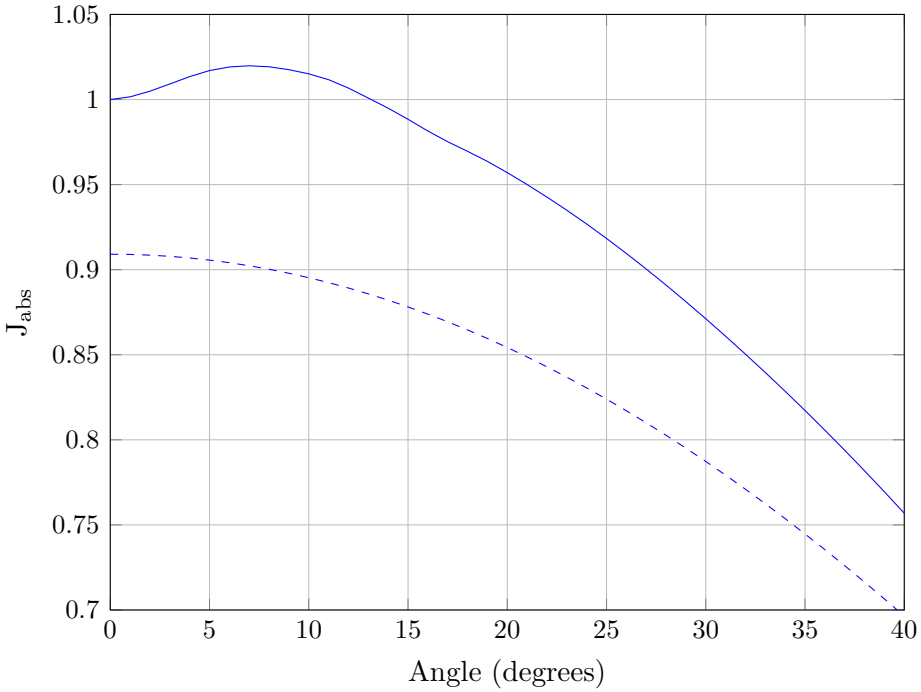

Figure 5.2 Absorption current as a function of angle of incidence for a silver triangular grating with periodicity 350 nm, normalised to the absorption current at normal incidence. The absorption current for a planar device is shown for comparison (dashed line) and has been normalised to the absorption current of the featured device at normal incidence.

reduced by the same factor to take this into account.

A number of simulations were perfomed with different wavelength ranges and k_x vectors. The results processed such that the absorption as a function of wavelength was interpolated back to a common set of angles, due to the wavelength dependence of k_x discussed above. The spectrum is assumed to be the same across all angles of incidence and the irradiation is reduced by a factor of $\cos(\theta)$ as discussed above. Whilst this is a simplification of the complex relationship that exists between angle of incidence and the incident power and spectrum, a more detailed analysis is beyond the scope of this thesis. More detailed discussions of this can be found elsewhere [105, 106]. The resulting spectra as a function of wavelength are shown in Figure 5.3.

From Figure 5.2, there is a small increase in absorption current up to around 10°.

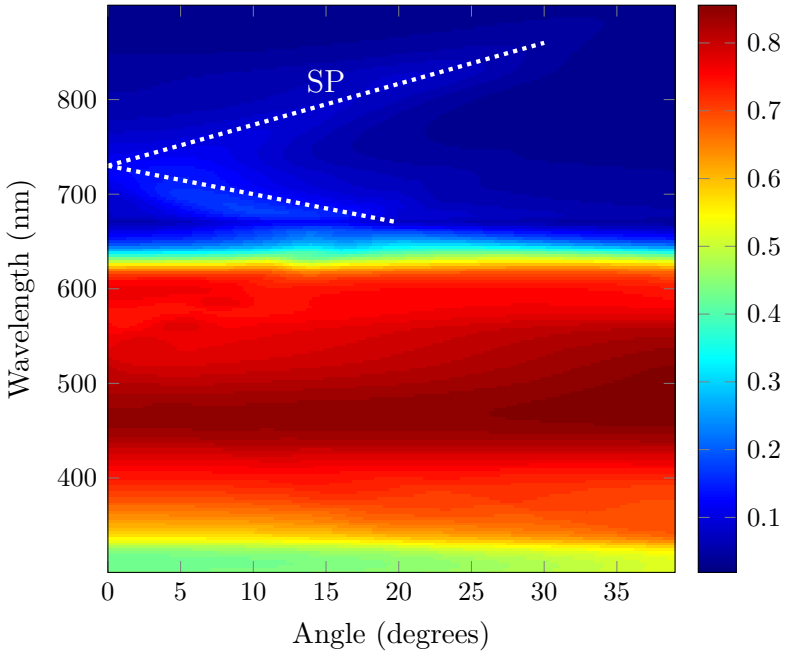

Figure 5.3 Normalised absorption (A(λ)) as a function of angle for a device incorporating a silver grating with a periodicity of 350 nm, demonstrating the splitting of the surface plasmon mode with angle. The surface plasmon mode is labelled with lines marked SP as a guide for the eye.

This is due to the angular dependence of the surface plasmon wavelength, whereby a small shift in angle results in a small shift in the surface plasmon mode. Returning to Figure 4.2, the surface plasmon mode should split into two branches as the angle is increased from the normal. This is reflected in the absorption spectrum shown in Figure 5.3. The splitting may contribute to the small increase at off-normal incidence. In addition, increasing the angle of incidence increases the average path length though the device which should increase the absorption current. This is balanced by the reduction in average irradiance as the angle of incidence is increased. The net result is that the absorption current begins to decay steeply from around 10°. The absorption currents are, however, moderately insensitive to changes in angle up to this point. This insensitivity is corroborated in the work by Abass *et al.* [1].

In practical devices, the angle of incidence will vary during during the day, so some robustness to changes in angle is advantageous. Reductions due to these changes in

angle can be mitigated by employing tracking systems to maintain an optimum angle to the sun [107]. This adds significant cost to the solar panels, however, and may not be economical for the relatively low efficiency organic solar cells. Furthermore, the diffuse component of solar illumination occurs from many different angles, as discussed in Section 5.3.

5.3 Illumination conditions

Up until this point, a standard solar spectrum (AM1.5G) has been assumed, as is standard within the literature. This spectrum incorporates both direct and diffuse components. The different AM1.5 spectra including the diffuse spectrum, calculated from the difference between AM1.5D and AM15G, are illustrated in Figure 5.4. In addition to the spectral differences, the direct component of light falls in a narrow range of angles around the normal, whereas the diffuse component arises from scattering across the sky. The diffuse component therefore appears to arrive from a wide range of angles.

In addition, the AM1.5G spectrum assumes a solar zenith angle, the angle between the vertical directly overhead and the sun's centre, of 48.2°. At angles away from this, the path length through the atmosphere varies, and the wavelength-dependent scattering leads to a variable spectrum. Local effects such as weather, and pollution will also affect the incident solar spectrum [108]. The latitude will influence both the zenith angle during the day and the length of the days in a seasonal fashion and highly influence the solar intensity. The incident solar spectrum is therefore highly dependent on local conditions, as well as the angle of incidence on the panel, which will vary during the day without the use of solar-tracking systems.

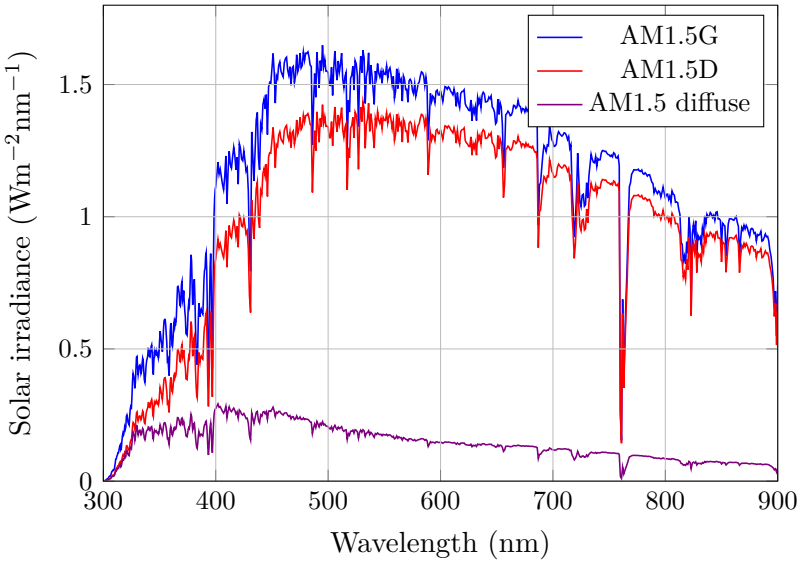

Figure 5.4 Direct, diffuse, and global tilt AM1.5 spectra, as labelled.

In order to simplify this complexity and make some reasonable comparisons, the response under AM1.5D and AM1.5 diffuse radiation was compared. This enables comparison between direct illumination at near-normal incidence and broad diffuse radiation which is incident at many angles. In some countries, such as the UK, a large component of the incident solar radiation is diffuse, varying strongly by location and clearness index $\bar{k_t}$, the ratio of local irradiation to the extraterrestrial radiation AM0. For example, at a k_t of 0.2 and 0.4, the diffuse ratio in London is 70% and 58%, respectively, whilst in Stornoway it is 80% and 70% [109].

The absorption current of a typical device incorporating a triangular grating was therefore compared under AM1.5D radiation and the diffuse component of AM1.5G, and is shown in Figure 5.5 as a function of grating period for a 1D triangular silver grating. Typical absorption spectra under the two types of irradiation are shown in Figure 5.6.

It can be seen that the typical absorption under diffuse light is significantly lower than that under direct illumination. Looking at the overall absorption current J_{abs} as a function of grating period, absorption currents are around 13.6 mAcm^{-2}

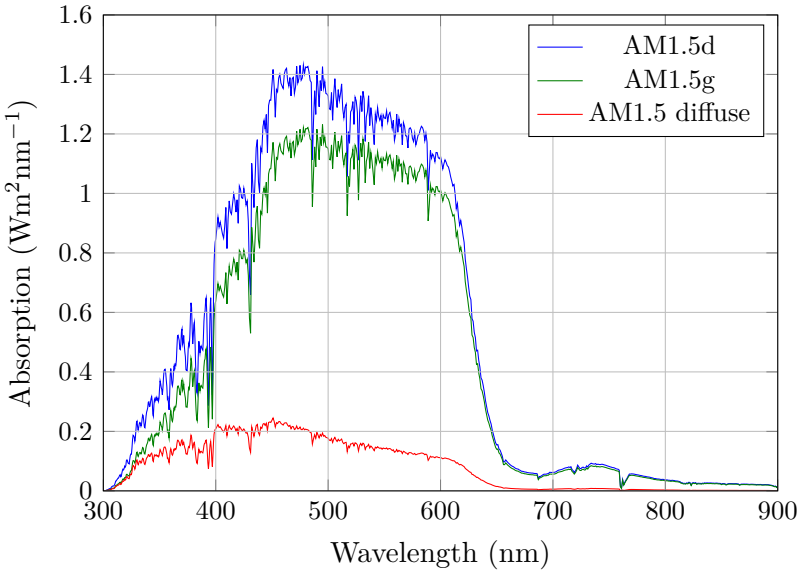

Figure 5.5 Typical absorption spectrum under direct and diffuse AM1.5 illumination, as labelled.

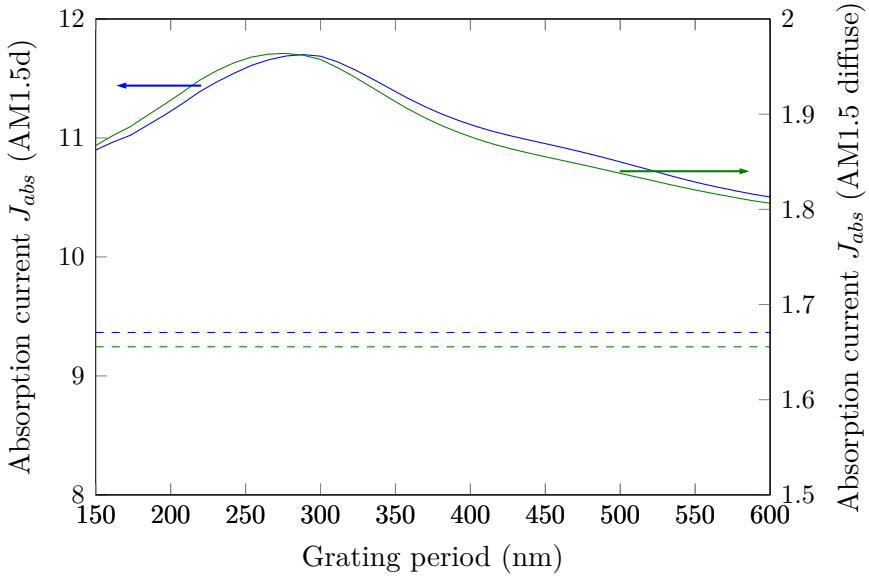

Figure 5.6 Absorption current J_{abs} as a function of grating period under direct and diffuse AM1.5 illumination, as labelled. The absorption currents for planar control devices are indicated by dashed lines, for comparison.

compared to 1.95 $\mathrm{mAcm^{-2}}$ for direct and diffuse illumination, respectively. Notably, the enhancements are very similar, however, although there is a small shift to shorter grating periods for the optimum enhancement under diffuse illumination. This is due to the shorter wavelength bias of the diffuse solar spectrum.

As discussed previously, a significant proportion of incident light in the UK is diffuse. From the preceeding discussion, it is evident that plasmonic devices of the type discussed in this thesis will have a comparable effect under diffuse light conditions as under direct illumination and therefore provide a worthwhile benefit in both cases.

Finally, it is worthwhile noting that diffuse radiation is incident from a wider range of angles than direct illumination. The effects of angle of incidence discussed in Section 5.2 will therefore come into play for a significant proportion of the incident diffuse irradiation.

5.4 Substrate

So far, a glass substrate has been assumed for the fabricated devices. One of the benefits of organic solar cells is that the thin layers permit the fabrication of flexible devices. In this case the substrate is typically a plastic, such as polyethylene terephthalate (PET). In order to achieve good flexibility, the relatively rigid ITO front contact must be replaced with an alternative. One possible alternative is the use of a silver grid or silver nanowires on PEDOT:PSS [110, 111].

This alters the optical effects in two ways. Firstly, the incident light hitting the substrate will have differing reflection/transmission coefficients for the different materials. PET has a higher refractive index than glass and the refractive index is more highly wavelength-dependent, as shown in Figure 5.7, where the refractive

index data has been taken from literature sources [88, 112]. PET has a slight intrinsic birefringence that remains due to molecular alignment during manufacture but this has been neglected as it is relatively small for such thin films [113].

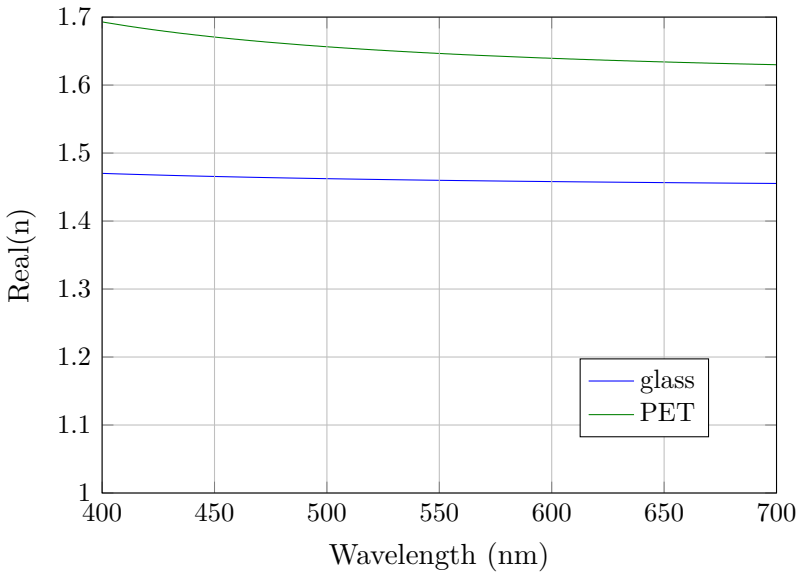

Figure 5.7 Refractive index of glass and PET substrates, as labelled, as a function of wavelength.

In the first instance the higher refractive index will lead to different reflection coefficients at the air/substrate interface. This is calculated using the Fresnel equations and shown in Figure 5.8. The glass substrate leads to a reflection coefficient of 4% at normal incidence compared to 6% for the PET. The PET substrate therefore leads to a slight reduction in available energy of a similar magnitude. The reflection coefficients for PET are also higher than glass at off-normal angles of incidence. The Brewster angle, at which TM reflection falls to zero, occurs at a slightly higher angle for PET at 59° rather than 56°. Extending above this angle, large reflections from the substrate occur for both polarisations leading to greatly reduced photocurrent.

In addition, when the PET substrate is employed, a silver grid will typically be employed without an ITO layer. As identified previously, the TIR does not depend on the refractive index of the layer in contact with the substrate, so the TIR mode

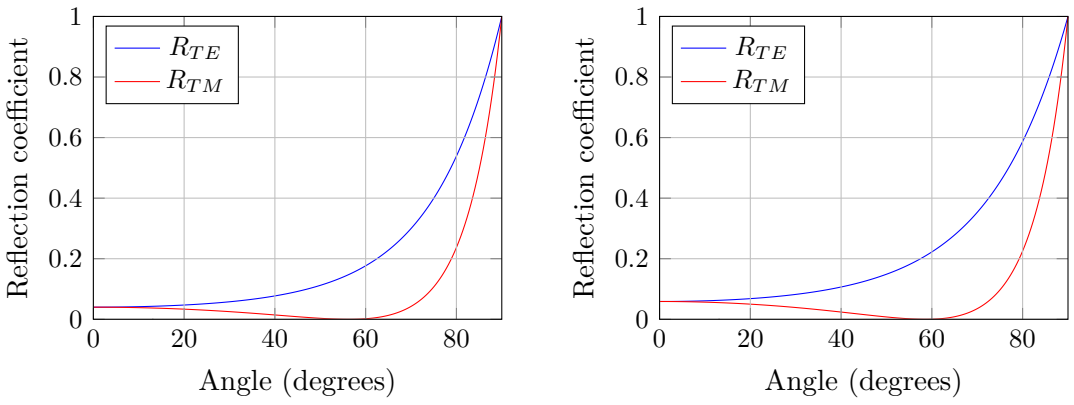

(a) Glass (b) PET

Figure 5.8 Reflection coefficients at the air/substrate interface for glass and PET substrates, for TE-polarised and TM-polarised light, as labelled.

should still be present and provide enhancements to these devices.

Finally, the higher index of the PET layer will lead to increased refraction towards the normal under angled illumination. This will affect the response of the devices as light will be incident on the active device layers at a reduced angle. This may be beneficial at steep angles of incidence, as the featured devices perform worse at these angles, as discussed in Section 5.2.

5.5 Material choices

The field of photovoltaics is evolving rapidly and new materials are in constant development. This work has focussed on P3HT:PCBM as a stable reference material, but active material blends with higher conversion efficiencies have been demonstrated, such as PCDTBT:PCBM and PTB7:$PC_{71}BM$. These materials present different refractive index environments for any grating structures employed. This may affect the enhancement mechanisms previously identified including the surface plasmon resonance conditions, the angle of grating scattering and hence the TIR modes,

and the multilayer interference. The refractive index of the materials are shown in Figure 5.9, with the refractive index data taken from various experimental sources [6, 114, 115]. The PTB7 and PCDTBT blends are seen to have a higher real refractive index across the wavelength spectrum, and show stronger absorption at longer wavelengths due to the larger imaginary component. These longer wavelength regions are ideal for enhancement by the surface plasmon mode.

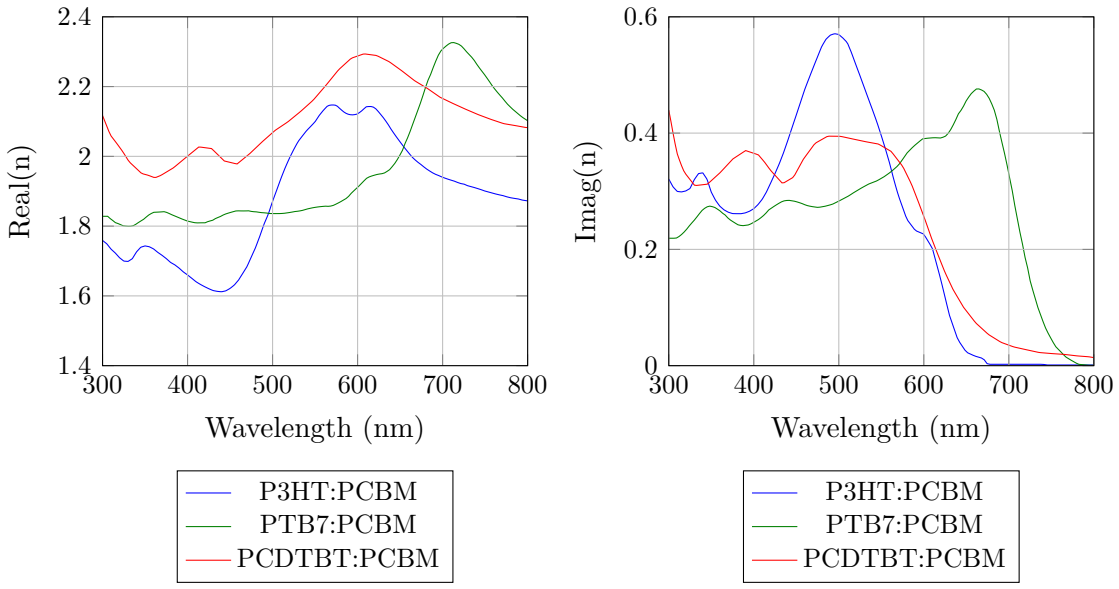

Figure 5.9 Refractive indices for a number of photoactive material blends, as labelled. Data are taken from various experimental sources [6, 114, 115].

The different active layer materials will lead to different dielectric environments for the excitation of surface plasmons at the rear electrode. In order to get a sense for the likely effects of this, Figure 5.10 presents the surface plasmon excitation wavelength for a number of material combinations. These data were calculated using custom Python code. This first calculates the dispersion using the surface plasmon condition of Equation (2.18) then applies band-folding arguments, as in Section 4.3, to calculate the crossings with $k_x = 0$. These crossings are identified by the code, and those that correspond to first order surface plasmon excitation are retained.

The different active materials lead to shifts in the surface plasmon position, although

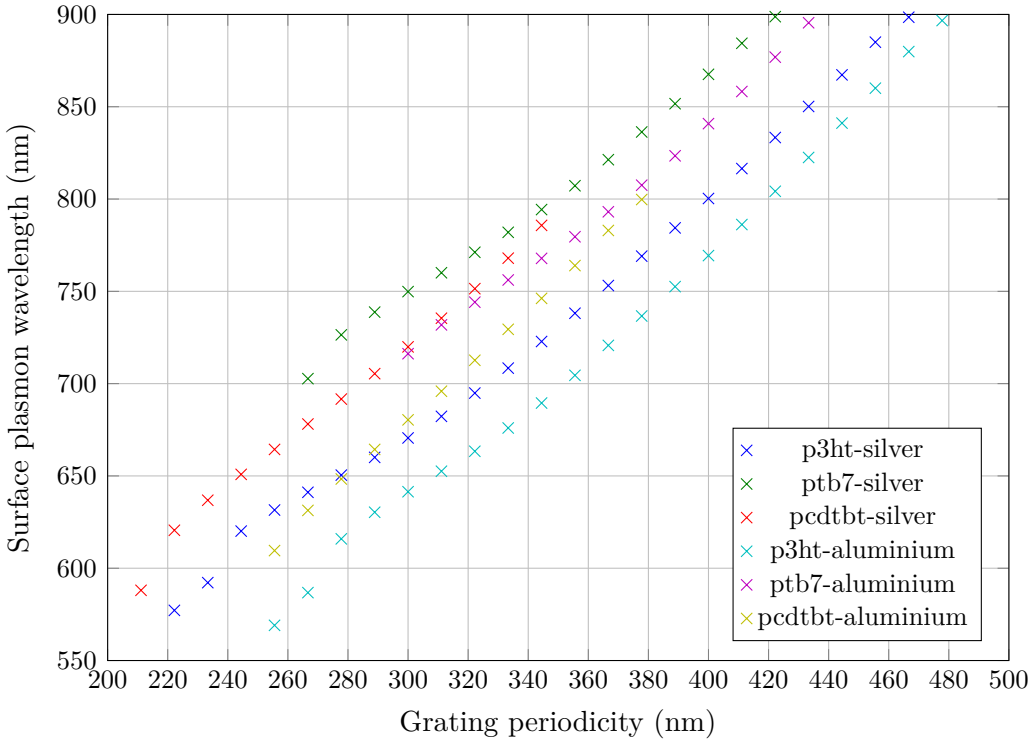

Figure 5.10 Surface plasmon wavelength for a number of material combinations.

these do not differ by more than 100 to 150 nm at a particular grating period. For all the active materials, the surface plasmon arising from a silver grating occurs at a shorter periodicity than for the aluminium grating. At a particular surface plasmon wavelength, the P3HT blend requires the longest grating, and both the PCDTBT and PTB7 require shorter gratings, with the PTB7 requiring the shortest. This may have implications for the fabrication of working devices, as generally shorter gratings are harder to fabricate. However, this is balanced against the fact that the PCDTBT and PTB7 display stronger absorption at longer wavelengths than the P3HT blend, so surface plasmon enhancement may be more beneficial at longer wavelengths. The range of grating periods that will lead to good optical enhancement are therefore likely to be similar for all these materials.

Considering now the total internal reflection demonstrated in Chapter 3, the choice of active material will not have a significant impact on this mode. Referring to

Equation (3.10), it can be seen that the refractive index of the active material is not significant. The TIR enhancement is therefore expected to persist regardless of the active material employed.

5.6 Device structure

In addition to the active layer material, overall device structures vary widely. Additional layers are often introduced into the devices, such as Ca, CS_2CO_3, TiO_2, or ZnO before the cathode to act as an electron transport buffer layer [116], or sometimes as an optical spacer layer [117, 118]. Similarly, PEDOT:PSS, In_2O_3, V_2O_5, and MoO_3 are employed as hole transport buffer layers. In addition, inverted device structures have been shown to produce high efficiency devices, whilst mitigating some of the disadvantages of organic solar cells in terms of air stability [119]. In this case, the role of the front and rear contacts as anode and cathode, respectively, is reversed. Buffer layers of ZnO and MoO_3 are frequently employed in this configuration.

These additional buffer layers will alter the optical properties of the device. To demonstrate the effect of a high index buffer layer, Figure 5.11 shows a typical absorption spectrum for a 350 nm silver triangular grating, incorporating a 40 nm buffer layer at the rear cathode compared to a device without one. A high index layer with a real refractive index of 3 was employed, to give a sense of the effect of high index materials such as ZnO.

The buffer layer can be seen to have two effects. The first is that the surface plasmon mode is shifted to longer wavelengths, as expected given the increase in the dielectric environment for surface plasmon excitation. In addition, the interference within the multilayer structure has been severely modified, leading to sharp changes in

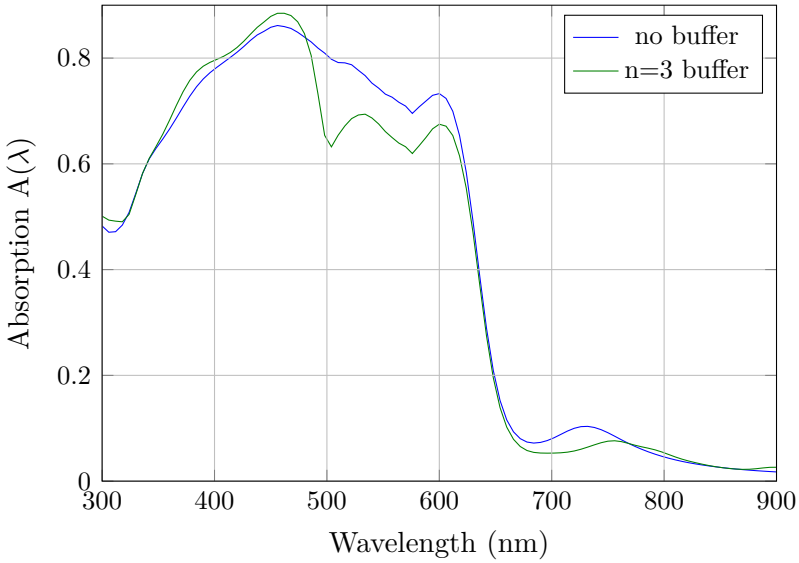

Figure 5.11 Typical absorption spectra of a device incorporating a 350 nm silver grating. Devices with a 40 nm buffer layer with a refractive index of 3 are compared to devices without a buffer layer.

the region of 500 to 640 nm. In the optical design of a specific device, the layer thicknesses should ideally be tuned to provide optimal multilayer interference, whilst maintaining the enhancements provided by the rear grating. Other structural changes will cause different optical effects and FDTD modelling of the form demonstrated provides a useful tool to evaluate these effects.

5.7 Chapter summary

In this chapter, I have investigated various aspects of the featured devices that influence their application in the real world. I explored the effect of varying the angle of incidence on the absorption spectra and identify splitting of the surface plasmon mode, as predicted from theory. Good overall absorption is also demonstrated up to around 15°, and there is, in fact, a small increase in absorption at small angles of incidence. This insensitivity to angle of incidence is important as this angle will vary during the day for practical devices.

I have explored the effect of illumination conditions on featured devices, specifically comparing direct and diffuse irradiation. I identified that although overall absorptions are significantly lower under diffuse radiation, the enhancements due to the grating are comparable in both cases, although there is a subtle shift to require longer gratings under diffuse illumination.

The effect of the substrate was addressed by comparing a PET and glass substrate. The substrate will introduce losses due to reflection at the air/substrate interface. This is increasingly significant at larger angles but even at small angles, reflection losses of 4% and 6%, for glass and PET, respectively, are demonstrated.

I then investigated the effect of employing different active layer materials on the devices. This will lead to significant differences in the multilayer interference. In addition, the surface plasmon mode will occur at different wavelengths, with P3HT leading to the shortest wavelengths, although the differences between the polymers are limited to around 100 to 150 nm. A shorter grating periodicity is therefore required for PTB7 and PCDTBT to achieve the same surface plasmon wavelength. This is, however, balanced against the requirement for enhancement at longer wavelengths for the latter materials. Finally, I briefly explored the effect of introducing a high index buffer layer into the devices. This significantly effects the multilayer interference, and leads to a shift in the surface plasmon wavelength.

Whilst it is difficult to provide an optimal cell design for all illumination conditions and device architectures, the work in this chapter demonstrates that grating structures provide valuable enhancements in most cases. Gratings provide enhancements that are relatively insensitive to angled illumination and provide enhancements under different illumination conditions. Different device structures will lead to subtle differences in interference and surface plasmon enhancement. Optimisations of the type demonstrated in Chapter 4 would enable informed optical design decisions

to be made to account for these differences. In the following chapter, I address steps towards the experimental fabrication of practical devices incorporating grating structures.

CHAPTER 6

Fabrication of Nanoscale Stamp

6.1 Introduction

In this section I describe the steps taken to implement some of the grating structures previously identified. The principal method I employed was Focussed Ion Beam milling (FIB). Atomic Force Microscopy (AFM) was then used to characterise the fabricated structures. This section begins with a short description of the FIB and AFM techniques including details that are relevant to the fabrication and characterisation of features on the required length-scale. It then provides a discussion of the steps taken to assess the resolution limits of the FIB technique. This is followed by a description of the iterative steps taken to fabricate grating structures with

the appropriate dimensions. Finally, I describe how I employed the technique to successfully fabricate larger areas of nano-scale gratings, including a transfer process to an intermediate polymer substrate.

6.2 FIB background

FIB milling is a technique which employs a focussed beam of heavy ions which are directed on to a target substrate. This beam is used both for imaging and to remove material from the substrate with high precision. The FIB microscope has many similarities to a scanning electron microscope (SEM), but in the latter case an electron beam is used in place of the ion beam. I will now describe the basic operating principles of a FIB microscope, which will serve as a useful backdrop for the rest of this chapter. A schematic of the principal components within the ion column is given in Figure 6.1.

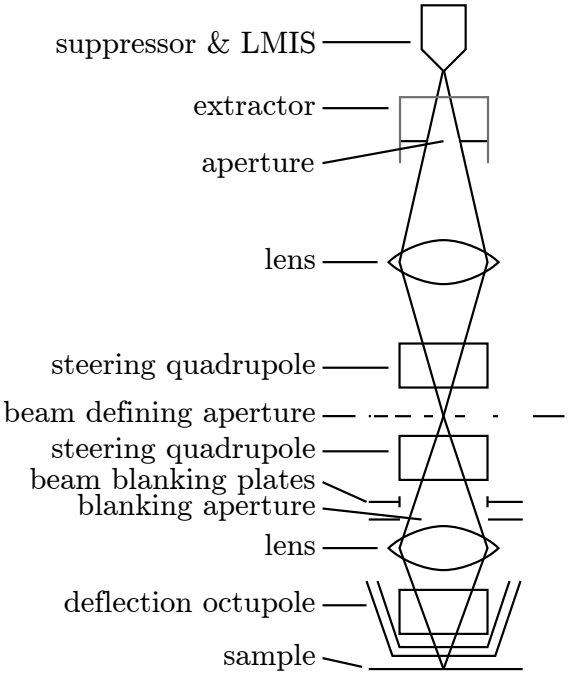

Figure 6.1 Schematic of the FIB ion column.

The first stage in the ion column is to create a stream of ions, typically gallium, from a liquid metal ion source (LMIS). To achieve this, gallium is heated at a conical tip and the molten metal flows down it, held to the tip under surface tension. A large field is applied using the extractor which leads the gallium to form a Taylor cone from which gallium ions are emitted. The stream of gallium ions first passes through an acceptance aperture, before passing through a lens and quadrupole. This is used to alter the path of the beam so that it falls in the middle of the beam-defining aperture (BDA) below it. This BDA consists of a series of apertures with differing radii. The radius of the aperture dictates the flux of ions, measured as a current, with a larger radius leading to a higher current. A steering quadrupole aligns the beam with a second lens, which focusses the beam towards the sample. Having passed through the second lens, the beam finally passes through a deflection octupole which permits the final beam shaping and deflection before it reaches the sample. There is also a beam blanking system within the column which deflects the beam from the sample when needed.

The impact of the focussed ions reaching the sample, leads to sputtering of material from the surface. A schematic of this process is shown in Figure 6.2. The relatively heavy accelerated gallium ions carry momentum which is controllable by altering the acceleration voltage. When they hit the sample, they transfer momentum to it, setting off a collision cascade [120]. As a result of this collision cascade, atoms from the sample that reach the surface with sufficient energy to overcome the surface binding energy may be ejected. The ejected material may either be a neutral atom or a a charged ion, along with secondary electrons, as illustrated in the figure. In order to form an image, a detector is used to sense either the secondary ions or secondary electrons emitted during the sputtering process. The difference in the number of these sputtered at a particular sample location provides the contrast. The imaging process is therefore destructive in a single beam FIB microscope as used in this work,

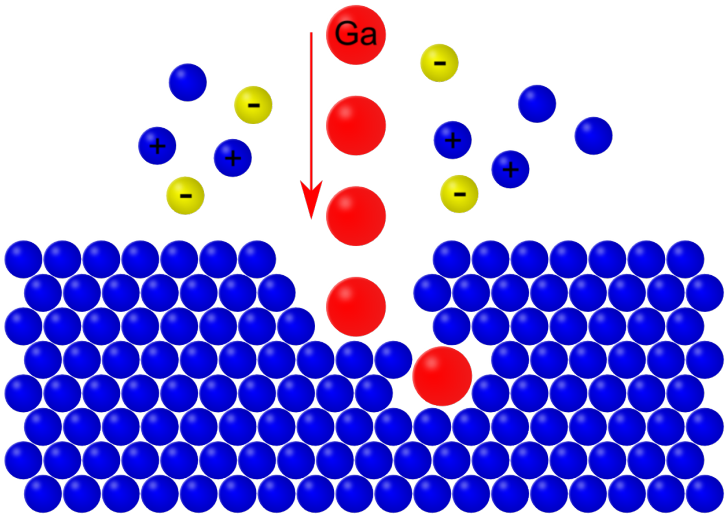

Figure 6.2 Schematic of the sputtering process showing silicon (blue) and gallium (red), along with secondary electrons (yellow). Gallium implantation is also illustrated.

due to the sputtering required.

6.3 AFM background and processing

AFM is a scanning technique which uses a very fine tip to record the topography of a sample. A silicon or silicon nitride tip is formed at the end of a cantilever attached to a holder, collectively known as an AFM probe. The tip of the probe is scanned across the sample and the topography of the sample causes deflection of the tip and therefore the cantilever. The deflection of this cantilever is measured by recording laser light reflected from it. This is achieved by using a number of photodiodes in close proximity and measuring the differential signal recorded by them. Displacement of the cantilever leads to displacement of the reflected beam which in turn leads to a different amount of light reaching each photodiode and therefore a differential signal. This signal is proportional to the angular deflection of the cantilever caused by the topography of the sample. An overall image is built up by rastering the sample so

that the tip moves across it in a series of passes. Data samples are taken during this process on either a 256×256 or 512×512 spatial grid. For this work, a Park Autoprobe CP was employed for the measurements.

There are several elements of the AFM technique that have an important bearing on the quality of the results obtained. The radius of the tip on the probe can lead to artifacts in the final images. An example of how this occurs is shown in Figure 6.3. If the probe is not sufficiently narrow to penetrate a feature on the sample which has sudden change in height, it may impinge on the sides of the feature. The resulting image will therefore follow the contour of the tip, rather than the feature itself. In order to mitigate this problem, a narrow tip with a radius of 12 nm was used. This is defined as the radius of a circle that fits the curvature of a cross-section of the tip.

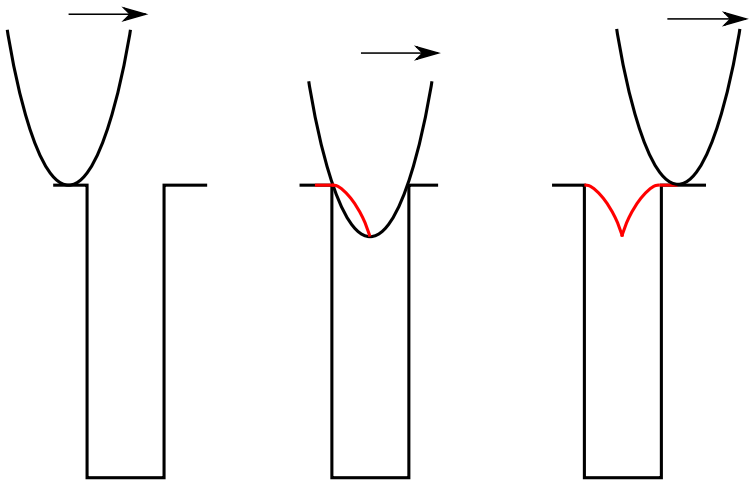

Figure 6.3 Artifact from scanning an AFM tip with a finite radius across a small feature on a sample.

The scan speed also has a strong bearing on the results. If the tip is scanned too fast over a feature with a sudden change in height, then the cantilever will not follow the profile correctly. There are some machine adjustments to help mitigate this problem, such as increasing the force with which the probe presses down on the substrate. This is achieved by altering the set point of the feedback mechanism to the position of the probe. In practice, the scan speed also needs to be reduced to around $0.5\,\mu\mathrm{ms}^{-1}$

to $1\,\mu ms^{-1}$ in order to obtain accurate recorded heights. This compares to a scan speed of around $10\,\mu ms^{-1}$ that is typically employed for samples without the ridge structures.

Finally, the scan direction has a strong influence on the obtained image. The probe can either be scanned parallel or perpendicular to the ridges. When scanning parallel to the ridges, poor image results were obtained, with much better images obtained for images scanned perpendicular to the ridges. This is due to the fact that the AFM is more accurate recording relative change in height during a single line scan, compared to absolute changes in height between lines.

Having obtained an image, there is a degree of post-processing that is sometimes necessary, due to artifacts introduced in the scanning process. These include any overall slope in the images due to mounting a sample that is not entirely flat. In addition, there is a height artifact that is introduced between scan rows during larger area scans when moving between flat and featured areas. This artefact is illustrated in Figure 6.4 for a rectangular trench. This did not appear to be such a large factor when taking small scan areas. In order to remove this artifact, code written using the Python programming language was used to take a known flat area of the sample, and find the average height profile of this region. The assumption is then made that this profile is consistent across the image, and is subtracted from each row. This assumption seems reasonable given that the silicon substrate is known to be extremely flat. In addition, isolated scans of the flat regions return flat results, strongly implying that the average slope in the other scans is an experimental artifact.

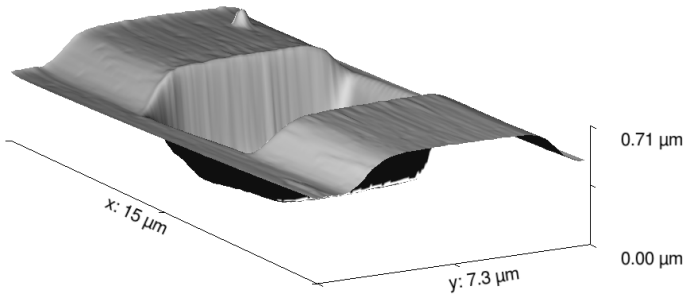

Figure 6.4 Rectangular trench exhibiting height artifacts, both an overall slope and height deviation between lines.

6.4 Development of FIB technique for nanoscale ridges

The FEI FIB software incorporates functions to mill simple shapes. The user defines the required size and depth of the feature, and the software calculates the required dwell times and performs the milling in a raster pattern. To achieve optimum control of the beam during milling, however, code written in the Matlab programming language was used in order to generate stream files, which are read by the FIB. Within these files, a series of dwell positions are defined for the beam, along with a dwell time for that position. When loaded, the ion beam is moved to each position for the duration given by the dwell time, before moving to the next position. The number of iterations of this stream file is also set, in order to achieve the overall required milling time. In order to mill continuous lines, the distance between adjacent pixels was adjusted to obtain suitable beam overlap. By altering these properties, the depth of the final mill at each position can be controlled. In addition, it is possible to

set the exact path that the beam takes over the sample. After some experimentation, a serpentine milling pattern was adopted. The beam is not blanked between dwell positions, and the serpentine pattern minimises inadvertent damage caused during a typical raster pattern as the beam moves between lines.

Conventionally, large beam currents are used in order to mill features into substrates, whilst lower beam currents are reserved for imaging. The large beam currents allow the rapid removal of material and therefore fabrication of large areas of features, at the expense of reduced resolution. In my case, however, I wished to fabricate very small features and this necessitates low beam currents in order to utilise a very narrow beam diameter and achieve optimum resolution. At these small beam currents, however, the rate of removing material (sputtering rate) is very low. This limits the featured areas that can be fabricated in a reasonable time scale.

The specifications of the instrument used, an FEI FIB 200, suggest that sufficient resolution is obtainable using beam currents around 500 pA.The specifications are typically quoted in imaging mode, however, and while it may be possible to resolve features on this length-scale at these beam currents, my requirements were to cleanly remove material. In in this case, I defined a 'milling resolution', which identifies the smallest resolvable feature that can be fabricated using the technique. This is largely limited by the dynamics of the milling system. Ion implantation and charging affect the sputtering as a function of time, for example.

There are a number of adjustable parameters which influence the milling resolution. The first is the width and shape of the spot at the substrate. The spot width can also be controlled to some extent by altering the beam current used during milling, with higher beam currents leading to a larger spot diameter. In addition, the spot shape is strongly influenced by the alignment of the instrument. The majority of this alignment is performed during the regular maintenance of the instrument, however

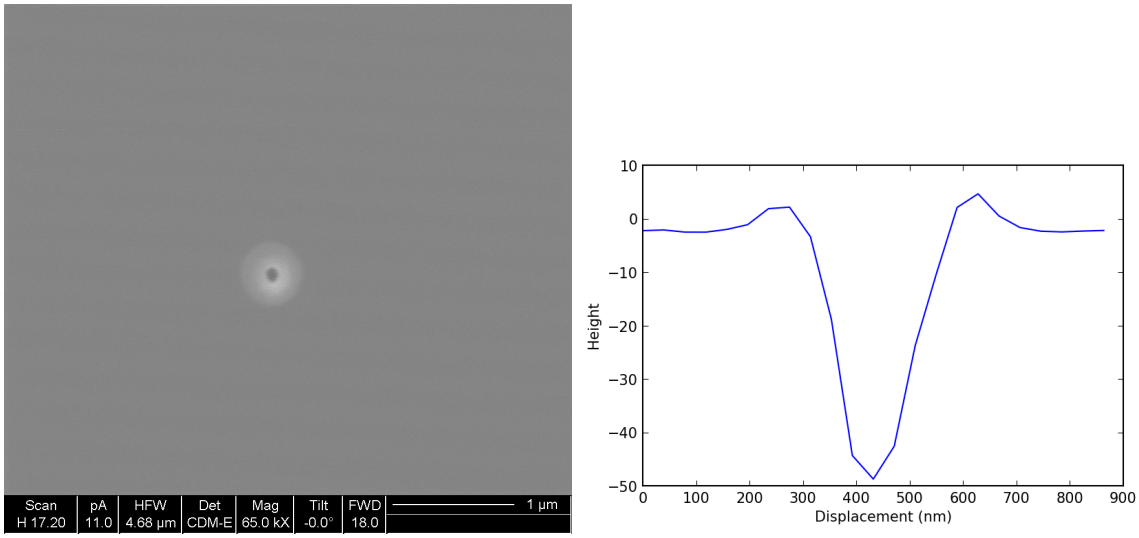

(a) 30pA spot and redeposition tail (b) AFM cross-section

Figure 6.5 FIB image and AFM cross section of a spot milled at 30 pA.

the user has control over the eucentric height of the specimen, astigmatism correction, and the focus. Any astigmatism or small deviation from perfect focus can lead to a wider or misshaped spot which reduces the milling resolution as it increases the overlap between adjacent spots. During every session, this was corrected for as much as possible, but as I worked at the edge of the resolution limit of the machine, small maladjustments were found to lead to unacceptable losses in resolution. This process was further complicated by the use of clean silicon substrates which were extremely flat and ideally had few discernible surface features which would otherwise aid focussing. The human error in the focussing of the instrument therefore led to some deviation in the achievable milling resolution.

In addition to the spot shape, there is a redeposition tail which forms at the edge of the milled region, as previously discussed. To illustrate the effect of this, a point was milled a point for a few seconds under the smallest beam currents. A FIB image of the resulting spot and tail is shown Figure 6.5. The dark milled hole in the centre is surrounded by a lighter halo of redeposition. In the same figure the height profile, as extracted from an AFM scan of the milled spot, is shown to characterise the spot

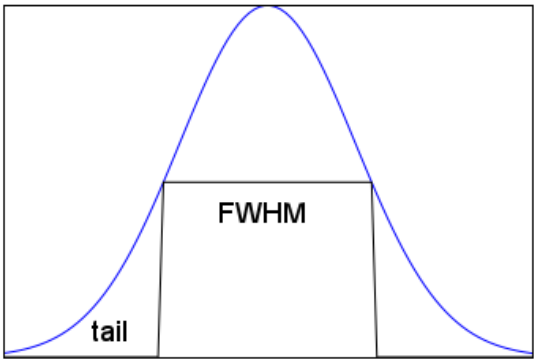

Figure 6.6 Schematic of a Gaussian ion beam profile, showing the full width at half maximum (FWHM) and beam tails.

shape further. The profile of the milled spot shows good agreement with Tseng [121]. The width of the spot appears to be of the order of 300 nm for a 50 nm trench, with a beam current of 30 pA. The redeposition at the edges of the spot reaches around 5 nm in height, and is around 50 nm wide on both sides. It is difficult to characterise the amount of redeposition that occurred within the milled spot. Redeposition of this kind may have difficulty escaping the spot and so may be a sizeable amount. Its overall effect would be to decrease the rate at which trenches can be dug.

An important result obtained from the AFM profile is that the width of the spot and the redeposition act to limit the resolution of the achievable features to around 300 nm. The profile of the spot feature revealed that the mouth of the spot is relatively wide. This can be explained due to the profile of the gallium ion beam. This can be approximated as a Gaussian for small beam apertures [122], as shown in Figure 6.6. The realistic width of the beam is given by the full width at half maximum (FWHM), in addition to the tails which form at the edge of the spot. For longer dwell times, these tails may lead to substantial widening of the mouth of the dwell spot.

In order to more rigorously assess the limit of achievable milling resolution using

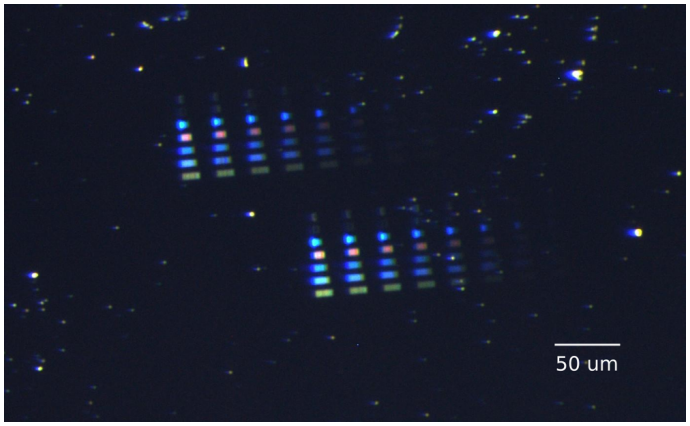

Figure 6.7 Optical image of ridges cut into a silicon substrate for two beam currents, at a variety of dwell times and periodicities between 200-1400 nm.

this instrument, a series of lines with decreasing periodicity were cut into a silicon substrate. This experiment was repeated a number of times for different beam currents in order to alter the nominal spot diameter. The FIB was set to mill a set number of lines for a given period, hence the overall extent of the milled region increases with increasing period. An optical image of an example set of ridges at two different beam currents and a variety of dwell times is shown in Figure 6.7. The period of these ridges varies from 200 nm to 1400 nm. Different colours are observed due to the interaction of the microscope illumination and the grating formed by the periodic lines. At the lowest periodicities, beam overlap may be disrupting the ridges, altering the colour observed. In addition, the intensity of the colour decreases moving horizontally as the depth of the features decreases due to the reduced dwell time. The white spots present are most likely to be dirt on the surface of the sample.

To obtain some analytical data, AFM scans were performed on each set of lines and height profiles were extracted from them. A typical AFM image, visualised in 3D, is shown in Figure 6.8a. Height profiles were extracted from these AFM images, as shown in Figures 6.8b-d. Figure 6.8b demonstrates that discrete lines were formed at large periods. As the period of the lines was reduced the lines eventually formed a continuous grating, as shown in Figure 6.8c. As the period is reduced further, as

in Figure 6.8d, a trench begins to form and periodic lines can be seen within it. At this point the width of the beam was too wide to cut discrete features as there was overlap between adjacent lines. I note that the tail of the Gaussian beam shape may play an increasingly noticeable role as the dwell time and so feature depth is increased.

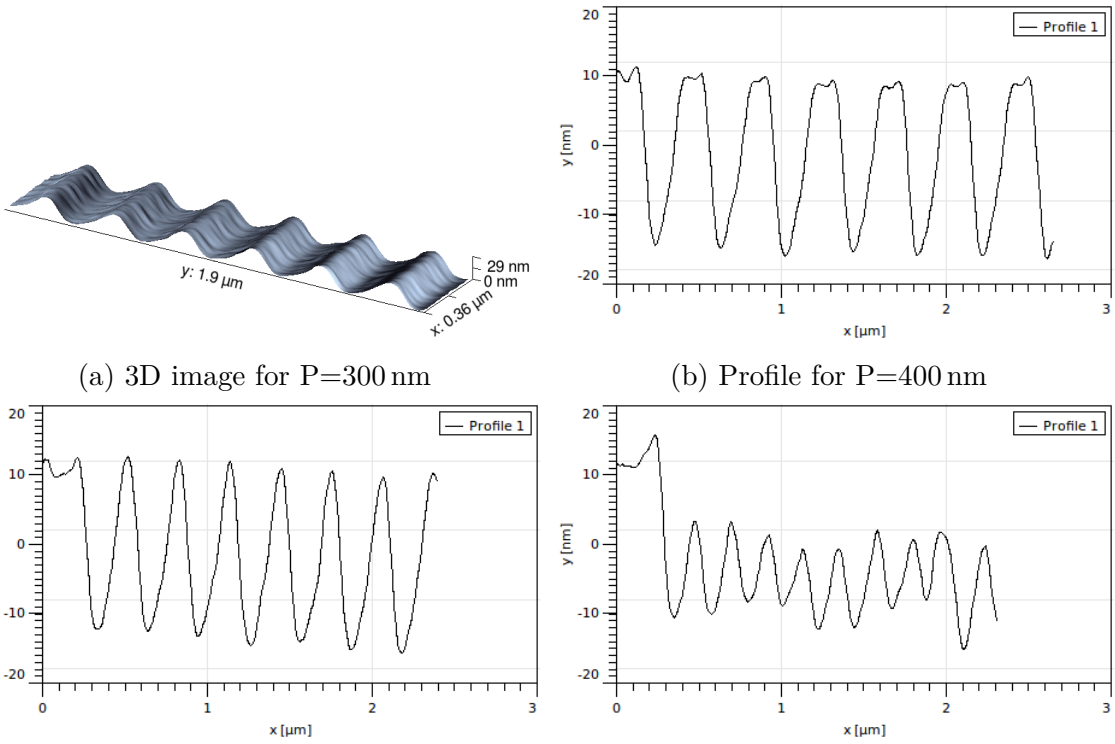

(a) 3D image for P=300 nm

(b) Profile for P=400 nm

(c) Profile for P=300 nm

(d) Profile for P=250 nm

Figure 6.8 A typical 3D image, and extracted height profiles for lines milled at 100 pA, with periodicities P as labelled.

As the period of the lines was reduced yet further, the depth of the trench continued to increase. Ridges are formed with the correct nominal periodicity, but their height is reduced by the beam overlap, which acts to smooth them. This makes it increasingly difficult to discern the individual ridges. From these data, it was possible to assess the minimum milling resolution, which was defined as the point at which the beam overlap occurs such that individual lines could not be milled. From the simulation results of the previous chapters, features with a periodicity of around 300 nm are ideally required. For this reason, it was necessary to employ a beam of at most

100 pA. Even with a beam current as low as 30 pA, the smallest consistent resolution achievable was 200 nm to 250 nm.

Having ascertained the optimum parameters in order to achieve the required periodicity, it was necessary to achieve the correct feature depth. In order to get a quantitative idea of the dwell time required for a given feature height, a square pattern was milled and the total time for this mill was recorded at a nominal beam current of 1000 pA. AFM height profile data was taken and was then processed to remove the AFM artefacts previously described. The processed AFM data is shown in Figure 6.9. In passing, I note that parallel lines can be observed which follow the path of the ion beam as it milled the features.

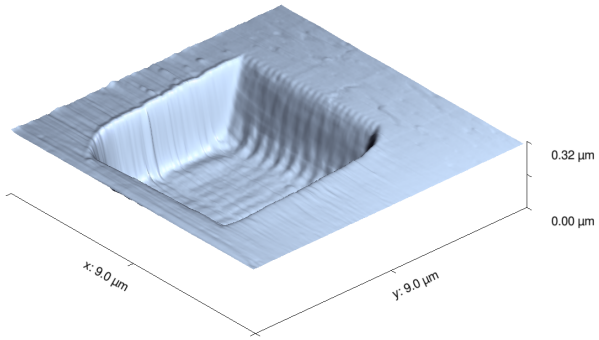

Figure 6.9 Processed AFM data of a rectangular trench.

From the AFM profile data, the overall volume of material removed during the milling process was calculated. Using this volume, the beam current and overall dwell time, a sputter rate of 0.2 μm^3/nC was computed, which gives the volume of material removed for a given deposited charge of gallium ions. This is somewhat smaller than reported in the literature [123]. This may be due to some redeposition within the trench, which is a strong function of dwell time and the milling pattern. The milling rate calculated gives a useful indication, however, of the total dwell time required to remove a given volume of material using the system.

Altering the beam current alters the rate at which ions are deposited and therefore the rate of removing material from the substrate. So, in order to calculate the dwell times at each pixel for a given pattern, the volume of the final shape was calculated and divided by the sputtering rate and beam current. This then gives the average dwell time required for each pixel. For a pattern with uniform depth, this is sufficient information. For a non-uniform pattern, it was possible to simply weight each dwell position by the height required. In addition, the overall extent of the pattern was calculated such that it was possible to fabricate this pattern area within a given time frame. In the case of the periodic ridges, they were treated as triangular prisms with a height of approximately 50 nm. Running the FIB overnight for 10 hours, to allow for sample loading and alignment, it was possible to fabricate feature areas of order $8000\,\mu m^2$.

A goal of the project was to be able to fabricate ridges with a controllable depth. As a first approximation, the technique described above using the sputter rate was used to estimate the volume of material to be removed and therefore the length of the mill required. In practice, however, the situation is more complicated, and the feature depth does not increase linearly with dwell time. This is due to broadening of the features with dwell time, due to the beam shape, as described above. In addition, non-uniform redeposition may occur preferentially within the ridges which may lead to a reduction in the rate at which the ridges can be cut. In practice it was therefore necessary to systematically vary the dwell time for each ridge at a number of periodicities and assess the height and width of the features fabricated using AFM scans.

In order to achieve the same overall dwell time for the pattern, it is possible to alter either the dwell time at each pixel, or the total number of iterations of the pattern. This has a great influence on the final result achieved. The origin of this is largely

due to the scan speed. At short local dwell times, with a high number of pattern iterations in order to achieve the same overall pattern time, the speed of the scanning beam is higher. This reduces re-deposition, but this must be balanced against a decrease in the sputtering rate [124]. This is due to the angle that the incident beam forms with the perpendicular to the line at which sputtering takes place. At lower scan speeds this angle increases which leads to an increased sputtering rate, as described above. A local dwell time of around 1 ms was chosen to offer a reasonable compromise between redeposition and sputtering rate.

6.5 Final master stamp

Through the processes described in Section 6.4 I was able to obtain an optimum set of parameters that enabled the fabrication of ridges with appropriate dimensions. I achieved this by milling a series of parallel lines, as in the tests above, with the appropriate beam current such that the milled trenches just touched. This gave a ridge profile of a slightly softened triangle, as described above. However, the rounding of the triangular ridges would not have a significant impact on solar cell devices fabricated using such a stamp, as described in Chapter 3. I therefore began milling larger sample areas for characterisation. Silicon was chosen as the substrate due to its high degree of flatness.

Milling at high magnifications, as performed until this point, required scanning of the sample stage to achieve a large area of features, due to the reduced field of view. The movement of the stage led to stitching errors, in which there was a small gap between adjacent patterned areas, or worse overlap between them. This occurs due to the relatively coarse movement of the stage and backlash inherent in the movement. To reduce these errors, the mills were therefore performed at low magnifications to

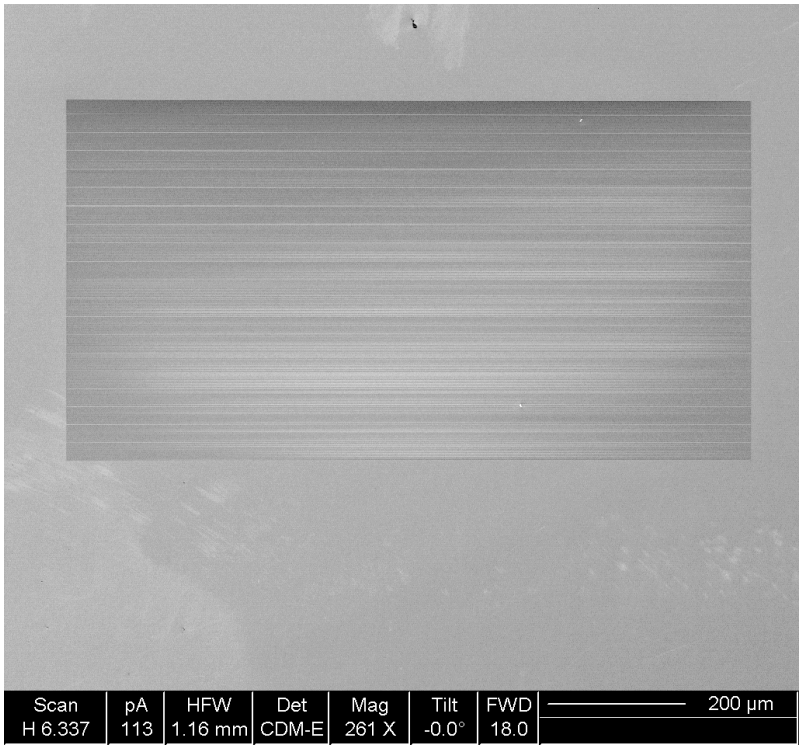

Figure 6.10 Typical FIB image of the final ridges formed.

increase the field of view. This initially produced poor results that were inconsistent with the tests previously performed. This was due to a machine limitation such that the beam position can only be defined on a 4096×4096 grid. This is due to the 12 bit card used to drive the beam deflection system, which allows integers up to $2^{12} = 4096$. The field of view is therefore split into 4096 discrete pixels. At high magnifications, the pixels translate into an adequate spatial resolution on the sample, but at lower magnifications this resolution is not sufficient. If a ridge periodicity does not fall at an integer grid position, snapping to the closest available position causes the ridge periodicity to be disrupted. To mitigate this effect, the magnification was set such that the ridge periodicity fell at integer multiples of the pixel spacing. A typical FIB image of the ridges fabricated is shown in Figure 6.10.

Difficulties arose in achieving consistent good focus and astigmatism correction. These processes should be performed near the target area for the stamp, as the

sample may not be exactly level. As described previously, imaging is a destructive process, so focus had to be achieved as quickly as possible. The lack of features on the clean silicon substrate also hindered this process. The patterns were milled in the centre of the sample area to prevent damage due to sample handling, but this removed an edge which would otherwise serve as a useful reference for focussing. It was typically therefore necessary to rely on the presence of a small amount of dust to assist with focussing. This made it difficult to consistently achieve 300 nm periodicity ridges with the required depth and profile, though it was possible. It was, however, possible to consistently fabricate a number of substrates each containing ridges with a 350 nm and 400 nm periodicity. The areas milled were $65 \times 65\mu m^2$. To increase the area that can be milled, gas-assisted FIB milling could potentially be used to increase the sputtering rate. This may also improve the aspect ratio of the features that could be fabricated, and therefore reduce the period of the ridges that could be formed. This capability was not available on the machine used for the current research.

6.6 PDMS transfer

The next important stage in the fabrication process is the transfer from the hard silicon master to the active layer of the final devices. In order to achieve scalability, it is beneficial to first transfer the stamp to a soft intermediate stamp. This soft stamp could then be used to imprint final active devices without degrading the original hard master, which takes a long time to fabricate. I utilised a simple transfer method using polydimethylsiloxane (PDMS), whose basics steps are illustrated in Figure 6.11.

The silicone used is sold as Sylgard 184 and is readily available at low cost. The

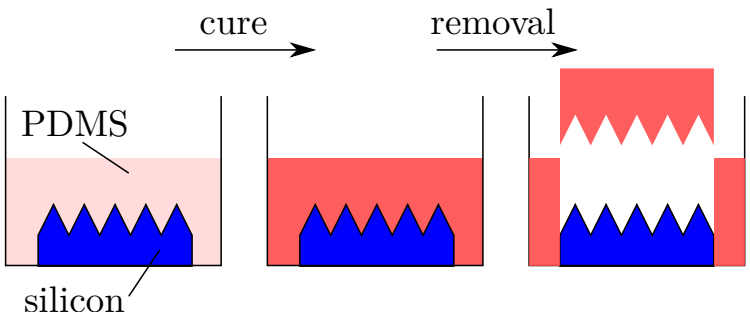

Figure 6.11 Schematic of the PDMS transfer process.

method followed was to mix the base silicone and curing agent in a 1:10 ratio, then agitate vigorously to thoroughly mix the two compounds. The resulting mixture was degassed by placing under vacuum in a desiccating chamber for 1 hour. This removes air bubbles from the mixture which could otherwise be present in the final stamp. The master silicon substrate was placed with the grating facing upwards and then the degassed mixture was poured on top, slowly so as to prevent the formation of large air bubbles. The depth of the mixture on the stamp dictated the final thickness of the polymer intermediate. This was chosen to be around 2 mm to 3 mm, which is thick enough for good mechanical stability, but still allows some flexibility such that the polymer stamp is not brittle. The stamp and silicone mixture were then cured at 140 °C under vacuum for 1 hour. Curing under vacuum encourages the silicone mixture to penetrate into the nano-features of the grating.

In order to assess the resultant polymer stamp, a standard optical microscope was used to observe the featured regions and qualitatively assess that a transfer had taken place. This is demonstrated in Figure 6.12, but it is not, of course, possible to resolve the individual lines of the grating using this technique. To do so, AFM scans were performed on the imprinted regions. These were performed in tapping mode as

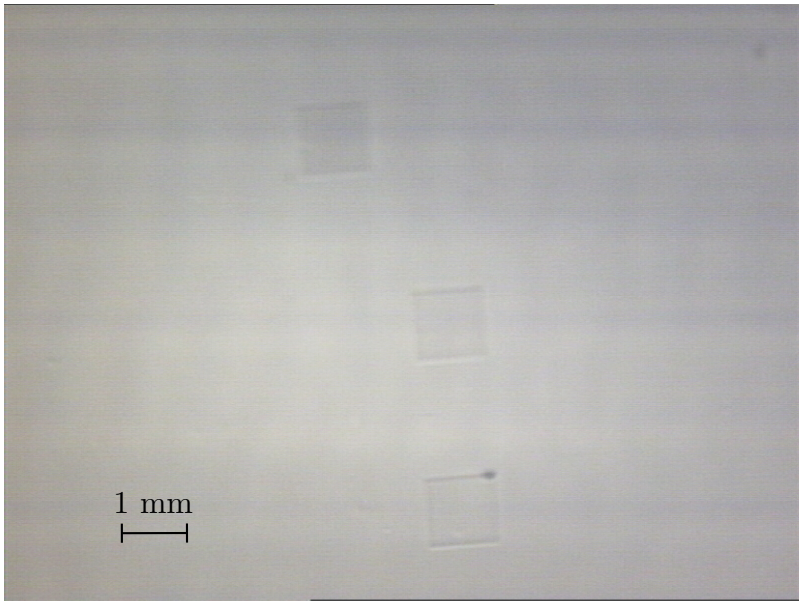

Figure 6.12 Optical image of PDMS with 3 regions of transferred nano-features.

the cured PDMS is too soft to enable the use of contact mode which would erode the material quickly. In tapping mode, the AFM cantilever is driven resonantly and oscillates up and down tapping the surface. As the tip interacts with the sample surface, intermolecular forces cause a measurable reduction in the amplitude of the oscillations which is used to map the surface. This method greatly reduced the force applied to the relatively soft PDMS surface. Even in tapping mode, the AFM probe occasionally picked up small pieces of the polymer that had a detrimental effect on the resolution obtained. In this case, it was often necessary to change probes, or wait for the material to become dislodged.

A typical AFM scan of the final ridges is shown in Figure 6.13. We can see that the grating is reproduced well in the PDMS mould. The height of 60 nm appears to be similar to that of the initial silicon master stamp. The absolute values must be read with some caution, however, given that in the case of the PDMS measurements tapping mode scans were performed in contrast to the contact mode scans performed on the silicon masters. The effective manner in which the PDMS adopts the features of the grating is somewhat unexpected due to its hydrophobicity [125].

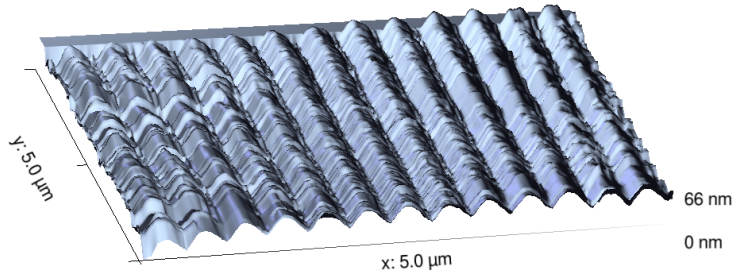

Figure 6.13 Processed AFM scan of featured PDMS stamp, visualised in 3D.

This simple method of transfer appears to provide the necessary resolution to transfer nano-scale grating features from a hard silicon stamp. I have achieved the fabrication of polymer stamps with a periodicity down to 350 nm, and with a feature depth of ∼60 nm. This PDMS stamp could then be used to imprint the active layer of a solar cell device, using techniques such as those discussed previously [67]. A metal contact could then be evaporated onto this indented active layer. After evaporation, a metallic nano-grating in close contact with the active layer would result, and provide a good approximation to the optimum devices simulated in Chapter 3. Due to the small area of features that can be fabricated using the FIB technique, only a small region of the final device will exhibit the structured electrode, whilst the remaining areas will maintain a planar electrode. This could enable on-sample comparisons between featured and control areas of the same cell, which would remove the effects of inter-sample variation. In addition, it ensures that both the control and featured devices have undergone the exact same fabrication conditions. This would allow the direct attribution of absorption enhancements to the presence of the featured electrode.

Previous work in the literature has employed alternative methods to fabricate the master stamp. Na *et al.* used two argon laser beams to form a sinusoidal interference pattern which was used to cure an azo polymer. This method allows a relatively large area of features to be fabricated and the feature period and height can be controlled by the angle of incidence and irradiation time. This method perhaps provides a more robust method to crate a larger area of features, but even so this would not be sufficient in scale for a commercial solar panel. It also does not have the kind of fine control that I have demonstrated using the FIB technique, nor the ability to vary the feature geometry within a single sample.

Other grating fabrication methods include electron-beam lithography, which is capable of resolutions better than 10 nm, but typical resolutions are closer to 20 nm [126, 127]. This displays an advantage over the FIB techniques of this work. The FIB technique, however, far more readily allows the fabrication of 3D features, including those with high aspect ratio [128].

It may be possible to provide a truly large area stamp by using a series of imprinting steps into an intermediate, where the master stamp is translated between steps. This carries with it several challenges, such as stitching errors between the imprinted regions. These should not be so deep that they may cause shorting of the final devices. In addition, if it is necessary to use thermal cycling during the imprinting steps, these may significantly reduce throughput, or even preclude the technique entirely. The method has the potential, however, to provide a truly scalable solution if these challenges are overcome.

To tie the experimental and simulation work together, simulations were performed using the grating profile extracted from the AFM data. It is therefore possible to make some comments regarding how experimental deviation from the ideal shape may influence the absorption within devices fabricated from these master gratings.

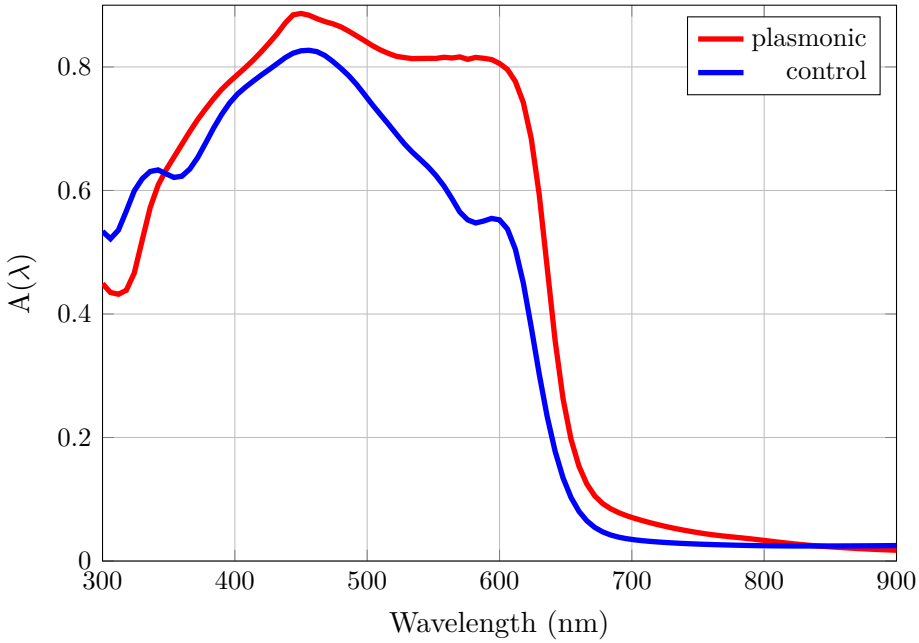

Figure 6.14 Absorption spectra of control and plasmonic devices. The grating profile has been extracted from AFM data and incoporated into a simulated device with a 120nm active layer and a silver electrode.

AFM profile data from a fabricated 300 nm grating were used in the simulations and the absorption spectra compared to a control device are shown in Figure 6.14, for a silver grating. The shift in interference can be seen at short and intermediate wavelengths, and the bulge around 600 nm is due to the surface plasmon mode. From these data, absorption currents of 13.85 $\mathrm{mAcm^{-2}}$ and 13.10 $\mathrm{mAcm^{-2}}$ were calculated for a silver and aluminium grating, respectively. These currents are very close to the absorption currents simulated for an optimum grating structure. This therefore suggests that a small amount of roughness and fabrication inconsistency will not have a significant impact on experimental devices incorporating gratings.

6.7 Chapter summary

In this chapter, I demonstrate the steps taken to assess the limitations of the FIB, in this case an FEI FIB 200, for the fabrication of nanoscale triangular ridges. This was motivated by the FIBs inherent flexibility to create complex 3D structures and the potential to achieve sub-micron resolution. Through this work, I identify the factors that limit this resolution and the practical extent to which the FIB can be employed in this capacity. I demonstrate that nanoscale ridges with periodicity down to 300 nm can be fabricated in silicon substrates. The areas that can be achieved are relatively small, of order 50 µm × 50 µm, but multiple areas with varying parameters can easily be achieved on a single substrate.

Using these silicon substrates, I go on to develop and test a method to transfer from the hard silicon master to a soft PDMS intermediate that can be used to imprint organic solar cell devices. The fidelity of the transfer process is high and within the errors inherent in the AFM technique used to characterise the samples. This stamp could then be used to imprint the active region of complete devices to achieve a textured back contact. Due to the variety of periodicities and heights that can be patterned onto a single stamp using the FIB technique, comparisons between the effect of gratings of varying periodity and height on a single solar cell sample could be performed. This negates variation between samples as all grating areas undergo the same fabrication conditions. Using valuable information gained in this fashion, the stamping method could potentially be utilised for a high throughput of devices, with an alternative method used to achieve a large area master stamp. Typically, methods to achieve this could include interference lithography.

CHAPTER 7

Final Conclusions

Through this work I have performed a detailed analysis of the application of rear electrode gratings to enhance the efficiency of thin-film organic solar cells. In Chapter 3, I have ascertained that there is a strong degree of optimisation that can be performed on planar organic solar cell devices. I have demonstrated that the inclusion of a grating at the rear electrode has a marked effect on the absorption spectrum of these devices. Further to this, I took detailed look at the mechanisms by which the structured electrode leads to absorption enhancement. I identified three mechanisms of enhancement: multilayer interference, surface plasmon modes, and scattering of the grating order modes. This dissection of independent but simultaneously occurring mechanisms of enhancement adds greater clarity to the analysis of experimental results.

In Chapter 4 I have taken a more detailed look at the enhancement of devices using gratings. I calculated theoretical band structures for the surface plamon modes based

on the dispersion of surface plasmons at a planar interface. This led to a summary of the dependence of the surface plasmon mode excitation wavelength on grating period, serving as a useful reference for P3HT:PCBM based devices. It provides useful insight into the design of featured electrodes in the context of thin-film cells, both in the field of organic solar cells and beyond.

Following this section, I performed an optimisation of the overall absorption that can be achieved in organic solar cell devices incorporating gratings. Overall absorption current enhancements of up to 10% and 4.5% are possible for silver and aluminium electrodes respectively, when making a realistic comparison to optimised control devices. In practical devices, aluminium is a cost-effective choice with good electrical properties and I have demonstrated that an enhancement can be attained with this metal. Rectangular and sinusoidal gratings have also been shown to provide of up to 6.5% and 8% respectively for a silver electrode. I have also demonstrated the benefits of 2D gratings which may have a significant benefit due to the polarisation-independence of their enhancements.

There was a broad tolerance to grating parameters, including the grating width and height, and the sharpness of the triangular grating features. This suggests that the practical realisation of devices incorporating gratings is robust to fabrication inconsistencies. The results so far presented have investigated the optical effects of gratings at the rear electrode without a detailed analysis of the electrical effects that would arise because of their incorporation. A valuable extension of this work would to implement a charge extraction model starting with exciton generation rates as a function of position from FDTD modelling.

In Chapter 5, I have looked at many factors in practical devices that affect the absorption enhancments that can be generated using gratings. I identify that there is a good insensitivity to the angle of incidence, up to around 15°, with a slight

enhancement at small angles, with positive implications for practical devices.

Absorption under a diffuse illumination spectrum leads to comparable enhancements to the direct spectrum. This suggests that the featured devices investigated will be useful in countries where cloudy conditions are frequent, such as in the UK. The diffuse light occurs over a broader range of angles, and the effects of angled illumination identified will therefore also play a part.

The choice of materials employed to fabricate the devices will have an impact on their optical properties. The choice of substrate was seen to have a limited impact on the absorption, with PET, which is useful for flexible devices, leading to a small detriment compared to a glass substrate. A wide variety of active materials are being explored, and a small sample of these were compared in terms of their effect on the surface plasmon excitation wavelength. Although differences were observed, the change in excitation wavelength at a particular grating period was confined to a relatve narrow range of around 100 to 150 nm, despite the apparently large differences in refractive index. This suggests the required grating features to effect good enhancements will be broadly similar across a number of materials. Additional buffer layers introduced into the devices led to changes in the absorption spectra, with large changes evident in the multilayer interference. For a particular device geometry, simulations of the type described would therefore be of great benefit for optical engineering of optimum devices.

In Chapter 6, I described practical steps taken towards the experimental realisation of the optimum simulated devices. I utilised a focussed ion beam method to fabricate a hard master stamp in silicon. This method, although relatively low throughput, enables the variation of feature dimensions. I have assessed the limit of the technique using an FEI FIB 200 and achieved grating periodicities down to 300 nm. In addition, I have described a technique to transfer from the hard silicon master to a soft PDMS

intermediate stamp with high fidelity. This could in turn be used to stamp the photoactive region of an organic cell prior to electrode evaporation, leading to a nanostructured final device. Using the FIB technique, areas with multiple periods can be fabricated on a single sample. This could provide a valuable method to make comparisons between grating periodicities on a single sample. This would give a rigorous insight into the effects of gratings embedded into the electrodes of organic solar cell devices.

Within the context of the field of thin-film photovoltaic research, this work has provided new insights into the design of structures to enhance thin-film organic solar cells. It builds on and supplements previous work studying simple grating structures placed at the rear electrode. By simulating the full device structure, additional mechanisms of enhancement are demonstrated, and a realistic appraisal of the benefits of gratings structures can be made. A detailed exploration of the mechanisms of enhancements provides further insights to aid the design of these structures. In addition, this work considered the effects of additional factors that influence the efficacy of plasmonic structures when used in practical devices. This helps to provide a pathway towards optimising thin-film organic solar cells for use under realistic conditions.

This work has focussed on the optical design of thin-film organic solar cells. A worthy extension to the work would be to couple the optical simulations with charge extraction models. The simulations described in this work provide the spatial distribution of exciton generation. These data could be used as the entry data to a charge extraction model which would facilitate more accurate estimates of device efficiency, and therefore help better inform the design of structures for overall device enhancement.

Further, there is a significant scope to develop alternative structures to employ at the

rear electrode. Blazed gratings may provide enhanced coupling into beneficial modes at off-normal incidence, for example. Chirped gratings, in which the periodicity varies across the grating, could be employed to excite modes under a range of incident wavelengths. This has the potential to broaden the enhancements spectrally and potentially also improve the angular tolerance of the devices.

The experimental results provide a clear starting point for further work. The FIB has been demonstrated as a potential technique to fabricate customised gratings for use in lab-scale devices. Scaling to larger sizes would prove difficult, however. Alternative techniques such as laser interference or electron beam lithography might prove fruitful avenues to explore for large-scale fabrication of features with a similar geometry.

The wider field of thin-film photovoltaics is advancing in a number of directions. There is a particular interest in lower-bandgap polymer blends and also in perovskite devices, which have demonstrated substantial improvements in efficiency over recent years. The current work has the potential to help inform the design of optical structures which could be used to provide further enhancements in these other device architectures. The methods used, employing both theoretical band structures and FDTD simulations, could be readily applied to these alternative materials. The use of grating structures at the rear electrode may prove to be of benefit in devices employing these future materials.

Organic solar cells offer a promising route for harvesting energy from the Sun using a cheap and scalable architecture. Incorporating gratings into the rear electrode provides a highly tunable and robust system to improve the optical properties of these devices. This work has aimed to provide a valuable insight into the processes through which these systems can be enhanced and will hopefully lead to further fruitful investigation in the field.

References

[1] Abass, A., Shen, H., Bienstman, P. & Maes, B. Angle insensitive enhancement of organic solar cells using metallic gratings. *Journal of Applied Physics* **109,** 023111 (2011).

[2] Sefunc, M. A., Okyay, A. K. & Demir, H. V. Plasmonic backcontact grating for P3HT:PCBM organic solar cells enabling strong optical absorption increased in all polarizations. *Optics express* **19,** 14200–9 (2011).

[3] Jayawardena, K. D. G. I. *et al.* 'Inorganics-in-Organics': recent developments and outlook for 4G polymer solar cells. *Nanoscale* **5,** 8411–27 (2013).

[4] Hoppe, H. & Sariciftci, N. S. Organic solar cells: An overview. *Journal of Materials Research* **19,** 1924–1945 (2004).

[5] Li, G., Zhu, R. & Yang, Y. Polymer solar cells. *Nature Photonics* **6,** 153–161 (2012).

[6] He, Z. *et al.* Enhanced power-conversion efficiency in polymer solar cells using an inverted device structure. *Nature Photonics* **6,** 591–595 (2012).

[7] Ma, W., Yang, C., Gong, X., Lee, K. & Heeger, A. J. Thermally Stable, Efficient Polymer Solar Cells with Nanoscale Control of the Interpenetrating Network Morphology. *Advanced Functional Materials* **15,** 1617–1622 (2005).

[8] Li, G. *et al.* High-efficiency solution processable polymer photovoltaic cells by self-organization of polymer blends. *Nature Materials* **4,** 864–868 (2005).

[9] Ko, C.-J., Lin, Y.-K., Chen, F.-C. & Chu, C.-W. Modified buffer layers for polymer photovoltaic devices. *Applied Physics Letters* **90,** 063509 (2007).

[10] Gan, Q., Bartoli, F. J. & Kafafi, Z. H. Plasmonic-enhanced organic photovoltaics: breaking the 10% efficiency barrier. *Advanced materials* **25,** 2385–96 (2013).

[11] Søndergaard, R., Hösel, M., Angmo, D., Larsen-Olsen, T. T. & Krebs, F. C. Roll-to-roll fabrication of polymer solar cells. *Materials Today* **15,** 36–49 (2012).

[12] Frenkel, J. On the transformation of light into heat in solids. I. *Physical Review* **37,** 17–44 (1931).

[13] Thompson, B. C. & Fréchet, J. M. J. Polymer–Fullerene Composite Solar Cells. *Angewandte Chemie International Edition* **47,** 58–77 (2008).

[14] Blom, P., Mihailetchi, V., Koster, L. J. A. & Markov, D. E. Device Physics of Polymer:Fullerene Bulk Heterojunction Solar Cells. *Advanced Materials* **19,** 1551–1566 (2007).

[15] Choy, W. C. H. *Organic Solar Cells: Materials and Device Physics* (Springer, 2012).

[16] Sariciftci, N. S., Smilowitz, L., Heeger, A. J. & Wudl, F. Photoinduced Electron Transfer from a Conducting Polymer to Buckminsterfullerene. *Science* **258,** 1474–1476 (1992).

[17] Onsager, L. Initial recombination of ions. *Physical Review* **54,** 554 (1938).

[18] Braun, C. L. Electric field assisted dissociation of charge transfer states as a mechanism of photocarrier production. *The Journal of Chemical Physics* **80** (1984).

[19] Servaites, J. D., Savoie, B. M., Brink, J. B., Marks, T. J. & Ratner, M. A. Modeling geminate pair dissociation in organic solar cells: high power conversion efficiencies achieved with moderate optical bandgaps. *Energy & Environmental Science* **5,** 8343 (2012).

[20] Tsoi, W. C. *et al.* Effect of Crystallization on the Electronic Energy Levels and Thin Film Morphology of P3HT:PCBM Blends. *Macromolecules* **44,** 2944–2952 (2011).

[21] Scharber, M. *et al.* Design Rules for Donors in Bulk-Heterojunction Solar Cells—Towards 10 % Energy-Conversion Efficiency. *Advanced Materials* **18,** 789–794 (2006).

[22] Garcia-Belmonte, G. G. & Bisquert, J. Open-circuit voltage limit caused by recombination through tail states in bulk heterojunction polymer-fullerene solar cells. *Applied Physics Letters* **96,** 113301 (2010).

[23] Pivrikas, A., Neugebauer, H. & Sariciftci, N. S. Charge Carrier Lifetime and Recombination in Bulk Heterojunction Solar Cells. *IEEE Journal of Selected Topics in Quantum Electronics* **16,** 1746–1758 (2010).

[24] Koster, L. J. A., Mihailetchi, V. D. & Blom, P. W. M. Ultimate efficiency of polymer/fullerene bulk heterojunction solar cells. *Applied Physics Letters* **88,** 093511 (2006).

[25] Forrest, S. The limits to organic photovoltaic cell efficiency. *MRS bulletin* **30,** 28–32 (2005).

[26] Liang, Y. *et al.* For the bright future – bulk heterojunction polymer solar cells with power conversion efficiency of 7.4%. *Advanced materials* **22,** E135–8 (2010).

[27] He, Z. *et al.* Simultaneous enhancement of open-circuit voltage, short-circuit current density, and fill factor in polymer solar cells. *Advanced materials* **23,** 4636–43 (2011).

[28] Maier, S. A. *et al.* Plasmonics – A route to nanoscale optical devices. *Advanced Materials* **13,** 1501–1505 (2001).

[29] Ritchie, R. H. Plasma losses by fast electrons in thin films. *Physical Review* **106,** 874–881 (1957).

[30] Powell, C. J. & Swan, J. B. Origin of the characteristic electron energy losses in magnesium. *Physical Review* **116,** 81–83 (1959).

[31] Powell, C. J. & Swan, J. B. Origin of the characteristic electron energy losses in aluminum. *Physical Review* **115,** 869–875 (1959).

[32] Maier, S. A. *Plasmonics: Fundamentals and Applications* 1–223 (Springer, 2007).

[33] Stern, E. A. & Ferrell, R. A. Surface plasma oscillations of a degenerate electron gas. *Physical Review* **120,** 130 (1960).

[34] Kretschmann, E. Decay of non radiative surface plasmons into light on rough silver films. Comparison of experimental and theoretical results. *Optics Communications* **6,** 185–187 (1972).

[35] Otto, A. Excitation of nonradiative surface plasma waves in silver by the method of frustrated total reflection. *Zeitschrift für Physik* **216,** 398–410 (1968).

[36] Teng, Y. Y. & Stern, E. A. Plasma radiation from metal grating surfaces. *Physical Review Letters* **19,** 511–514 (1967).

[37] Wood, R. W. On a Remarkable Case of Uneven Distribution of Light in a Diffraction Grating Spectrum. *Proceedings of the Physical Society of London* **18,** 269–275 (1902).

[38] Mills, D. Interaction of surface polaritons with periodic surface structures; Rayleigh waves and gratings. *Physical Review B* **15,** 3097 (1977).

[39] Agranovich, V. M. *Surface polaritons* (Elsevier, 2012).

[40] Chandezon, J., Dupuis, M., Cornet, G. & Maystre, D. Multicoated gratings: a differential formalism applicable in the entire optical region. *JOSA* **72** (1982).

[41] Maxime, C. & Fick, J. Surface plasmon polaritons in sub-wavelength metallic gratings studied by higher-order angle-resolved spectroscopy. *The European Physical Journal Applied Physics* **48,** 10901 (2009).

[42] Giannattasio, A. & Barnes, W. Direct observation of surface plasmon-polariton dispersion. *Optics Express* **13,** 428–34 (2005).

[43] Constant, T. J. *et al.* Direct mapping of surface plasmon dispersion using imaging scatterometry. *Applied Physics Letters* **102,** 251107 (2013).

[44] Hooper, I. & Sambles, J. Dispersion of surface plasmon polaritons on short-pitch metal gratings. *Physical Review B* **65,** 165432 (2002).

[45] Barnes, W., Preist, T., Kitson, S. & Sambles, J. Physical origin of photonic energy gaps in the propagation of surface plasmons on gratings. *Physical Review B* **54,** 6227–6244 (1996).

[46] Rochon, P. L. & Lévesque, L. Standing wave surface plasmon mediated forward and backward scattering. *Optics Express* **14,** 13050–5 (2006).

[47] Maier, S. S. A. & Atwater, H. A. Plasmonics: Localization and guiding of electromagnetic energy in metal/dielectric structures. *Journal of Applied Physics* **98,** 011101 (2005).

[48] Mie, G. Beiträge zur Optik trüber Medien, speziell kolloidaler Metallösungen. *Annalen der physik* **330,** 377–445 (1908).

[49] Kelly, K. L., Coronado, E., Zhao, L. L. & Schatz, G. C. The Optical Properties of Metal Nanoparticles: The Influence of Size, Shape, and Dielectric Environment. *The Journal of Physical Chemistry B* **107,** 668–677 (2003).

[50] Stuart, H. & Hall, D. Absorption enhancement in silicon-on-insulator waveguides using metal island films. *Applied Physics Letters* **69,** 2327–2329 (1996).

[51] Stuart, H. & Hall, D. Island size effects in nanoparticle-enhanced photodetectors. *Applied Physics Letters* **73,** 3815–3817 (1998).

[52] Lim, S. H., Mar, W., Matheu, P., Derkacs, D. & Yu, E. T. Photocurrent spectroscopy of optical absorption enhancement in silicon photodiodes via scattering from surface plasmon polaritons in gold nanoparticles. *Journal of Applied Physics* **101,** 104309 (2007).

[53] Temple, T. L., Mahanama, G. D. K., Reehal, H. S. & Bagnall, D. M. Influence of localized surface plasmon excitation in silver nanoparticles on the performance of silicon solar cells. *Solar Energy Materials and Solar Cells* **93,** 1978–1985 (2009).

[54] Pillai, S., Catchpole, K. R., Trupke, T. & Green, M. A. Surface plasmon enhanced silicon solar cells. *Journal of Applied Physics* **101,** 093105 (2007).

[55] Matheu, P., Lim, S. H., Derkacs, D., McPheeters, C. & Yu, E. T. Metal and dielectric nanoparticle scattering for improved optical absorption in photovoltaic devices. *Applied Physics Letters* **93,** 113108 (2008).

[56] Derkacs, D., Lim, S. H., Matheu, P., Mar, W. & Yu, E. T. Improved performance of amorphous silicon solar cells via scattering from surface plasmon polaritons in nearby metallic nanoparticles. *Applied Physics Letters* **89,** 239–241 (2006).

[57] Stenzel, O., Stendal, A., Voigtsberger, K. & von Borczyskowski, C. Enhancement of the photovoltaic conversion efficiency of copper phthalocyanine thin film devices by incorporation of metal clusters. *Solar Energy Materials and Solar Cells* **37,** 337–348 (1995).

[58] Westphalen, M., Kreibig, U., Rostalski, J., Lüth, H. & Meissner, D. Metal cluster enhanced organic solar cells. *Solar Energy Materials and Solar Cells* **61,** 97–105 (2000).

[59] Morfa, A. J., Rowlen, K. L., Reilly III, T. H., Romero, M. J. & van de Lagemaat, J. Plasmon-enhanced solar energy conversion in organic bulk heterojunction photovoltaics. *Applied Physics Letters* **92,** 013504 (2008).

[60] Kim, S.-S., Na, S.-I., Jo, J., Kim, D.-Y. & Nah, Y.-C. Plasmon enhanced performance of organic solar cells using electrodeposited Ag nanoparticles. *Applied Physics Letters* **93,** 073307 (2008).

[61] Chen, X. *et al.* Insight into the efficiency enhancement of polymer solar cells by incorporating gold nanoparticles. *Solar Energy Materials and Solar Cells* **111,** 1–8 (2013).

[62] Duche, D. *et al.* Improving light absorption in organic solar cells by plasmonic contribution. *Solar Energy Materials and Solar Cells* **93,** 1377–1382 (2009).

[63] Shen, H., Bienstman, P. & Maes, B. Plasmonic absorption enhancement in organic solar cells with thin active layers. *Journal of Applied Physics* **106,** 073109 (2009).

[64] Kochergin, V., Neely, L., Jao, C.-Y. & Robinson, H. D. Aluminum plasmonic nanostructures for improved absorption in organic photovoltaic devices. *Applied Physics Letters* **98,** 133305 (2011).

[65] Chou, S., Krauss, P. & Renstrom, P. Imprint of sub-25 nm vias and trenches in polymers. *Applied Physics Letters* **67,** 3114–3116 (1995).

[66] Roman, L. S. *et al.* Trapping Light in Polymer Photodiodes with Soft Embossed Gratings. *Advanced Materials* **12,** 189–195 (2000).

[67] Na, S.-I. *et al.* Surface relief gratings on poly(3-hexylthiophene) and fullerene blends for efficient organic solar cells. *Applied Physics Letters* **91,** 173509 (2007).

[68] Shih, C. F., Hung, K. T., Wu, J. W., Hsiao, C. Y. & Li, W. M. Efficiency improvement of blended poly(3-hexylthiophene) and 1-(3-methoxycarbonyl)-propyl-1-phenyl-(6,6)C61 solar cells by nanoimprinting. *Applied Physics Letters* **94,** 143505 (2009).

[69] You, J. *et al.* Surface Plasmon and Scattering-Enhanced Low-Bandgap Polymer Solar Cell by a Metal Grating Back Electrode. *Advanced Energy Materials* **2,** 1203–1207 (2012).

[70] Li, X. *et al.* Polarization-independent efficiency enhancement of organic solar cells by using 3-dimensional plasmonic electrode. *Applied Physics Letters* **102,** 153304 (2013).

[71] Tvingstedt, K., Persson, N.-K., Inganäs, O., Rahachou, A. & Zozoulenko, I. V. Surface plasmon increase absorption in polymer photovoltaic cells. *Applied Physics Letters* **91,** 113514 (2007).

[72] Ebbesen, T. W., Lezec, H. J., Ghaemi, H. F., Thio, T. & Wolff, P. A. Extraordinary optical transmission through sub-wavelength hole arrays. *Nature* **391,** 667–669 (1998).

[73] Lindquist, N. C., Luhman, W. A., Oh, S.-H. & Holmes, R. J. Plasmonic nanocavity arrays for enhanced efficiency in organic photovoltaic cells. *Applied Physics Letters* **93,** 123308 (2008).

[74] Luhman, W. A., Hoon Lee, S., Johnson, T. W., Holmes, R. J. & Oh, S. H. Self-assembled plasmonic electrodes for high-performance organic photovoltaic cells. *Applied Physics Letters* **99,** 103306 (2011).

[75] Min, C. *et al.* Enhancement of optical absorption in thin-film organic solar cells through the excitation of plasmonic modes in metallic gratings. *Applied Physics Letters* **96** (2010).

[76] Ahn, S. H. & Guo, L. J. High-Speed Roll-to-Roll Nanoimprint Lithography on Flexible Plastic Substrates. *Advanced Materials* **20,** 2044–2049 (2008).

[77] Rakic, A. D., Djurisic, A. B., Elazar, J. M. & Majewski, M. L. Optical properties of metallic films for vertical-cavity optoelectronic devices. *Applied Optics* **37,** 5271–5283 (1998).

[78] Pines, D. & Bohm, D. A collective description of electron interactions: II. Collective vs individual particle aspects of the interactions. *Physical Review* **85,** 338 (1952).

[79] Pines, D. Collective energy losses in solids. *Reviews of Modern Physics* **28** (1956).

[80] Brooker, G. *Modern Classical Optics* (OUP Oxford, 2003).

[81] Sernelius, B. E. in *Surface Modes in Physics* 99–165 (Wiley-VCH Verlag, Weinheim, 2005).

[82] Heavens, O. S. Optical properties of thin films. *Reports on Progress in Physics* **23,** 1 (1960).

[83] Peumans, P., Yakimov, A. & Forrest, S. R. Small molecular weight organic thin-film photodetectors and solar cells. *Journal of Applied Physics* **104,** 3693 (2003).

[84] Yee, K. Numerical solution of initial boundary value problems involving maxwell's equations in isotropic media. *IEEE Transactions on Antennas and Propagation* **14,** 302–307 (1966).

[85] Lumerical Solutions Inc. *FDTD Solutions [software]*

[86] Monestier, F. *et al.* Modeling the short-circuit current density of polymer solar cells based on P3HT:PCBM blend. *Solar Energy Materials and Solar Cells* **91,** 405–410 (2006).

[87] Tumbleston, J. R., Ko, D.-H., Lopez, R. & Samulski, E. T. *Characterizing enhanced performance of nanopatterned bulk heterojunction organic photovoltaics* in *Proc. SPIE* **7047** (2008), 70470S:1–70470S:9.

[88] Palik, E. D. *Handbook of Optical Constants of Solids Handbook of Optical Constants of Solids* **v.4** (Academic Press, 1998).

[89] Mittra, R. & Yu, W. A conformal FDTD software package modeling antennas and microstrip circuit components. *IEEE Antennas and Propagation Magazine* **42,** 28–39 (2000).

[90] Press, A. I. N. *et al.* Reporting solar cell efficiencies in Solar Energy Materials and Solar Cells. *Solar Energy Materials and Solar Cells* **92,** 371–373 (2008).

[91] Liu, B. *et al.* High internal quantum efficiency in fullerene solar cells based on crosslinked polymer donor networks. *Nature communications* **3,** 1321 (2012).

[92] Park, S. H. *et al.* Bulk heterojunction solar cells with internal quantum efficiency approaching 100%. *Nature photonics* **3,** 297–302 (2009).

[93] Moulé, A. J., Bonekamp, J. B. & Meerholz, K. The effect of active layer thickness and composition on the performance of bulk-heterojunction solar cells. *Journal of Applied Physics* **100,** 094503 (2006).

[94] Gordon, R. G. Criteria for Choosing Transparent Conductors. *MRS bulletin,* 52–57 (2000).

[95] Min Nam, Y., Huh, J. & Ho Jo, W. Optimization of thickness and morphology of active layer for high performance of bulk-heterojunction organic solar cells. *Solar Energy Materials and Solar Cells* **94,** 1118–1124 (2010).

[96] Moulé, A. & Meerholz, K. Minimizing optical losses in bulk heterojunction polymer solar cells. *Applied Physics B* **86,** 721–727 (2007).

[97] Beal, R. M. *et al.* The Molecular Structure of Polymer–Fullerene Composite Solar Cells and Its Influence on Device Performance. *Macromolecules* **43,** 2343–2348 (2010).

[98] Byrnes, S. *tmm [software] – https://pypi.python.org/pypi/tmm*

[99] Koev, S. T., Agrawal, A., Lezec, H. J. & Aksyuk, V. A. An Efficient Large-Area Grating Coupler for Surface Plasmon Polaritons. *Plasmonics* **7,** 269–277 (2011).

[100] Mitchell, E. W. J. & Mitchell, J. W. The work functions of copper, silver and aluminium. *Proceedings of the Royal Society of London. Series A. Mathematical and Physical Sciences* **210,** 70–84 (1951).

[101] Krasavin, A. V., MacDonald, K. F. & Zheludev, N. I. *Nanophotonics with Surface Plasmons* 109–139 (Elsevier, 2007).

[102] Koster, L., Smits, E., Mihailetchi, V. & Blom, P. Device model for the operation of polymer/fullerene bulk heterojunction solar cells. *Physical Review B* **72** (2005).

[103] Fallahpour, A. H., Ulisse, G., Auf der Maur, M., Di Carlo, A. & Brunetti, F. 3-D Simulation and Optimization of Organic Solar Cell With Periodic Back Contact Grating Electrode. *IEEE Journal of Photovoltaics* **5,** 591–596 (2015).

[104] Taflove, A., Johnson, S. G. & Oskooi, A. *Advances in FDTD Computational Electrodynamics: Photonics and Nanotechnology* 83–86 (Artech house, 2013).

[105] Blanc, P. *et al.* Direct normal irradiance related definitions and applications: The circumsolar issue. *Solar Energy* **110,** 561–577 (2014).

[106] Smith, C. J., Forster, P. M. & Crook, R. An all-sky radiative transfer method to predict optimal tilt and azimuth angle of a solar collector. *Solar Energy* **123,** 88–101 (2016).

[107] Mousazadeh, H. *et al.* A review of principle and sun-tracking methods for maximizing solar systems output. *Renewable & Sustainable Energy Reviews* **13,** 1800–1818 (2009).

[108] Holbert, K. E. & Srinivasan, D. *Handbook of renewable energy technology* (eds Zobaa, A. F. & Bansal, R. C.) 189–204 (World Scientific, 2011).

[109] Muneer, T., Etxebarria, S. & Gago, E. Monthly averaged-hourly solar diffuse radiation model for the UK. *Building Services Engineering Research and Technology* **35,** 573–584 (2014).

[110] Carlé, J. E. *et al.* A laboratory scale approach to polymer solar cells using one coating/printing machine, flexible substrates, no ITO, no vacuum and no spincoating. *Solar Energy Materials and Solar Cells* **108,** 126–128 (2013).

[111] Nickel, F. *et al.* Mechanically robust, ITO-free, 4.8% efficient, all-solution processed organic solar cells on flexible PET foil. *Solar Energy Materials and Solar Cells* **130,** 317–321 (2014).

[112] Elman, J. F., Greener, J., Herzinger, C. M. & Johs, B. Characterization of biaxially-stretched plastic films by generalized ellipsometry. *Thin Solid Films* **313–314,** 814–818 (1998).

[113] Singh, G. & Mehta, D. S. Residual and Induced Birefringence Measurement of. *Journal of Display Technology* **11,** 1035–1041 (2015).

[114] Monestier, F. *et al.* Modeling the short-circuit current density of polymer solar cells based on P3HT:PCBM blend. *Solar Energy Materials and Solar Cells* **91,** 405–410 (2007).

[115] Sergeant, N. P. *et al.* Design of Transparent Anodes for Resonant Cavity Enhanced Light Harvesting in Organic Solar Cells. *Advanced Materials* **24,** 728–732 (2012).

[116] Kundu, S. *et al.* Device stability of inverted and conventional bulk heterojunction solar cells with MoO3 and ZnO nanoparticles as charge transport layers. *Organic Electronics* **14,** 3083–3088 (2013).

[117] Vervisch, W. *et al.* Optical-electrical simulation of organic solar cells: Influence of light trapping by photonic crystal and ZnO spacer on electrical characteristics. *Journal of Applied Physics* **111,** 094506 (2012).

[118] Gilot, J., Barbu, I., Wienk, M. M. & Janssen, R. A. J. The use of ZnO as optical spacer in polymer solar cells: Theoretical and experimental study. *Applied Physics Letters* **91,** 113520:1–11352:3 (2007).

[119] Pacios, R. *et al.* Effects of photo-oxidation on the performance of poly[2-methoxy-5-(3',7'-dimethyloctyloxy)-1,4-phenylene vinylene]:[6,6]-phenyl C-61-butyric acid methyl ester solar cells. *Advanced Functional Materials* **16,** 2117–2126 (2006).

[120] Sigmund, P. Theory of Sputtering. I. Sputtering Yield of Amorphous and Polycrystalline Targets. *Physical Review* **184,** 383–416 (1969).

[121] Tseng, A. A. Recent developments in micromilling using focused ion beam technology. *Journal of Micromechanics and Microengineering* **14,** R15–R34 (2004).

[122] Assayag, G. B. New characterization method of ion current-density profile based on damage distribution of Ga+ focused-ion beam implantation in GaAs. *Journal of Vacuum Science & Technology B* **11,** 2420 (1993).

[123] Steckl, A. J. & Chyr, I. Focused ion beam micromilling of GaN and related substrate materials (sapphire, SiC, and Si). *American Vacuum Society* **17,** 362–365 (1999).

[124] Santamore, D., Edinger, J., Orloff, J. & Melngailis, J. Focused ion beam sputter yield change as a function of scan speed. *Journal of Vacuum Science & Technology B: Microelectronics and Nanometer Structures* **15,** 2346 (1997).

[125] Wong, I. & Ho, C. Surface molecular property modifications for poly (dimethylsiloxane)(PDMS) based microfluidic devices. *Microfluidics and nanofluidics* **7,** 291–306 (2009).

[126] Vieu, C. *et al.* Electron beam lithography: resolution limits and applications. *Applied Surface Science* **164,** 111–117 (2000).

[127] Broers, A., Hoole, A. & Ryan, J. Electron beam lithography — Resolution limits. *Microelectronic Engineering* **32,** 131–142 (1996).

[128] Joshi-Imre, A. & Bauerdick, S. Direct-Write Ion Beam Lithography. *Journal of Nanotechnology* **2014** (2014).